INTERNATIONAL ATOMIC ENERGY AGENCY
UNITED NATIONS EDUCATIONAL, SCIENTIFIC AND CULTURAL ORGANIZATION
INTERNATIONAL CENTRE FOR THEORETICAL PHYSICS
I.C.T.P., P.O. BOX 586, 34100 TRIESTE, ITALY, CABLE: CENTRATOM TRIESTE

H4.SMR/650-12

Workshop on Three-Dimensional Modelling
of Seismic Waves Generation
Propagation and their Inversion

30 November - 11 December 1992

Seismic Ray Method for 3-D Structures:
Possibilities and Limitations

V. Cerveny

Charles University
Dept. of Geophysics
Faculty of mathematics and Physics
Prague
Czech and Slovak

SEISMIC RAY METHOD FOR 3-D STRUCTURES: POSSIBILITIES AND LIMITATIONS

The lectures consist of four parts:

1) In the first part, the basic principles of the seismic ray method are explained.

2) In the second part, the validity conditions and limitations of the seismic ray method are discussed. The Fresnel volumes are introduced. Various singular regions of the ray fields and anomalous situations of the seismic ray method are described.

3) In the third part, the methods of direct evaluation of first arrival travel times (without computation of rays) are explained.

4) In the fourth part, various extensions of the ray method which can be used even in situations where the ray method fails are briefly reviewed.

The lecture notes cover only selected parts of the lectures. For a more detailed explanation, see the included references.

PART 1

BASIC PRINCIPLES OF THE SEISMIC RAY METHOD

In this part of lectures, the procedures to evaluate travel times and ray amplitudes of seismic body waves are briefly reviewed. Ray tracing and dynamic ray tracing procedures are discussed. Expressions for the ray-theory elastodynamic Green functions are derived.

A general inhomogeneous anisotropic medium is considered. The explanation does not consider structural interfaces, but the resulting equations may be simply modified even for a more general case of layered and blocked structures.

References:

V. Červený, I. A. Molotkov, I. Pšenčík: Ray Method in Seismology. Charles University Press, Prague 1977

V. Červený: Seismic Ray Theory. In Encyclopedia of Geophysics, D. E. James, ed., Van Nostrand Co., 1989.

V. Červený: Seismic Ray Theory. Cambridge University Press, under preparation.

The complete treatment of the problem will be given in the last reference. The dynamic ray tracing in isotropic inhomogeneous media is explained in Červený (1989), and also in Červený and Soares (1992), included in Part 2.

HIGH-FREQUENCY ASYMPTOTIC SOLUTIONS OF ELASTODYNAMIC EQUATION IN INHOMOGENEOUS ANISOTROPIC MEDIA

ELASTODYNAMIC EQUATION:

$$\frac{\partial}{\partial x_j}\left(c_{ijkl}\frac{\partial u_k}{\partial x_l}\right)+f_i=\rho\frac{\partial^2 u_i}{\partial t^2}, \qquad i=1,2,3.$$

x_i ... Cartesian coordinates,
t ... time,
ρ ... density,
c_{ijkl} ... elastic parameters, $c_{ijkl}=c_{ijkl}(x_i)$
u_i ... Cartesian components of the displacement vector $\vec{u}$
f_i ... Cartesian components of a body force, $f_i=f_i(x_m)$.

BODY WAVE HF SOLUTION

$$u_i(x_m,t)=U_i(x_m)\,F(t-T(x_m)),$$

U_i ... Cartesian components of a complex-valued amplitude vector $\vec{U}$,
T ... travel time field, $T=T(x_m)$,
$F(\phi)$ ... analytical signal, $F(\phi)=x(\phi)\pm i g(\phi)$, $x(\phi)$ and $g(\phi)$ form a Hilbert transform pair

ASSUMPTIONS

$$|\dot{F}(\vartheta)| \gg \left|\frac{\partial c_{ijkl}}{\partial x_m}\right|, \left|\frac{\partial \varrho}{\partial x_m}\right|, \quad \left|\frac{\partial U_k}{\partial x_m}\right|, \left|\frac{\partial p_i}{\partial x_m}\right|.$$

[High-frequency body waves are considered].

NOTATIONS

$a_{ijkl} = \frac{c_{ijkl}}{\varrho}$ — density normalised elastic parameters

$\Gamma_{ik} = a_{ijkl}\, p_j p_l$ — Christoffel matrix (3×3),

$p_i = \partial T / \partial x_i$ — components of the slowness vector $\vec{p} = \nabla T$,

$G_m(x_n, p_n)$, $m=1,2,3$ — Eigenvalues of the Christoffel matrix

$\vec{g}^{(m)}(x_n, p_n)$, $m=1,2,3$ — Relevant eigenvectors

Isotropic medium:

$G_1 = G_2 = \beta^2 p_i p_i$ $\quad \beta = \sqrt{\frac{\mu}{\varrho}}$

$G_3 = \alpha^2 p_i p_i$ $\quad \alpha = \sqrt{\frac{\lambda+2\mu}{\varrho}}$

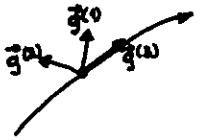

SOLUTIONS

Three HF seismic body waves propagate in the anisotropic inhomogeneous medium ($m=1,2,3$). Each of them is described by the equation

$$u_i(x_n, t) = U_i(x_n)\, F(t - T(x_n))$$

Isotopic: 2 waves - P and S

(1) The eikonal equation (equation for $T(x_n)$):

$$G_m(x_n, p_n) = 1.$$

Isotopic m.:

$\beta^2 p_i p_i = 1$ — S wave

or

$\alpha^2 p_i p_i = 1$ — P wave

(2) Polarisation equation for $\vec{U}$,

$$\vec{U}(x_n) = U(x_n)\, \vec{g}^{(m)}.$$

(3) Transport equation for $U(x_n)$,

$$\nabla U \cdot \vec{V}^G + \frac{U}{2\varrho} \nabla \cdot (\varrho \vec{V}^G) = 0.$$

$\vec{V}^G$ ... group velocity vector

(4) The analytical signal $F(\vartheta)$ may be arbitrary, but must be high-frequency.

$G_m(x_n, p_n)$ ... eigenvalues of the christoffel matrix Γ_{ik}

$\vec{g}^{(m)}(x_n, p_n)$ ... relevant eigenvectors

$\Gamma_{ik} = \frac{c_{ijkl}}{\varrho}\, p_j p_l$

SOLUTIONS OF THE EIKONAL EQUATION $G_m(x_n, p_n) = 1$ FOR THE TRAVEL TIME $T(x_n)$.

1) DIRECT SOLUTION FOR $T(x_n)$
2) SOLUTION USING RAYS

(a) EXACT TRAVEL TIME COMPUTATIONS

Ray tracing systems:

$$\frac{dx_i}{dT} = \frac{1}{2}\frac{\partial G_m}{\partial p_i}, \qquad \frac{dp_i}{dT} = -\frac{1}{2}\frac{\partial G_m}{\partial x_i}.$$

This yields $(i=1,2,3)$.

$$\frac{dx_i}{dT} = a_{ijke}\, p_e\, g_k^{(m)} g_j^{(m)}, \qquad \frac{dp_i}{dT} = -\frac{1}{2}\frac{\partial a_{ijke}}{\partial x_i}\, p_e p_s\, g_k^{(m)} g_l^{(m)},$$
$(i=1,2,3)$

(b) APPROXIMATE TRAVEL TIME COMPUTATIONS

Perturbation methods

δa_{ijkl} ... perturbations in elastic parameters
δT ... perturbations in the travel time

$$\delta T(0,S) = -\frac{1}{2}\int_{0\,(L)}^{S} \delta a_{ijke}\, p_i p_e\, g_k^{(m)} g_l^{(m)}\, dT$$

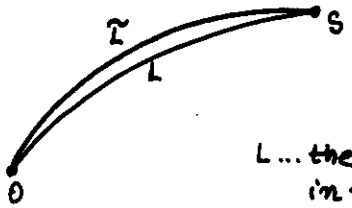

L ... the ray from 0 to S in the unperturbed medium
T ... the ray from 0 to S in the perturbed medium

COMPUTATION OF AMPLITUDES ALONG RAYS

$$\vec{U}(x_n) = U(x_n)\,\vec{q}^{(m)}$$

$\vec{q}^{(m)}$ ... polarization vector (eigenvector of the Christoffel matrix)

$U(x_n)$ satisfies the transport equation

Solution of the transport equation along the ray

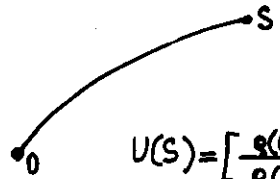

$$U(S) = \left[\frac{\rho(0)\, c(0)\, J(0)}{\rho(S)\, c(S)\, J(S)}\right]^{1/2} U(0),$$

Here J is the ray Jacobian, c the group velocity.

$$J = \frac{D(x_1, x_2, x_3)}{D(\gamma_1, \gamma_2, \gamma_3)},$$

where $\gamma_1, \gamma_2, \gamma_3$ are ray coordinates.
J is proportional to the cross-sectional area of the ray tube.

Computation of the ray Jacobian J:

(a) Finite-differences, from four rays,
(b) Dynamic ray tracing, along 1 ray. (paraxial methods)

DYNAMIC RAY TRACING (DRT)

Computation of the travel time field in the paraxial vicinity of the ray

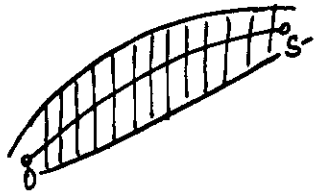

$$\frac{d}{dt}\left(\frac{\partial x_i}{\partial \gamma_J}\right) = \frac{1}{2}\frac{\partial^2 G_m}{\partial p_i \partial x_j}\frac{\partial x_j}{\partial \gamma_J} + \frac{1}{2}\frac{\partial^2 G_m}{\partial p_i \partial p_j}\frac{\partial p_j}{\partial \gamma_J},$$

$$\frac{d}{dt}\left(\frac{\partial p_i}{\partial \gamma_J}\right) = -\frac{1}{2}\frac{\partial^2 G_m}{\partial x_i \partial x_j}\frac{\partial x_j}{\partial \gamma_J} - \frac{1}{2}\frac{\partial^2 G_m}{\partial x_i \partial p_j}\frac{\partial p_j}{\partial \gamma_J},$$

$i = 1,2,3$, $J = 1,2$ ⇒ 12 equations

γ_1, γ_2 ... ray parameters. (Červený, 1972)

Solution:

$$\begin{pmatrix} \frac{\partial x_1}{\partial \gamma_1} & \frac{\partial x_2}{\partial \gamma_1} & \frac{\partial x_3}{\partial \gamma_1} \\ \frac{\partial x_1}{\partial \gamma_2} & \frac{\partial x_2}{\partial \gamma_2} & \frac{\partial x_3}{\partial \gamma_2} \end{pmatrix} \qquad \begin{pmatrix} \frac{\partial p_1}{\partial \gamma_1} & \frac{\partial p_2}{\partial \gamma_1} & \frac{\partial p_3}{\partial \gamma_1} \\ \frac{\partial p_1}{\partial \gamma_2} & \frac{\partial p_2}{\partial \gamma_2} & \frac{\partial p_3}{\partial \gamma_2} \end{pmatrix}.$$

From these matrices, the ray jacobian J can be computed.

The matrices, however, have many other applications, similarly as in isotropic media.

RAY PROPAGATOR MATRIX $\Pi(0,S)$

(Matrix of linearly independent solutions of the DRT system).

The solutions of the DRT system given above, however, are not linearly independent.

Necessary to evaluate some auxiliary matrices and multiply the whole system by these matrices.

Final form of the DRT:

$$\frac{dX}{dT} = SX \qquad \text{4 equations}$$

X ... 4×1 matrix

S ... 4×4 matrix

$\Pi(S,0)$ ... 4×4 ray propagator matrix from the point 0 to the point S

$$\Pi(0,0) = \begin{pmatrix} I & 0 \\ 0 & I \end{pmatrix}$$

I ... 2×2 identity matrix

0 ... 2×2 null matrix

↓ point source at 0

local plane wave at 0

Notation:

$$\Pi(S,0) = \begin{pmatrix} Q_1(S,0) & Q_2(S,0) \\ P_1(S,0) & P_2(S,0) \end{pmatrix}$$

does not depend on the parameterization of the field

↓ point source solution

plane wave solution

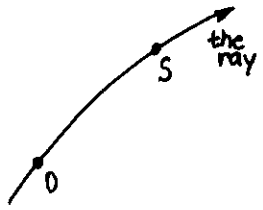

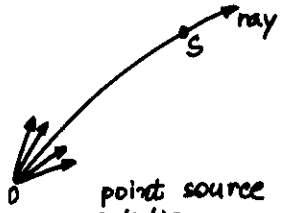

point source solution

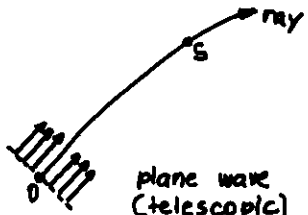

plane wave (telescopic) solution

INVERSE OF THE RAY PROPAGATOR MATRIX

$$\Pi(S,0) = \begin{pmatrix} Q_1(S,0) & Q_2(S,0) \\ P_1(S,0) & P_2(S,0) \end{pmatrix}$$

$$\Pi(0,S) = \begin{pmatrix} Q_1(0,S) & Q_2(0,S) \\ P_1(0,S) & P_2(0,S) \end{pmatrix}$$

It can be proved that

$$\boxed{\Pi(0,S) = \Pi^{-1}(S,0) = \begin{pmatrix} P_2^T(S,0) & -Q_2^T(S,0) \\ -P_1^T(S,0) & Q_1^T(S,0) \end{pmatrix}}$$

This yields, among others,

$$Q_2(0,S) = -Q_2^T(S,0)$$

$$\boxed{\det Q_2(0,S) = \det Q_2(S,0)}$$

Important equations.
Basic importance in the proofs of reciprocity.

DISPLACEMENT VECTOR FOR A POINT SOURCE

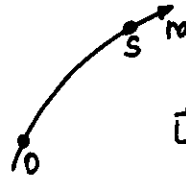

$$\vec{U}(S)\vec{g}(S) = \left[\frac{\rho(0)c(0)J(0)}{\rho(S)c(S)J(S)}\right]^{1/2} \vec{U}(0)\vec{g}(0)$$

$$\vec{U}(S) = \left[\frac{\rho(0)c(0)J(0)}{\rho(S)c(S)J(S)}\right]^{1/2} (\vec{U}(0)\vec{g}(0))\cdot\vec{g}(S)$$

$$= \left[\frac{\rho(0)c(0)|J(0)|}{\rho(S)c(S)|J(S)|}\right]^{1/2} e^{i\delta T(0,S)} (\vec{U}(0)\vec{g}(0))\cdot\vec{g}(S)$$

c ... group velocity
$\vec{g}$ ... polarization vector
$\delta T(0,S)$ ... phase shift due to caustics between 0 and S

Point source at 0:

$$\vec{U}(0)\cdot\vec{g}(0) \to \infty, \quad |J(0)| \to 0,$$

$|J(0)|^{1/2}(\vec{U}(0)\cdot\vec{g}(0))$ remains finite, non-vanishing.

$$\vec{U}(S) = \left[\frac{\rho(0)c(0)}{\rho(S)c(S)}\right]^{1/2} \frac{1}{|J(S)|^{1/2}} e^{i\delta T(0,S)} \Psi(0)\,\vec{g}(S),$$

where

$$\Psi(0) = \lim_{\substack{0_s \to 0 \\ \text{along } \Omega}} \left\{ |J(0_s)|^{1/2} (\vec{U}(0_s)\cdot\vec{g}(0_s)) \right\}.$$

DETERMINATION OF THE RAY JACOBIAN J

$$J(S) = \frac{C(S)}{c(S)} \det Q(S)$$

$C(S)$ ... phase velocity
$c(S)$ ... group velocity
$Q(S)$ ... 2x2 matrix determined by DRT

Application of the ray propagator matrix:

$$\begin{pmatrix} Q(S) \\ P(S) \end{pmatrix} = \Pi(S,0) \begin{pmatrix} Q(0) \\ P(0) \end{pmatrix}$$

$$= \begin{pmatrix} Q_1(S,0) & Q_2(S,0) \\ P_1(S,0) & P_2(S,0) \end{pmatrix} \begin{pmatrix} Q(0) \\ P(0) \end{pmatrix}$$

Point source at 0 : $Q(0) = 0$. Then

$$Q(S) = Q_2(S,0)\, P(0),$$

$$\boxed{J(S) = \frac{C(S)}{c(S)} \det Q_2(S,0) \det P(0).}$$

Displacement vector:

$$\vec{U}(S) = \left[\frac{\rho(0)\, C(0)}{\rho(S)\, C(S)}\right]^{1/2} \frac{\exp(i\delta T(0,S))}{|\det Q_2(S,0)|^{1/2}}\, \tilde{\Psi}(0)\, \vec{q}(S)$$

$$\tilde{\Psi}(0) = \lim_{\substack{O_S \to 0 \\ \text{along } \Omega}} \left\{ |\det Q_2(O_S,0)|^{1/2} (\vec{U}(O_S) \cdot \vec{q}(O_S)) \right\}.$$

DETERMINATION OF $\tilde{\Psi}(0)$ FOR A SINGLE UNIT FORCE AT 0.

$\vec{f}_m$ ... a single unit force in the direction of the Cartesian axis x_m
$\vec{f}_m = \vec{e}_m$

The expression for $\tilde{\Psi}(0)$ can be found for a locally homogeneous anisotropic medium in the vicinity of 0,

$$\boxed{\tilde{\Psi}(0) = \frac{1}{4\pi \rho(0) (C(0))^{3/2}} (\vec{e}_m(0)\, \vec{q}(0))_1}$$

$C(0)$ ... phase velocity at 0.

This yields,

$$\vec{U}(S) = \frac{1}{4\pi} \frac{\exp(i\delta T(0,S))}{[\rho(0)\rho(S)C(0)C(S)]^{1/2}} \frac{(\vec{e}_m(0)\cdot\vec{q}(0))}{|\det Q_2(S,0)|^{1/2}}\, \vec{q}(S)$$

$U_m(S)$ ... m-th Cartesian component of $\vec{U}$

$$\boxed{\begin{aligned} U_m(S) &= (\vec{U}(S)\cdot\vec{e}_m(S)) \\ &= \frac{1}{4\pi} \frac{\exp(i\delta T(0,S))}{[\rho(0)\rho(S)C(0)C(S)]^{1/2}} \frac{(\vec{e}_m(0)\vec{q}(0))(\vec{e}_m(S)\vec{q}(S))}{|\det Q_2(S,0)|^{1/2}}. \end{aligned}}$$

ELASTODYNAMIC RAY THEORY GREEN FUNCTION FOR ANISOTROPIC INHOMOGENEOUS MEDIA

Definition of the Green function $G_{mn}(S,t;0,t_0)$

$G_{mn}(S,t;0,t_0)$ is the m-th Cartesian component of the displacement vector at S at time t, caused by the application of a single force unit impulse in the direction of the m-th Cartesian axis at 0 and time t_0.

$$U_m(S)=\frac{1}{4\pi}\frac{\exp(i\delta T(0,S))}{[\varrho(0)\varrho(S)C(0)C(S)]^{1/2}}\frac{(\vec{e}_m(0)\vec{g}(0))(\vec{e}_m(S)\vec{g}(S))}{|\det Q_2(0,S)|^{1/2}}$$

We use the analytical signal

$$F(t-T(0,S))=\delta^{(A)}(t-t_0-T(0,S))$$

$\delta^{(A)}(\vartheta)$ ... analytical delta function

ELASTODYNAMIC RAY THEORY GREEN FUNCTION FOR ANISOTROPIC INHOMOGENEOUS MEDIA

FINAL EXPRESSIONS

$$G_{mn}(S,t;0,t_0)=\frac{\mathrm{Re}\{\exp(i\delta T(0,S))\,\delta^{(A)}(t-t_0-T(0,S))\}}{4\pi[\varrho(0)\varrho(S)C(0)C(S)\,|\det Q_2(S,0)|^{1/2}]}\times(\vec{e}_m(0)\vec{g}(0))(\vec{e}_m(S)\vec{g}(S))$$

The expression is fully reciprocal in the following sense:

$$G_{mn}(S,t;0,t_0)=G_{nm}(0,t;S,t_0).$$

Elastodynamic equation for $G_{in}(\vec{x},t;\vec{x}_0,t_0)$

$$\frac{\partial}{\partial x_j}\left(c_{ijkl}\frac{\partial G_{kn}}{\partial x_l}\right)-\varrho\frac{\partial^2 G_{in}}{\partial t^2}=-\delta_{in}\,\delta(\vec{x}-\vec{x}_0)\,\delta(t-t_0)$$

c_{ijkl} ... elastic moduli
δ_{in} ... Kronecker symbol

PART 2

VALIDITY CONDITIONS OF THE RAY METHOD. FRESNEL VOLUMES. SINGULAR REGIONS AND ANOMALOUS SITUATIONS

For the introduction of Fresnel volumes and their detailed discussion see paper Červený and Soares (1992). The paper also discusses the validity conditions of the ray method, see pages 913 - 914.

A discussion of singular regions and various anomalous situations in the seismic ray theory can be found in the references shown in Part 1.

GEOPHYSICS, VOL. 57, NO. 7 (JULY 1992): P. 902–915, 11 FIGS.

Fresnel volume ray tracing

Vlastislav Červený* and José Eduardo P. Soares‡

ABSTRACT

The concept of "Fresnel volume ray tracing" consists of standard ray tracing, supplemented by a computation of parameters defining the first Fresnel zones at each point of the ray. The Fresnel volume represents a 3-D spatial equivalent of the Fresnel zone that can also be called a physical ray. The shape of the Fresnel volume depends on the position of the source and the receiver, the structure between them, and the type of body wave under consideration. In addition, the shape also depends on frequency: it is narrow for a high frequency and thick for a low frequency. An efficient algorithm for Fresnel volume ray tracing, based on the paraxial ray method, is proposed. The evaluation of the parameters defining the first Fresnel zone merely consists of a simple algebraic manipulation of the elements of the ray propagator matrix. The proposed algorithm may be applied to any high-frequency seismic body wave propagating in a laterally varying 2-D or 3-D layered structure (P, S, converted, multiply reflected, etc.). Numerical examples of Fresnel volume ray tracing in 2-D inhomogeneous layered structures are presented. Certain interesting properties of Fresnel volumes are discussed (e.g., the double caustic effect). Fresnel volume ray tracing offers numerous applications in seismology and seismic prospecting. Among others, it can be used to study the resolution of the seismic method and the validity conditions of the ray method.

INTRODUCTION

In seismology, similarly as in other branches of physics, the rays can be introduced in several different ways. Commonly, they are defined as extremals of Fermat's functional, or as characteristics of the eikonal equation. They can also be interpreted as trajectories along which the high-frequency part of elastic energy propagates. All these alternative definitions yield the same ray trajectory. The actual ray trajectory, however, is only a mathematical fiction. For finite frequencies, the properties of the wave propagating along the ray under consideration and recorded at the receiver are influenced not only by the structure along the ray, but also by the structure in some vicinity of the ray.

The region in the vicinity of the ray that actually influences the properties of the wave propagating along the ray under consideration and recorded at the receiver has been a subject of interest and of numerous theoretical and experimental investigations for a long time. The results of such investigations are usually expressed in terms of well-known first Fresnel zones and their 3-D spatial equivalents, Fresnel volumes (see Figure 1). The Fresnel volume depends, of course, on the position of the source and receiver. However, it also depends on the frequency f. For higher frequencies, the Fresnel volumes are narrower. As we will show, the width of the Fresnel volume is inversely proportional to the square root of the frequency $\sqrt{f}$.

The term Fresnel volume is due to Kravtsov and Orlov (1979, 1980). Fresnel volumes are also known as *3-D Fresnel zones* (see Bertoni et al., 1971). Alternatively, they are also called *regions responsible for diffraction*, and similarly. It would also be sensible to call them *physical rays*, to emphasize their difference from *mathematical rays*. Whereas mathematical rays are merely volumeless trajectories, the physical rays are volumes of nonzero width concentrated close to the relevant mathematical rays. Their width is frequency dependent.

In a homogeneous medium, the ray connecting the source A with the receiver B is a straight line. The relevant Fresnel volume can then be calculated analytically, and it is represented by an ellipsoid with its foci at A and B (see the simple examples in Figure 2). Similarly, the Fresnel volume corresponding to a wave reflected from a planar interface between two homogeneous half-spaces can also be evaluated analyt-

Manuscript received by the Editor March 27, 1991; revised manuscript received January 3, 1992.
*Institute of Geophysics, Charles University, Ke Karlovu 3, 121 16 Praha 2, Czechoslovakia.
‡Rua do Matao 1226, Instituto Astronômico e Geofisico, Universidade de São Paulo, Cidade Universitaria-São Paulo-S.P., CEP. 05508, Brazil.

ically and has an ellipsoidal shape. In general, in laterally varying layered structures, the shape of the Fresnel volume is more complicated and must be evaluated numerically.

The exact computation of Fresnel volumes in complex 2-D and 3-D structures would require an extensive two-point ray tracing and would be extremely time consuming. In this paper, we propose a considerably more efficient approach for the calculation of the Fresnel volumes in complex structures. It is based on the application of the paraxial ray theory, particularly on the application of the ray propagator matrices. As the paraxial ray method is only approximate, the Fresnel volume evaluated by it will also only approximate the Fresnel volume computed exactly. To distinguish between the Fresnel volume calculated exactly and the Fresnel volume calculated by the paraxial ray method, we shall also call the former the exact Fresnel volume and the latter the *paraxial Fresnel volume*. The paraxial Fresnel volumes, however, represent the exact Fresnel volumes usually with high accuracy, particularly for higher frequencies. See a comparison of both computations in Figure 2.

At present, standard ray-tracing routines are usually supplemented by the dynamic ray tracing and by the computation of the ray propagator matrix. The dynamic ray tracing is, in general, required to determine the geometrical spreading and ray amplitudes. If the results of such computations are available along the ray, the paraxial Fresnel volume can be calculated at any point of the ray, simply by algebraic manipulation with the elements of the ray propagator matrix. There will be practically no additional expense to compute the Fresnel volume.

We shall introduce the following terminology and call the computation of a ray Ω from A to B, supplemented by the evaluation of the relevant Fresnel volume along the whole ray Ω from A to B, the *Fresnel volume ray tracing*. Alternatively, it would also be possible to use an abbreviated term, *the Fresnel ray tracing*, or to speak about *physical ray tracing*.

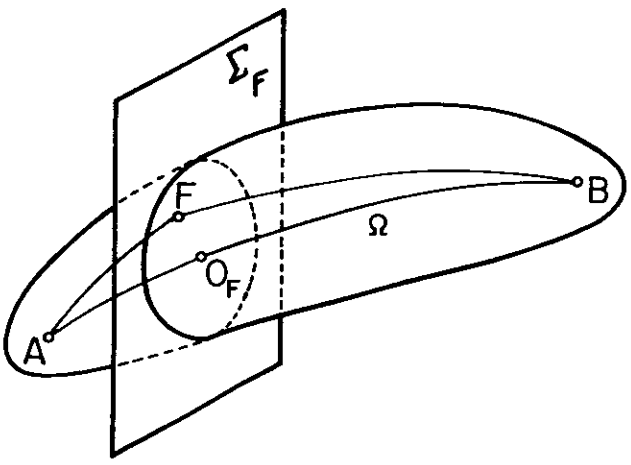

FIG. 1. Schematic presentation of a Fresnel volume for a point source at A and receiver at B. The point F belongs to the Fresnel volume if and only if it satisfies equation (1). The cross-section of the Fresnel volume by a plane Σ_F perpendicular to the ray at a point O_F represents the first Fresnel zone at O_F. Assume that the point F is situated in the plane Σ_F. Then it also belongs to the first Fresnel zone at O_F if it satisfies equation (1).

The Fresnel volumes and Fresnel zones play an important role in the solution of many wave propagation problems. In seismic prospecting, they have been used to study the horizontal resolution of seismic reflections (see Hagedoorn, 1959; Hilterman, 1970; Sheriff, 1977, 1980, 1985, 1989; Sheriff and Geldart, 1982; Kleyn, 1983; Lindsey, 1989; Eaton et al., 1991; and other references given in these papers and books. Also see, Pant and Greenhalgh (1989) for the laboratory investigation of the horizontal resolution of the seismic reflection method. Fresnel volumes and zones have also been used in the classification of scattering problems (see Flatté et al., 1979; Aki and Richards, 1980; and Wu and Aki, 1988). Fresnel volumes play an important role in the formulation of validity conditions of the ray method (see Kravtsov and Orlov, 1979, 1980 and Klem-Musatov, 1980). These applications will be discussed in greater detail in the last section. Even in singular regions, where the standard ray method fails (caustic regions, etc.), the Fresnel volumes can be used to find some robust quantitative estimates of the wavefield (See also Kravtsov and Orlov, 1980).

We believe that Fresnel volume ray tracing will find even some other, perhaps more important, applications in the numerical modeling of seismic wavefields and in the inversion of seismic data in the near future.

FRESNEL VOLUMES

We consider an elementary elastic harmonic wave propagating from a point source situated at A to the receiver situated at B. We denote the frequency of the wave by f and the relevant period by T. Further, we denote the ray connecting A and B by Ω and the traveltime from A to B by $\tau(B, A)$ (See Figure 1).

We introduce an auxiliary point F in the vicinity of the ray Ω and construct the rays connecting F with A and B. Along each of these rays, we compute the traveltimes $\tau(F, A)$ and $\tau(F, B)$.

We are now ready to give a definition of the Fresnel volume corresponding to the point source at A and receiver at B. Supported by numerous experiments and observations and by various theoretical and numerical investigations (e.g., by the method of the stationary phase), the Fresnel volume can be defined by the following equation (see Kravtsov and Orlov, 1980),

$$|\tau(F, A) + \tau(F, B) - \tau(B, A)| \leq \tfrac{1}{2}T. \qquad (1)$$

The point F belongs to the Fresnel volume corresponding to the source at A and receiver at B if and only if it satisfies equation (1). Note that the definition of Fresnel volumes in Kravtsov and Orlov (1980) is formally written in a slightly different form than in equation (1), as they use phases, where we use traveltimes.

As is obvious from the definition, the Fresnel volume is reciprocal, i.e., if we exchange the source and receiver, the Fresnel volume remains the same.

The boundary of the Fresnel volume is described by the relation

$$|\tau(F, A) + \tau(F, B) - \tau(B, A)| = \tfrac{1}{2}T. \qquad (2)$$

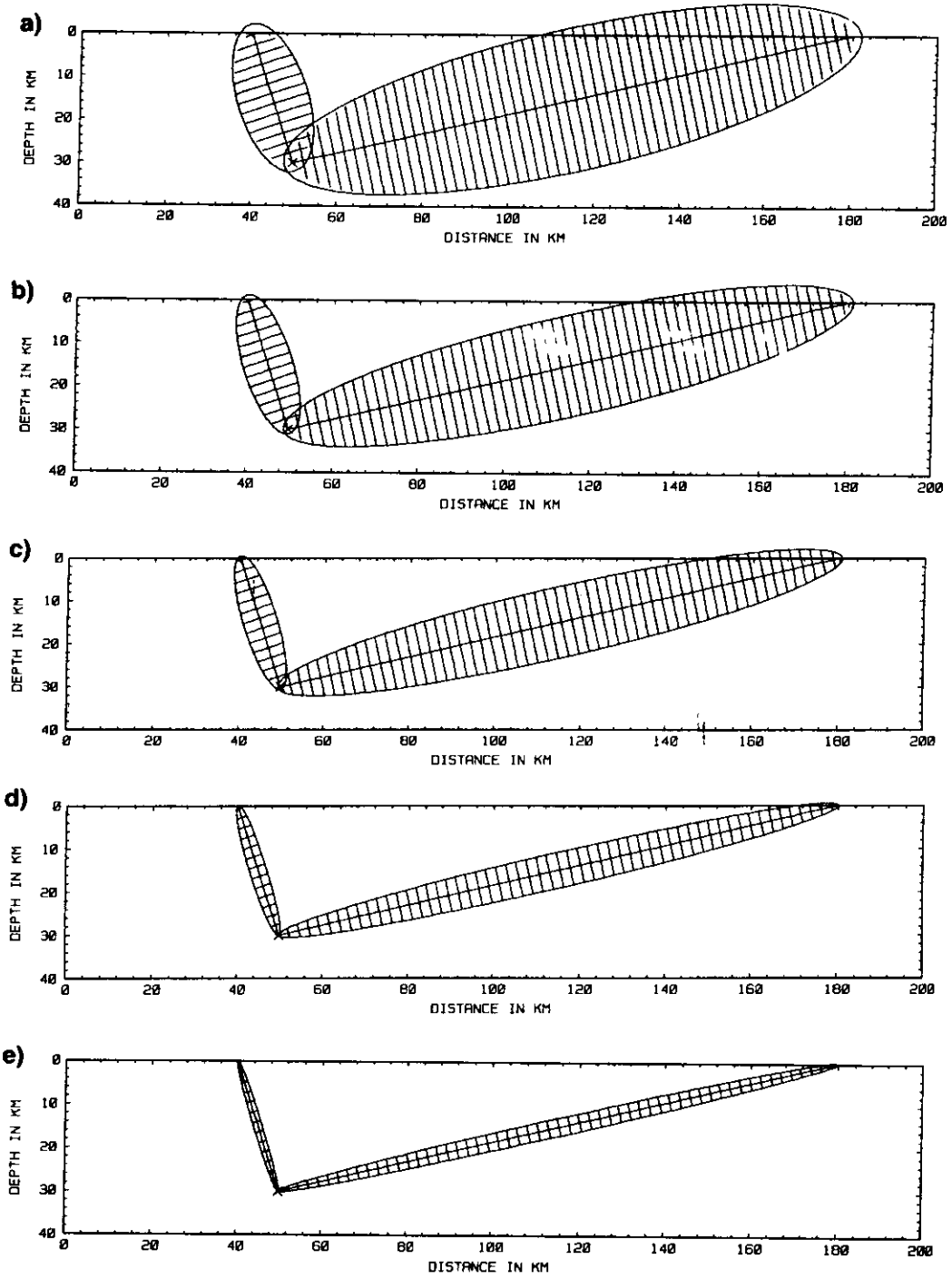

FIG. 2. Comparison of exact and paraxial Fresnel volumes in a homogeneous medium, with velocity $v = 6$ km/s. The point source is situated at depth, with two receivers at the earth's surface. The boundaries of the exact Fresnel volumes are shown by continuous lines, and the paraxial Fresnel volumes are represented discretely, by the radii of paraxial Fresnel zones. Five frequencies are considered: (a) $f = 0.75$ Hz, (b) $f = 1.5$ Hz, (c) $f = 3$ Hz, (d) $f = 12$ Hz, and (e) $f = 48$ Hz. The differences between the exact and paraxial Fresnel volumes are observable only for low frequencies close to the source and receivers.

We shall call the cross-section of the Fresnel volume equation (1) by a plane perpendicular to the ray Ω the Fresnel zone.

The Fresnel volume as defined by equation (1) as well as the Fresnel zone corresponds to the point source and receiver situated at points A and B. For different types of sources, alternative definitions can be written. For example, a Fresnel volume corresponding to the wavefield generated at an *initial surface* Σ and recorded at a point B can also be introduced. Such a configuration will play an important role in the study of the wavefield generated by finite faulting earthquake sources in seismology. In this paper, however, we shall consider only the *point source—point receiver configuration*.

Let us now discuss Equation (2) for the boundary of the Fresnel volume in a homogeneous medium. If we denote the velocity by v (= const.), we can rewrite equation (2) as follows:

$$\ell(F, A) + \ell(F, B) - \ell(B, A) = \frac{\lambda}{2}. \tag{3}$$

Here $\lambda = vT$ is the wavelength, $\ell(A, B)$ denotes the distance between points A and B; $\ell(F, A)$ and $\ell(F, B)$ have a similar meaning. It is not necessary to write the absolute value in equation (3), as the expression on the left-hand side is always positive in homogeneous media.

We now demonstrate the differences between exact Fresnel volumes and paraxial Fresnel volumes. The Cartesian coordinates x, y, z are considered, with points A and B situated along the x-axis. The coordinates of A, B, F are denoted as follows: $A \equiv [x_A, 0, 0]$, $B \equiv [x_B, 0, 0]$, $F \equiv [x_F, y_F, z_F]$, with $x_B > x_A$. Then equation (3) yields,

$$[(x_F - x_A)^2 + y_F^2 + z_F^2]^{1/2} + [(x_F - x_B)^2 + y_F^2 + z_F^2]^{1/2} = \frac{\lambda}{2} + \ell, \tag{4}$$

where $\ell = \ell(A, B) = x_B - x_A$. This is the equation for the boundary of the exact Fresnel volume. It represents a rotational ellipsoid with foci at points A, B. The Fresnel zones are circles. The algebraic treatment of equation (4) is left to the reader.

For small $y_F^2 + z_F^2$, equation (4) can also be treated approximately. For $x_B > x_F > x_A$, we obtain from equation (4),

$$r \doteq \left[\lambda \frac{(x_F - x_A)(x_B - x_F)}{x_B - x_A}\right]^{1/2}, \tag{5}$$

where $r = (y_F^2 + z_F^2)^{1/2}$ is the radius of the Fresnel zone. Equation (5) corresponds, in fact, to the paraxial ray approximation of equation (4) in a homogeneous medium.

Figure 2 demonstrates the differences between exact and paraxial Fresnel volumes. The boundaries of the exact Fresnel volumes calculated by equation (4) are shown by continuous lines, and the paraxial Fresnel volumes calculated using equation (5) are represented discretely, by the radii of paraxial Fresnel zones.

It is obvious from Figure 2 that the paraxial Fresnel volumes are good, sufficiently accurate approximations for the exact Fresnel volumes. Only close to points A and B, particularly for low frequencies, the accuracy is lower. Let us discuss the differences in the vicinity of A and B in greater detail.

The radius of the exact Fresnel zone directly at A and B is simply obtained from equation (4),

$$r_{\text{exact}}(A) = r_{\text{exact}}(B) = \frac{\lambda}{2}\frac{1 + \lambda/4\ell}{1 + \lambda/2\ell}.$$

For $\ell \gg \lambda$, we obtain approximately $r_{\text{exact}}(A) = r_{\text{exact}}(B) \sim \lambda/2$. In paraxial computations, however, the Fresnel zones at A and B shrink to zero, see equation (5). Similarly, for the "overshooting" Δ of the exact Fresnel volume behind A and B along the x-axis (for $y_F = z_F = 0$), we obtain from equation (4), $\Delta = \lambda/4$. The paraxial computations do not give any overshooting.

Equation (5) and Figure 2 allow us to draw some conclusions regarding the typical sizes of the Fresnel volumes and Fresnel zones in homogeneous media. For example, let us compute the radius of the Fresnel zone at the middle point between points A, B. Then $x_F - x_A = x_B - x_F = \frac{1}{2}(x_B - x_A) = \frac{1}{2}\ell$, and equation (5) yields $r = \frac{1}{2}(\lambda\ell)^{1/2}$. The same equation is valid for the radius of the Fresnel zone at a plane interface between two homogeneous media, if a reflected wave with the source and receiver situated at the same point is considered (normal incidence), and if the distance of the source from the interface is $\frac{1}{2}\ell$. Similar analytic expressions for Fresnel zones in simple structures have been known for a long time. See, for example,Flatté et al. (1979), Born and Wolf (1980), Sheriff (1980), Kravtsov and Orlov (1980), etc. Most of them are also only approximate, i.e., based on paraxial methods, even though the authors do not emphasize this fact.

In laterally varying layered structures, the computation of Fresnel zones is considerably more complicated. The most general approach for the evaluation of Fresnel zones along the rays in complex structures was proposed in Gelchinsky (1985). To evaluate the Fresnel zone at a selected point of the ray, he uses a geometrical approach based on the curvatures of the wavefront. Gelchinsky traces two wavefronts, one from point A and one from point B; however, he does not specify how to evaluate the curvature matrix of the wavefront along the ray in an inhomogeneous medium. The computation of the curvature matrix in an inhomogeneous medium along the ray can be done by solving a nonlinear matrix equation of the Riccati type. Such computations are usually less efficient. An alternative approach to compute the curvature matrix is based on a linear dynamic ray-tracing system. Then, however, the evaluation of the curvature matrix is not needed at all, i.e., the equations for the Fresnel zone parameters may be obtained directly, in a simple way See more details on the curvature matrix computation with both approaches in Hubral (1980), Hubral and Krey (1980) and Červený (1985, 1987).

In case of inhomogeneous media with curved interfaces the situation can become complicated in another way. Th Fresnel zones are not necessarily elliptical, but may also b hyperbolical or parabolical. For a detailed discussion hyperbolical Fresnel zones and their physical interpretatic see Asatryan and Kravtsov (1988).

A final note. In the whole treatment, we have considered harmonic waves, with a frequency f. In the case of actual seismic waves, however, we do not have harmonic waves, but usually some high-frequency signals. The definition of the Fresnel volume will remain approximately valid only for very-narrow-band-limited high-frequency signals, if the dominant frequency is used for f. For signals that are not very-narrow-band-limited, it will be necessary perhaps to consider several Fresnel volumes for different frequencies. It would also be possible to use an alternative definition of Fresnel volumes in terms of transient waves, with T representing the width of the signal. [See also Knapp (1991) and a discussion of *band-limited raypaths* from a different point of view in Woodward (1989).]

PARAXIAL FRESNEL VOLUMES IN 3-D STRUCTURES

In this section, we shall present equations for the paraxial Fresnel volumes in 3-D laterally varying layered and blocked structures. The derivation is based on the principles of the paraxial ray method (see Babich and Buldyrev, 1972; Červený and Pšenčík, 1983; Červený et al., 1984, 1988; Beydoun and Keho, 1987) and on the properties of the ray propagator matrix. For a detailed exposition of the paraxial ray method and, particularly, for the properties of the ray propagator matrix see Červený (1985, 1987, 1989b).

Paraxial ray method in 3-D smooth structures

Let us consider the ray Ω connecting two points A, B. The ray Ω can be described by the parametric equation $x_i = x_i(s)$, where x_i are Cartesian coordinates of points along the ray Ω, and s is the arclength of the ray, measured from the reference point $s = s_0$ on the ray, situated at A. The ray trajectory $x_i = x_i(s)$ satisfies the well-known ray-tracing equations. At any point of the ray Ω, we also determine the traveltime $\tau(s)$, the slowness vector $\mathbf{p}(s) = \nabla\tau = \mathbf{t}/v$, where $\mathbf{t}$ is the unit normal to the wavefront $\tau(x_i) = const.$ and v is the propagation velocity ($v = \alpha$ for P-waves, $v = \beta$ for S-waves). Along the ray Ω, we introduce the orthogonal ray centered coordinate system q_1, q_2, $q_3(\equiv s)$ and relevant basis vectors $\mathbf{e}_1$, $\mathbf{e}_2$, $\mathbf{e}_3(\equiv \mathbf{t})$. Directly along the ray Ω we have $q_1 = q_2 = 0$.

We perform the dynamic ray tracing in ray centered coordinates along Ω from A to B and determine the 4×4 ray propagator matrix $\underline{\Pi}(s, s_0)$. At the initial point $s = s_0$, the ray propagator matrix $\underline{\Pi}(s_0, s_0)$ equals the 4×4 identity matrix. We introduce four auxiliary 2×2 matrices $\underline{\mathbf{Q}}_1(s, s_0)$, $\underline{\mathbf{Q}}_2(s, s_0)$, $\underline{\mathbf{P}}_1(s, s_0)$, $\underline{\mathbf{P}}_2(s, s_0)$ by the relation

$$\underline{\Pi}(s, s_0) = \begin{pmatrix} \underline{\mathbf{Q}}_1(s, s_0) & \underline{\mathbf{Q}}_2(s, s_0) \\ \underline{\mathbf{P}}_1(s, s_0) & \underline{\mathbf{P}}_2(s, s_0) \end{pmatrix}. \tag{6}$$

Along the ray Ω, the ray propagator matrix satisfies the chain property $\underline{\Pi}(s, s_0) = \underline{\Pi}(s, s')\underline{\Pi}(s', s_0)$, where s' is any point on Ω, and its inverse is given by the relation,

$$\underline{\Pi}^{-1}(s, s_0) = \underline{\Pi}(s_0, s) = \begin{pmatrix} \underline{\mathbf{P}}_2^T(s, s_0) & -\underline{\mathbf{Q}}_2^T(s, s_0) \\ -\underline{\mathbf{P}}_1^T(s, s_0) & \underline{\mathbf{Q}}_1^T(s, s_0) \end{pmatrix}. \tag{7}$$

In the ray centered coordinates, the traveltime field $\tau(q_1, q_2, s)$ at a point situated *in the vicinity of the ray* Ω, specified by coordinates q_1, q_2, $q_3 \equiv s$ is approximately given by the relation,

$$\tau(q_1, q_2, s) = \tau(0, 0, s) + \tfrac{1}{2}\underline{\mathbf{q}}^T\underline{\mathbf{M}}(s)\underline{\mathbf{q}}, \quad \underline{\mathbf{q}} = \begin{pmatrix} q_1 \\ q_2 \end{pmatrix}. \tag{8}$$

Here $\underline{\mathbf{M}}(s)$ is a 2×2 matrix of second derivatives of the traveltime field with respect to q_1, q_2 at Ω,

$$M_{IJ}(s) = \left[\frac{\partial^2\tau(q_1, q_2, s)}{\partial q_I \partial q_J}\right]_{q_1 = q_2 = 0}. \tag{9}$$

The superscript T in equation (8) denotes a transpose. It is obvious that the matrix $\underline{\mathbf{M}}$ is symmetric.

The matrix $\underline{\mathbf{M}}$ can be expressed in terms of the ray propagator matrix (6). We can write

$$\underline{\mathbf{M}}(s) = \underline{\mathbf{P}}(s)\underline{\mathbf{Q}}^{-1}(s), \tag{10}$$

where $\underline{\mathbf{P}}(s)$ and $\underline{\mathbf{Q}}(s)$ are given by the following equations:

$$Q_{IJ} = \left(\frac{\partial q_I}{\partial \gamma_J}\right)_{q_1 = q_2 = 0}, \qquad P_{IJ} = \left(\frac{\partial^2\tau}{\partial q_I \partial \gamma_J}\right)_{q_1 = q_2 = 0},$$

where γ_1, γ_2 are ray parameters. $\underline{\mathbf{P}}(s)$ and $\underline{\mathbf{Q}}(s)$ are solutions of the dynamic ray-tracing system. They satisfy the continuation relation

$$\begin{pmatrix} \underline{\mathbf{Q}}(s) \\ \underline{\mathbf{P}}(s) \end{pmatrix} = \underline{\Pi}(s, s_0)\begin{pmatrix} \underline{\mathbf{Q}}(s_0) \\ \underline{\mathbf{P}}(s_0) \end{pmatrix}. \tag{11}$$

For a point source situated at s_0, we have $\underline{\mathbf{Q}}(s_0) = \mathbf{0}$.

The above relations play a very important role in the compact formulation and computation of paraxial Fresnel volumes.

Paraxial Fresnel volumes in 3-D smooth structures

We shall again consider the ray Ω connecting two points A, B. We wish to construct the Fresnel volume corresponding to the ray Ω with endpoints A, B (point source, receiver). Let us select an arbitrary point O_F on the ray Ω between A and B (see Figure 1). At O_F, we construct a plane Σ_F perpendicular to Ω. Finally, we choose a point F in the plane Σ_F. According to the definition, the point F belongs to the Fresnel volume corresponding to Ω with endpoints A, B if and only if the following condition is satisfied,

$$|\tau(F, A) + \tau(F, B) - \tau(B, A)| \le \tfrac{1}{2}T. \tag{12}$$

Here T is the period, and $\tau(B, A) = \tau(A, B)$ corresponds to the traveltime from A to B. The quantities $\tau(F, A)$ and $\tau(F, B)$ have a similar meaning.

To compute $\tau(F, A)$ and $\tau(F, B)$ for a specific point F in a laterally varying structure, it would be necessary to perform exhaustive numerical two-point ray tracing. If the point F, however, is not too far from Ω, we can use an analytical approach based on the paraxial ray method. This will reduce all the work to only a few matrix multiplications.

We shall introduce the following convention. If we write the matrix $\underline{\mathbf{M}}$ with two arguments, e.g., $\underline{\mathbf{M}}(O_F, A)$, it corresponds to the matrix of second derivatives of the

traveltime field at point O_F due to a *point source situated at* A. Similarly, $\underline{\mathbf{M}}(O_F, B)$ is due to a point source at B. A similar convention will also be used for matrices $\underline{\mathbf{Q}}$ and $\underline{\mathbf{P}}$.

We shall now specify the ray centered coordinate system q_1, q_2, q_3. We shall assume that the coordinate $q_3 \equiv s$ increases along Ω from A to B, and denote the ray centered coordinates of points O_F and F as follows, $O_F(0, 0, s)$, $F(q_1, q_2, s)$. To emphasize the fact that q_1, q_2 are coordinates of the point F, we shall write $q_1(F)$ and $q_2(F)$.

Then, using equation (8), we can write,

$$\tau(F, A) = \tau(0_F, A) + \tfrac{1}{2}\mathbf{q}^T(F)\underline{\mathbf{M}}(O_F, A)\mathbf{q}(F). \quad (13)$$

Similarly, we obtain

$$\tau(F, B) = \tau(0_F, B) - \tfrac{1}{2}\mathbf{q}^T(F)\underline{\mathbf{M}}(O_F, B)\mathbf{q}(F). \quad (14)$$

Note that equation (14) corresponds to the same ray centered coordinate system $q_1, q_2, q_3 \equiv s$ as equation (13), with the same arclength s along Ω, increasing from A to B. Thus, equation (14) corresponds to a *backward* continuation and the sign "$-$" must be used with the quadratic term. Even the quantities $\underline{\mathbf{M}}(O_F, A)$ and $\underline{\mathbf{M}}(O_F, B)$ are defined with respect to the same ray centered coordinate system $q_1, q_2, q_3 = s$. For example, in a homogeneous medium, elements of $\underline{\mathbf{M}}(O_F, A)$ are positive, but elements of $\underline{\mathbf{M}}(O_F, B)$ are negative.

We now take into account that $\tau(O_F, A) + \tau(O_F, B) = \tau(B, A)$. Inserting equations (13) and (14) into equation (12) yields the final equation for the paraxial Fresnel volume,

$$|\mathbf{q}^T(F)[\underline{\mathbf{M}}(O_F, A) - \underline{\mathbf{M}}(O_F, B)]\mathbf{q}(F)| \le T. \quad (15)$$

Similarly, the boundary of the paraxial Fresnel volume is composed of points F which satisfy the equation,

$$|\mathbf{q}^T(F)[\underline{\mathbf{M}}(O_F, A) - \underline{\mathbf{M}}(O_F, B)]\mathbf{q}(F)| = T. \quad (16)$$

Let us now consider a fixed point O_F, with a relevant plane Σ_F perpendicular to ray Ω at O_F. Then equation (15) represents a normal cross-section of the paraxial Fresnel volume with the plane Σ_F. We call this cross-section the *Fresnel zone*. From a physical point of view, it corresponds to the first Fresnel zone.

The left-hand sides of equations (15) and (16) are real valued symmetric quadratic forms, and equation (16) represents a quadratic curve in the plane Σ_F. The curve may be a circle (not common in laterally varying structures), an ellipse, a parabola, or a hyperbola. To simplify the terminology, we shall discuss the *Fresnel ellipse*. However, it should be understood that the curve may be any quadratic curve, not only an ellipse.

Equations (15) and (16) represent final equations for the paraxial Fresnel volume and for its boundary. It will, however, be useful to discuss the computation of matrices $\underline{\mathbf{M}}(O_F, A)$ and $\underline{\mathbf{M}}(O_F, B)$. In principle, it would be possible to use a *hungry wolf* approach and to perform the dynamic ray tracing along the Ω twice, once from the point A to B and second from B to A. In the second case, it would be necessary to use the same choice of ray centered coordinate system as in the first case. In addition, it would be necessary to choose proper initial conditions for matrices $\underline{\mathbf{P}}(A)$ and $\underline{\mathbf{P}}(B)$. Note that $\underline{\mathbf{Q}}(A) = \mathbf{0}$ for a point source at A, and $\underline{\mathbf{Q}}(B) = \mathbf{0}$ for a point source at B.

It is, however, possible to express $\underline{\mathbf{M}}(O_F, A)$ and $\underline{\mathbf{M}}(O_F, B)$ in terms of the minors of the ray propagator matrix and remove all the difficulties mentioned above. It is not necessary to perform the dynamic ray tracing twice, but just once, from A to B. No actual initial conditions for matrices $\underline{\mathbf{P}}(A)$ and $\underline{\mathbf{P}}(B)$ are required.

Using equations (10) and (11), we obtain the following equation for $\underline{\mathbf{M}}(O_F, A)$,

$$\underline{\mathbf{M}}(O_F, A) = \underline{\mathbf{P}}_2(O_F, A)\underline{\mathbf{Q}}_2^{-1}(O_F, A). \quad (17)$$

Thus, to determine $\underline{\mathbf{M}}(O_F, A)$, we only need to know two minors of the ray propagator matrix $\underline{\mathbf{\Pi}}(O_F, A)$: $\underline{\mathbf{P}}_2(O_F, A)$ and $\underline{\mathbf{Q}}_2(O_F, A)$. Initial conditions for $\underline{\mathbf{P}}(A)$ are not required.

An equation for $\underline{\mathbf{M}}(O_F, B)$ is more complex, as we want to express it in terms of elements of the ray propagator matrix $\underline{\mathbf{\Pi}}(O_F, A)$, not $\underline{\mathbf{\Pi}}(O_F, B)$. We shall show that this is possible, if the ray propagator matrix $\underline{\mathbf{\Pi}}(B, A)$ along the whole ray Ω from A to B is also known. The matrix $\underline{\mathbf{\Pi}}(B, A)$ is, of course, known when we perform the dynamic ray tracing along the whole ray Ω. If we use the chain property and equation (7) for the inverse of the ray propagator matrix (6), we obtain,

$$\begin{aligned}\underline{\mathbf{M}}(O_F, B) &= [-\underline{\mathbf{P}}_1(O_F, A)\underline{\mathbf{Q}}_2^T(B, A) \\ &+ \underline{\mathbf{P}}_2(O_F, A)\underline{\mathbf{Q}}_1^T(B, A)] \times [-\underline{\mathbf{Q}}_1(O_F, A)\underline{\mathbf{Q}}_2^T(B, A) \\ &+ \underline{\mathbf{Q}}_2(O_F, A)\underline{\mathbf{Q}}_1^T(B, A)]^{-1}. \end{aligned} \quad (18)$$

Equations (15) and (16), together with (17) and (18), are final equations for the paraxial Fresnel volume and its boundary. As soon as the minors of the ray propagator matrices $\underline{\mathbf{\Pi}}(O_F, A)$ and $\underline{\mathbf{\Pi}}(B, A)$ are known, the boundary of the paraxial Fresnel volume in the plane Σ_F perpendicular to the ray Ω at O_F can be computed analytically. When these minors are known at all points O_F of Ω, including the endpoint B, the whole paraxial Fresnel volume and its boundary can be analytically computed. An alternative version of several equations derived above was also presented, without derivation, in Červený et al. (1988).

Note that nowadays the minors of the ray propagator matrix are routinely evaluated in most of the existing program packages for numerical modeling of seismic wavefields in 2-D and 3-D complex structures. Because they are needed in many applications, the cost of a Fresnel volume computation is extremely low.

The final expressions (15)–(18) for the paraxial Fresnel volume and its boundary contain only the minors of the ray propagator matrices $\underline{\mathbf{\Pi}}(O_F, A)$ and $\underline{\mathbf{\Pi}}(B, A)$. These expressions remain valid even for any laterally varying structures *with curved interfaces*, if proper expressions for the ray propagator matrix are used (see Červený, 1989b).

Boundary of the paraxial Fresnel volume and Fresnel ellipse

The boundary of the paraxial Fresnel volume in the plane Σ_F, perpendicular to the ray Ω at the point O_F, is given by equation (16), with equations (17) and (18). We shall now rewrite equation (16) as a diagonal form. As the 2×2 matrices $\underline{\mathbf{M}}(O_F, A)$ and $\underline{\mathbf{M}}(O_F, B)$ are real-valued and symmetric, matrix $\underline{\mathbf{M}}(O_F, A) - \underline{\mathbf{M}}(O_F, B)$ has two real-valued eigenvalues. They are denoted by $M_1(O_F)$ and

$M_2(O_F)$. Similarly, we denote the relevant eigenvectors by $\mathbf{e}_1^M(O_F)$ and $\mathbf{e}_2^M(O_F)$. Then we can write,

$$\underline{\mathbf{M}}(O_F, A) - \underline{\mathbf{M}}(O_F, B) = \underline{\mathbf{R}}^T(O_F)\begin{pmatrix} M_1(O_F) & 0 \\ 0 & M_2(O_F) \end{pmatrix}\underline{\mathbf{R}}(O_F). \quad (19)$$

Here $\underline{\mathbf{R}}(O_F)$ is a rotation matrix that rotates the basis vectors $\mathbf{e}_1(O_F)$ and $\mathbf{e}_2(O_F)$ into eigenvectors $\mathbf{e}_1^M(O_F)$ and $\mathbf{e}_2^M(O_F)$. Its elements are components of the eigenvectors $\mathbf{e}_1^M$ and $\mathbf{e}_2^M$ into axes q_1 and q_2. Then we can write the quadratic form (16) in the following diagonalized form,

$$\left|\underline{\mathbf{q}}'^T(F)\begin{pmatrix} M_1(O_F) & 0 \\ 0 & M_2(O_F) \end{pmatrix}\underline{\mathbf{q}}'(F)\right| = T, \quad \underline{\mathbf{q}}' = \begin{pmatrix} q_1' \\ q_2' \end{pmatrix}. \quad (20)$$

Here q_1' and q_2' are new local Cartesian coordinates in the plane Σ_F. The axes q_1' and q_2' are oriented along the eigenvectors $\mathbf{e}_1^M(O_F)$ and $\mathbf{e}_2^M(O_F)$. Equation (20) yields,

$$|q_1'^2(F)M_1(O_F) + q_2'^2(F)M_2(O_F)| = T. \quad (21)$$

For $M_1(O_F) > 0$ and $M_2(O_F) > 0$, equation (21) represents a *Fresnel ellipse*. The half-axes of the Fresnel ellipse, $r_1(O_F)$ and $r_2(O_F)$, are given by relations,

$$r_1(O_F) = \left[\frac{T}{M_1(O_F)}\right]^{1/2}, \quad r_2(O_F) = \left[\frac{T}{M_2(O_F)}\right]^{1/2}. \quad (22)$$

These are final equations for the half-axes of the Fresnel ellipse in the plane Σ_F. They can be used to find the dimensions of the Fresnel ellipse at any point O_F of the ray Ω in a laterally varying layered 3-D structure. For $M_1(O_F).M_2(O_F) < 0$, the *Fresnel hyperbola* is obtained.

PARAXIAL FRESNEL VOLUMES IN 2-D STRUCTURES

Equations for the paraxial Fresnel volumes simplify considerably for *plane rays* Ω. Here we shall discuss an important special case of plane rays Ω, particularly the rays in a 2-D medium situated in the plane Σ perpendicular to the axis of symmetry. We specify the triplet of the basis vectors $\mathbf{e}_1(s_0)$, $\mathbf{e}_2(s_0)$, $\mathbf{e}_3(s_0) \equiv \mathbf{t}(s_0)$ at the initial point A in such a way that $\mathbf{e}_2(s_0)$ is perpendicular to Σ. The two other basis vectors are given by the relations $\mathbf{e}_3(s_0) = v(s_0)\mathbf{p}(s_0)$, $\mathbf{e}_1(s_0) = \mathbf{e}_2(s_0) \times \mathbf{e}_3(s_0)$. Then $\mathbf{e}_2$ is perpendicular to Σ along the whole ray Ω, $\mathbf{e}_2(s) = \mathbf{e}_2(s_0)$, and $\mathbf{e}_3(s)$, $\mathbf{e}_1(s)$ are given, for any s, by the same relations as at s_0: $\mathbf{e}_3(s) = v(s)\mathbf{p}(s)$, $\mathbf{e}_1(s) = \mathbf{e}_2(s) \times \mathbf{e}_3(s)$. The plane Σ_F is perpendicular to Σ along the whole ray Ω and the matrices $\underline{\mathbf{M}}(O_F, A)$, $\underline{\mathbf{M}}(O_F, B)$, are diagonalized ($M_{12} = M_{21} = 0$) with the diagonal elements $M_{11} = M^{\parallel}$ and $M_{22} = M^{\perp}$. Here $M^{\parallel}$ denotes the in-plane second derivative of the traveltime with respect to q_1, in the plane Σ. Similarly, $M^{\perp}$ denotes the perpendicular-to-the-plane second derivative, with respect to q_2, along the unit vector $\mathbf{e}_2$. Expressions (19) then remain valid, but $\underline{\mathbf{R}}$ is an identity matrix, and $M_1(O_F)$, $M_2(O_F)$ are given by relations,

$$M_1(O_F) = M^{\parallel}(O_F, A) - M^{\parallel}(O_F, B),$$
$$M_2(O_F) = M^{\perp}(O_F, A) - M^{\perp}(O_F, B). \quad (23)$$

Similarly, equations (20)–(22) remain valid. The final expressions for the radii of the Fresnel ellipse $r_1(O_F)$ and $r_2(O_F)$ are given by equation (22), with equation (23). In the analogy with $M^{\parallel}$ and $M^{\perp}$, we shall also use the notation $r^{\parallel}(O_F)$ for $r_1(O_F)$, and $r^{\perp}(O_F)$ for $r_2(O_F)$. The quantities $r^{\parallel}(O_F)$ and $r^{\perp}(O_F)$ have a simple physical meaning: $r^{\parallel}(O_F)$ represents the in-plane radius of the Fresnel ellipse, and $r^{\perp}(O_F)$ the radius measured along $\mathbf{e}_2$, in the direction perpendicular to Σ.

FRESNEL VOLUME RAY TRACING IN 2-D LATERALLY VARYING LAYERED STRUCTURES

In this section, we shall briefly describe an algorithm and computer programs for the Fresnel volume ray tracing in 2-D laterally varying structures containing curved interfaces. We shall also present examples of numerical calculations. In the whole section, we call the paraxial Fresnel volumes simply, the Fresnel volumes.

Algorithm of Fresnel volume ray tracing

Assume that a program package for a 2-D numerical ray tracing and traveltime computation is available. For each calculated ray, the program package should yield the Cartesian coordinates of points situated along the ray and certain additional quantities at these points (traveltime, components of slowness vector, etc.). Assume also that the program package performs dynamic ray tracing and calculates the ray propagator matrix at all evaluated points along the ray. If such a program package is available, the algorithm for the Fresnel volume ray tracing is straightforward. In the first step, no changes are made in the computations described above, and only a supplementary file containing some computed quantities is generated. As soon as such a file is available for a selected ray (or rays), the Fresnel volume(s) corresponding to the selected ray(s) can be computed and plotted using a supplementary program.

The program package BEAM87, described briefly in Červený (1989a), was used to generate the file described above. Many other recently available program packages could, of course, be used alternatively, e.g., the program package SEIS83 as described in Červený and Pšenčík (1984). The program package BEAM87 is designed to perform the ray tracing and dynamic ray tracing and to compute amplitudes, synthetic seismograms, and particle ground motion diagrams in 2-D laterally varying layered structures. The structure of the model may be rather general, with blocks, pinch-outs, and isolated bodies. Any type of multiply reflected, P, S, or converted wave, can be considered as optional. The point source A may be situated at any point of the medium, with the receivers (B) along the earth's surface.

To plot the results of Fresnel volume ray tracing, two methods are used. In both methods, the mathematical ray under consideration is plotted first. In the first method, the radii of Fresnel zones $r^{\parallel}(O_F)$ (or $r^{\perp}(O_F)$) are plotted discretely, in the direction perpendicular to the mathematical ray at points O_F. We shall refer to it as discrete presentation of Fresnel volumes. For examples, see Figures 8, 10, and 11. The advantage of the discrete presentation is an extreme simplification of the generated plots. The disadvantage consists of a complicated behavior close to the interfaces. As the ray is not generally perpendicular to the

interface, the abscissas, with the radii of Fresnel zones, partially intersect the interfaces (see Figures 10 and 11). In the second method, the Fresnel volumes are plotted continuously by a linear interpolation from the discrete presentation. We shall refer to it as continuous presentation of Fresnel volumes (see Figures 3, 4, and 5 for examples). Such a presentation, however, requires a little more numerical effort, particularly close to interfaces. We feel that the simple discrete presentation is quite sufficient for most practical purposes.

In all the examples, only the in-plane radii of the Fresnel zones $r^{\parallel}$ will be presented. The behavior of $r^{\perp}$ is simple and is not discussed here. All computations were performed by the paraxial ray method, so that the pictures correspond to paraxial Fresnel volumes.

Fresnel volumes of reflected/transmitted rays

The Fresnel zone with radii $r^{\parallel}$ and $r^{\perp}$ represents an intersection of the Fresnel volume with a plane perpendicular to the ray. Sometimes, however, a calculation of the intersection of the Fresnel volume is required, with an arbitrarily oriented surface Σ (not necessarily perpendicular to the ray) which may also be curved.

In the framework of the paraxial ray method, it is possible to evaluate the parameters of such an intersection analytically. We call the intersection of the Fresnel volume with Σ the *Fresnel zone on the surface* Σ. From a mathematical point of view, the problem of determining the Fresnel zone on the surface Σ practically reduces to the problem of the determination of the traveltime field generated by a point source along a curved surface. In the paraxial ray approximation, this can be done simply. Such a problem is solved, e.g., in Červený [1985, Eq. (7.9)] and will not be discussed here.

Such equations are applicable even for Fresnel zones at interfaces. It is not difficult to prove that the boundary of the Fresnel volume is continuous across the interface.

Simple examples of Fresnel volumes of reflected *P*-waves are shown in Figures 4 and 5. The continuous presentation of Fresnel volumes is used.

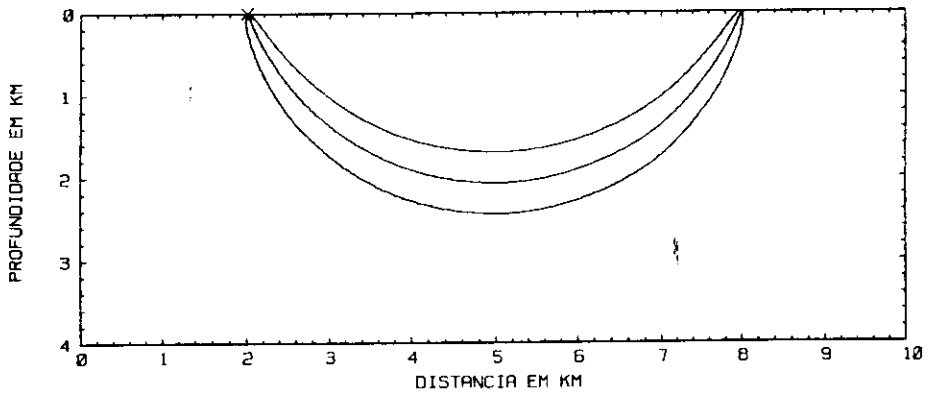

FIG. 3. Example of the paraxial Fresnel volume of a direct *P*-wave in a vertically inhomogeneous medium with a positive constant velocity gradient, $v(z) = 1 + 0.875z$ km/s. The frequency is $f = 30$ Hz.

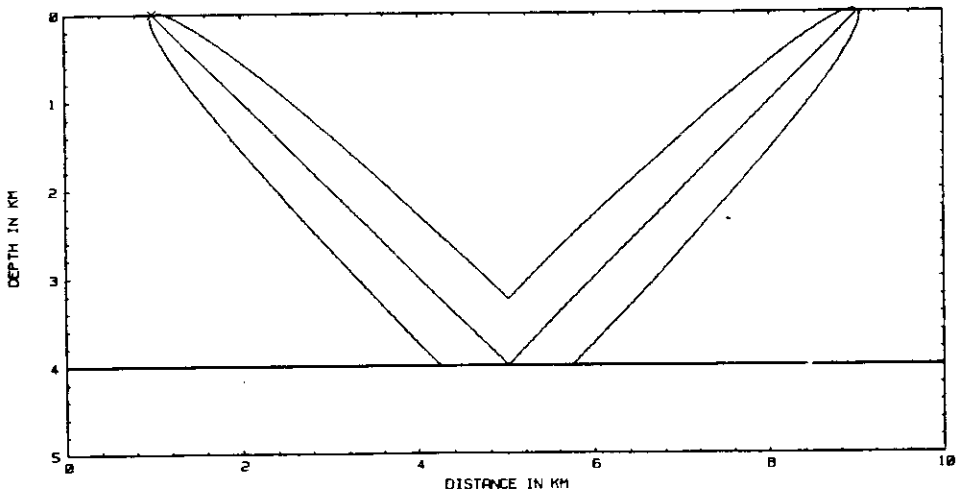

FIG. 4. Example of the paraxial Fresnel volume of a *PP*-reflected wave in a two-layer medium. The velocity in the upper layer is 3 km/s, and in the bottom layer 6.5 km/s. The frequency is $f = 30$ Hz. The penetration of the Fresnel volume below the reflector is not shown. (See text for more details.)

We add one note concerning Fresnel volumes of reflected waves. The *exact Fresnel volume* of the reflected wave does not stop abruptly at the reflector, as shown in Figures 4 and 5, but extends slightly, even below the reflector. Actually, a point F situated below the reflector close to the point of incidence may satisfy the Fresnel volume condition (1). This is well known from literature, see e.g., Hagedoorn (1959) and Sheriff and Geldart (1982). For example, the maximum penetration below the interface for a normal incidence is $\frac{1}{4}\lambda$, where λ is the wavelength below the interface. Such a penetration is not automatically included in the *paraxial Fresnel volume computation* and is not shown in figures presented here. Perhaps, it will not be difficult to supplement the paraxial procedure by some simple estimates, similarly, as in the vicinity of the source and receiver, and to plot the boundary of the Fresnel volume even below the interface.

Fresnel volumes close to caustic points

Let us consider the point source situated at A and a caustic point C on Ω between A and B. At the caustic point C, the ray Ω touches an envelope of rays and $|M^{\parallel}(O_F, A)| \to \infty$ for $O_F \to C$. Consequently,

$$r^{\parallel}(C) = 0.$$

Thus, at a caustic point C, the radius of the Fresnel zone $r^{\parallel}(C)$ vanishes. Before we present numerical examples illustrating this fact, we shall discuss in greater detail one interesting effect connected with the caustic points.

Let us consider a ray of a direct wave from A to B in a 1-D vertically inhomogeneous medium (see Figure 6). It is obvious that this ray is symmetrical about the vertical line passing through the minimum of the ray M.

First, assume that the point source is situated at A and the receiver at B (see Figure 6a). Consider a velocity-depth structure that generates a caustic point C between M and B. Let us now exchange the source and the receiver so that the receiver is situated at A and source at B. As the medium is 1-D, the caustic point must be situated at the same epicentral distance from the source as before. Thus, it will be situated at the point C', symmetrical to C.

Similarly as $M^{\parallel}(C, A) \to \infty$, we also have $M^{\parallel}(C', B) \to \infty$. Equations (22) and (23) then yield that the Fresnel volume vanishes not only at C, but also at C'. Thus, if the structure is 1-D, not only is the mathematical ray from A to B fully symmetrical about the vertical line passing through M, but also the Fresnel volume is symmetrical, including the two symmetrical caustic points C and C' for sources at A and B. We call this effect the *double caustic effect*.

We emphasize again: for a *fixed source at A* and *fixed receiver at B*, only the caustic point at C is real; the ray field is quite regular at C'. The relevant paraxial Fresnel volume, however, shrinks to zero not only at C, but also at C'.

The double caustic effect is very common in Fresnel volume ray tracing. Of course, the equations presented yield the double caustic effect automatically.

The double caustic effect is common not only in the case of symmetrical rays Ω, but also in case of rays in laterally varying layered structures with curved, nonsymmetrical interfaces. The rays in such structures are not symmetrical, but the caustic C (corresponding to the source at A) and C'

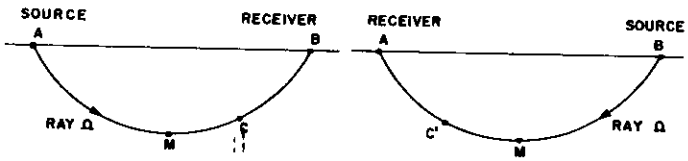

FIG. 6. Explanation of the double caustic effect using the principle of reciprocity. For the source at A, the caustic point is situated at C. For the source at B, the caustic point is situated at C'. At both these points, the width of the paraxial Fresnel volume shrinks to zero.

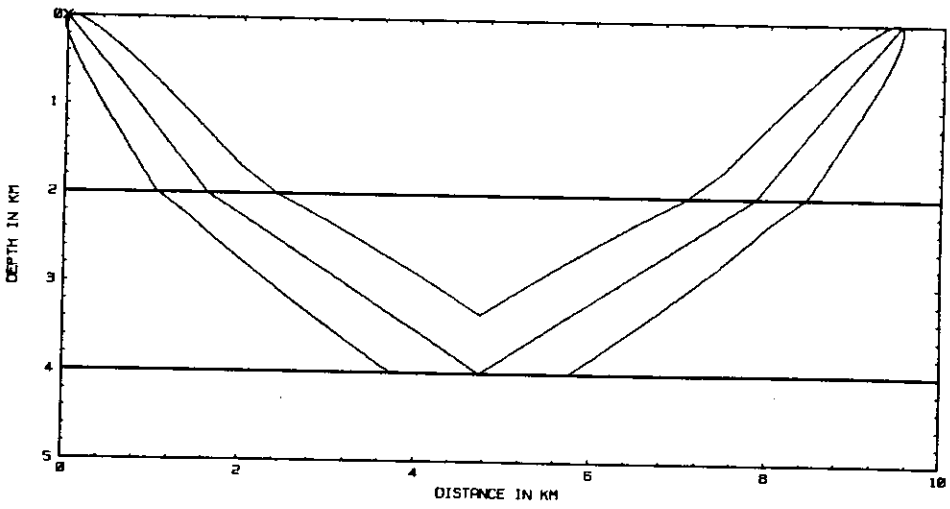

FIG. 5. Example of the paraxial Fresnel volume of a *PP*-reflected wave in a three-layered medium. The velocities in individual layers are 3 km/s, 4 km/s, and 6.5 km/s, from the top to the bottom. The frequency is 30 Hz. The penetration of the Fresnel volume below the reflector is not shown. (See text for more details.)

(corresponding to the source at B) will usually influence the shape of the Fresnel volume.

Examples of the double caustic effect are shown in Figures 7–10. In Figures 7 and 8, we consider a vertically inhomogeneous medium with a velocity-depth distribution $v(z)$ specified by a quadratic parabola $v(z) = 5.6 - 0.036z + 0.0024z^2$ (km/s). Here z is taken in kilometers, $z = 0$ corresponds to the earth's surface. This velocity depth distribution yields $v(0) = v(15) = 5.6$ km/s and $v(40) = 8$ km/s. The lowest velocity is reached at $z = 7.5$ km, $v(7.5) = 5.465$ km/s. The ray diagram (initial value ray tracing) and the traveltime curve, corresponding to a point source situated at the earth's surface, are shown in Figure 7. The Fresnel volumes corresponding to a selected ray, for frequencies of 5 Hz and 10 Hz, are shown in Figure 8. The discrete presentation of Fresnel volume is used.

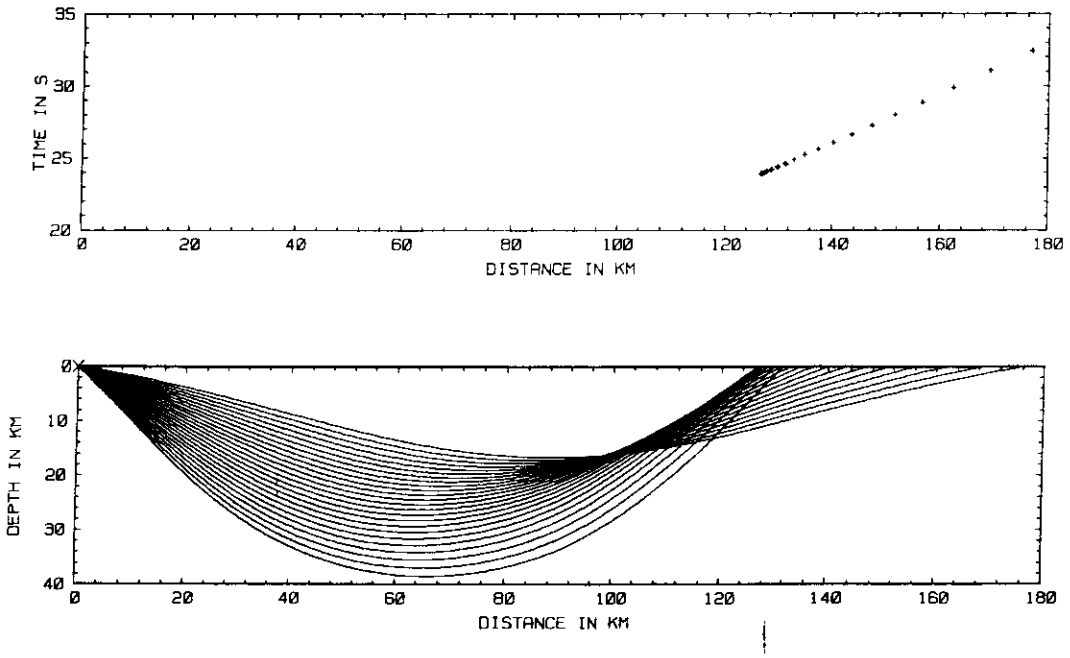

FIG. 7. The ray diagram and traveltime-distance curve of a direct wave in a vertically inhomogeneous medium with the velocity depth distribution given by the relation $v(z) = 5.6 - 0.036z + 0.0024z^2$ km/s. An envelope of rays (a caustic) is formed in the ray diagram. The caustic intersects the surface at the epicentral distance of 126 km.

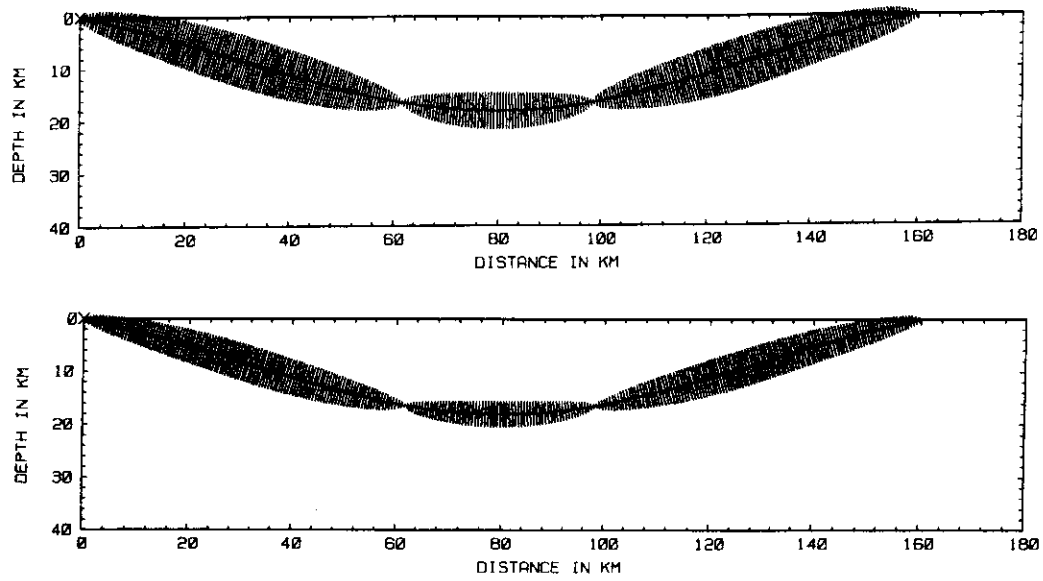

FIG. 8. Double caustic effect. The paraxial Fresnel volumes for one ray of the direct wave in the model shown in Figure 7 which passes through a caustic point at an epicentral distance of about 98 km. The freuqencies are 5 Hz and 10 Hz.

In another example, we consider a wave reflected from an interface of the syncline form. The ray diagram (initial value ray tracing) and the traveltime curves for a point source situated on the axis of symmetry of the model are shown in Figure 9. A Fresnel volume corresponding to one selected mathematical ray, for frequency of 30 Hz, is shown in Figure 10. The discrete presentation of the Fresnel volume is used again.

Remember that the Fresnel volumes presented are evaluated by the paraxial ray method, which fails at caustic points. Actually, the Fresnel zone will not vanish at the caustic point, but it will be very small. The situation is very similar to the situation at the point source. The radius of the exact Fresnel zone at the point source is $\frac{1}{2}\lambda$, but the paraxial Fresnel zone vanishes there. Thus, we can expect a radius of the Fresnel zone of the order of $\frac{1}{2}\lambda$, even at caustic points.

Fresnel volume ray tracing in complex 2-D layered structures

Using the algorithm proposed in this paper, we can compute the radii of the Fresnel zone by a simple step-by-step procedure in any laterally varying structure. The cost of the Fresnel volume ray tracing in 2-D layered structures does not significantly exceed the cost of standard ray tracing, as the evaluation of the radii of Fresnel zones requires only a simple algebraic manipulation.

We shall present several simple examples. The synthetic model under consideration contains curved interfaces, a lens-like isolated body, a pinch-out, and edge points of interfaces. The velocity distribution in individual layers changes slightly in both x- and z-directions. Fresnel volume ray tracing along a selected mathematical ray, is performed for four frequencies, 20 Hz, 30 Hz, 50 Hz, and 100 Hz (see Figure 11). The Fresnel volumes are presented in a discrete form.

As Figures 11 are self-explanatory, we shall not discuss them in detail here. Still, however, we shall point out that an edge point is situated close to the reflection point of the wave under consideration. For the frequency of 20 Hz, the edge point is situated within the Fresnel volume, but for the frequency of 100 Hz, it is situated safely outside the Fresnel volume. This implies that the wavefield recorded at the receiver will be influenced by the edge point for frequencies close to 20 Hz, but will not be influenced by it for frequencies close to 100 Hz. A similar situation is related to the pinch-out at the descending part of the ray Ω.

DISCUSSION AND CONCLUSIONS

We have presented a simple and efficient technique for Fresnel volume ray tracing. It yields the parameters of the Fresnel zones at any point of the ray, and can be applied to any type of seismic body wave propagating in 2-D and 3-D laterally varying layered structure.

As the technique practically does not require more computing time than the standard ray tracing, it can be included in routine computer packages to solve various direct inverse seismic problems. We shall discuss several possible applications.

The applications of the Fresnel volume ray tracing in the investigation of the horizontal resolution of seismic methods are well known and do not require any additional explanation. It should be emphasized only that the algorithm of the Fresnel volume ray tracing proposed here considerably

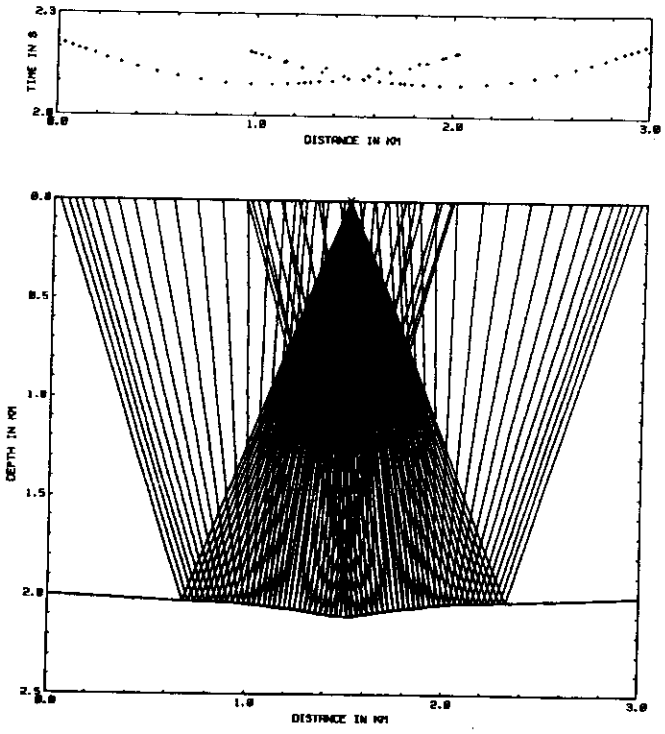

FIG. 9. The ray diagram and traveltime-distance curve of a wave reflected from a structural interface of a syncline form. The caustics can be clearly observed in the ray diagram. The velocity in the upper layer equals 2 km/s and 4 km/s in the bottom layer.

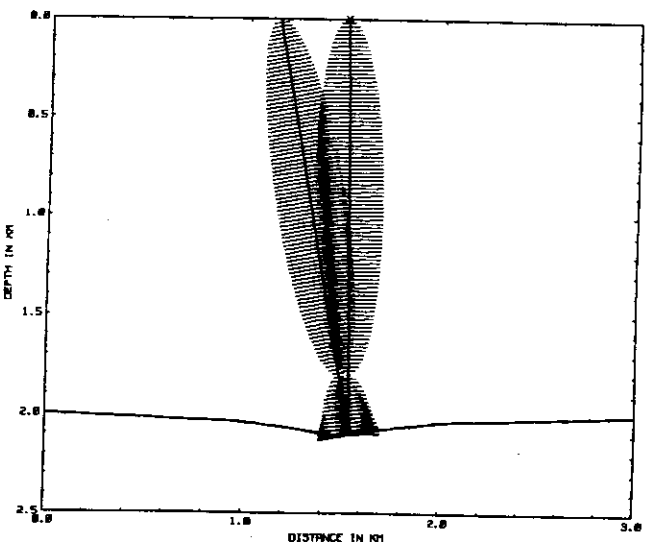

FIG. 10. Double caustic effect. The paraxial Fresnel volume for one ray of the reflected wave in the model shown in Figure 9 which passes through a caustic point. The frequency is 30 Hz.

extends the possibilities of such investigations for complex 2-D and 3-D laterally varying structures.

Another important application of the Fresnel volume ray tracing consists in possible routine computations of some quantitative estimates of the inaccuracy of the ray method and in a routine separation of regions where the ray method is or is not applicable. As this application is not as obvious, we shall discuss it in greater detail.

The validity conditions of the ray method have been discussed by many authors. For a detailed treatment and for many other references see Červený et al. (1977), Kravtsov and Orlov (1980), Chapman (1985), Beydoun and Ben-Menahem (1985), and Ben-Menahem and Beydoun (1985). The validity conditions usually have only a quantitative, not a quantitative character. Using the concept of the Fresnel volumes, the validity conditions can be expressed in a more quantitative way. We shall mainly follow the formulation and discussion of the Fresnel volume validity conditions given by Kravtsov and Orlov (1979, 1980). They propose two validity conditions:

1) The parameters of the medium and the parameters of the wave under consideration (amplitude, slowness vector) must not vary considerably within the cross-section of the relevant Fresnel volume.

If we denote the greater half-axis of the Fresnel zone by r_F, the validity conditions are as follows:

$$r_F \left| \frac{\nabla_\perp v}{v} \right| \ll 1, \qquad r_F \left| \frac{\nabla_\perp A_i}{A} \right| \ll 1,$$

$$r_F \left| \frac{\nabla_\perp p_i}{p} \right| \ll 1, \qquad \text{etc.} \tag{24}$$

Here $\nabla_\perp$ denotes the gradient in the direction perpendicular to the ray, p_i are components of the slowness vector, and A_i components of the amplitude vector. The physical meaning of the above inequalities is obvious.

2) The Fresnel volumes corresponding to different rays arriving at the receiver point must not substantially intersect each other.

We understand that two Fresnel volumes intersect each other substantially if the larger parts of the two Fresnel volumes overlap. The criterion may also be expressed in the following way,

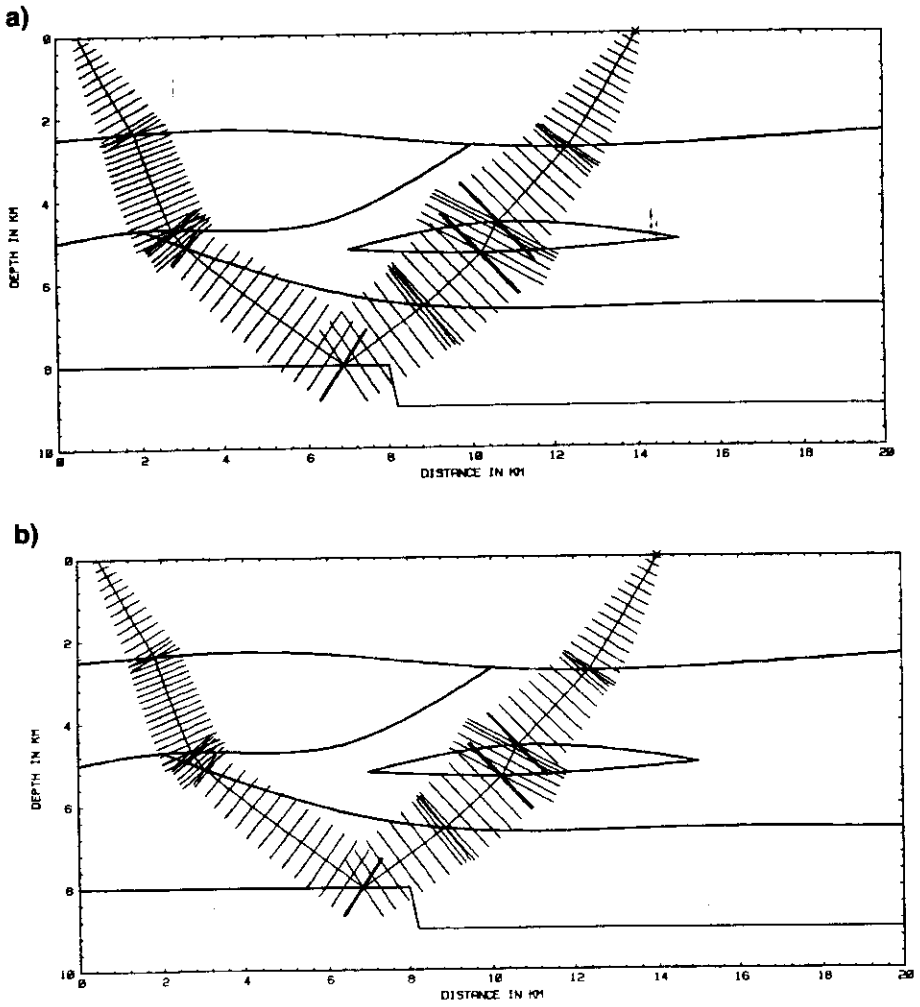

FIG. 11. Fresnel volume ray tracing in a complex 2-D laterally varying layered structure. The frequencies in individual figures are as follows: (a) $f = 20$ Hz, (b) $f = 30$ Hz, (c) $f = 50$ Hz, and (d) $f = 100$ Hz.

$$\frac{\delta V_F}{V_F} \ll 1. \tag{25}$$

Here V_F is a sum of both Fresnel volumes, and δV_F is the common (overlapping) part of the volumes.

According to Kravtsov and Orlov (1979, 1980), the criteria (24) and (25) are not only *necessary*, but also *universal and sufficient*. They investigated many special cases and found that the validity conditions (24) and (25) can replace many other forms of validity conditions of the ray method proposed by other authors. They also found that the signs $\ll$ in equations (24) and (25) can usually be replaced by signs $\leq$. Thus, it is possible to introduce quantities, $\sigma_1, \sigma_2, \ldots$, of the following type,

$$\sigma_1 = r_F \left| \frac{\nabla_\perp v}{v} \right|, \qquad \sigma_2 = \left| \frac{\delta V_F}{V_F} \right|, \qquad \text{etc.,} \tag{26}$$

and

$$\sigma = \text{Max}\,(\sigma_1, \sigma_2, \ldots). \tag{27}$$

The quantity σ can then be used as a *heuristic quantitative estimate of the inaccuracy of the ray method*. The boundary between the region of applicability of the ray method and the region of its inapplicability can be constructed along points at which $\sigma = 1$. For a more detailed discussion of equation (27) see Kravtsov and Orlov (1980).

Thus, the Fresnel volume ray tracing is an efficient tool to find the regions of inapplicability of the ray method. The Fresnel volume ray tracing, however, can offer even more: to find some robust estimates of the wavefield in certain regions of inapplicability of the ray field. Such possibilities were demonstrated by Kravtsov and Orlov (1980) on a caustic singular region. Perhaps it will also be possible to use an alternative approach in the region of inapplicability of the ray method: to combine locally the ray method with some other, more sophisticated approach. We believe that the hybrid combination of various methods is very promising.

Another possible application of the Fresnel volume ray tracing has a different character. The basic property of the Fresnel volumes consist in the fact that they define the region in space that is responsible for the properties of the

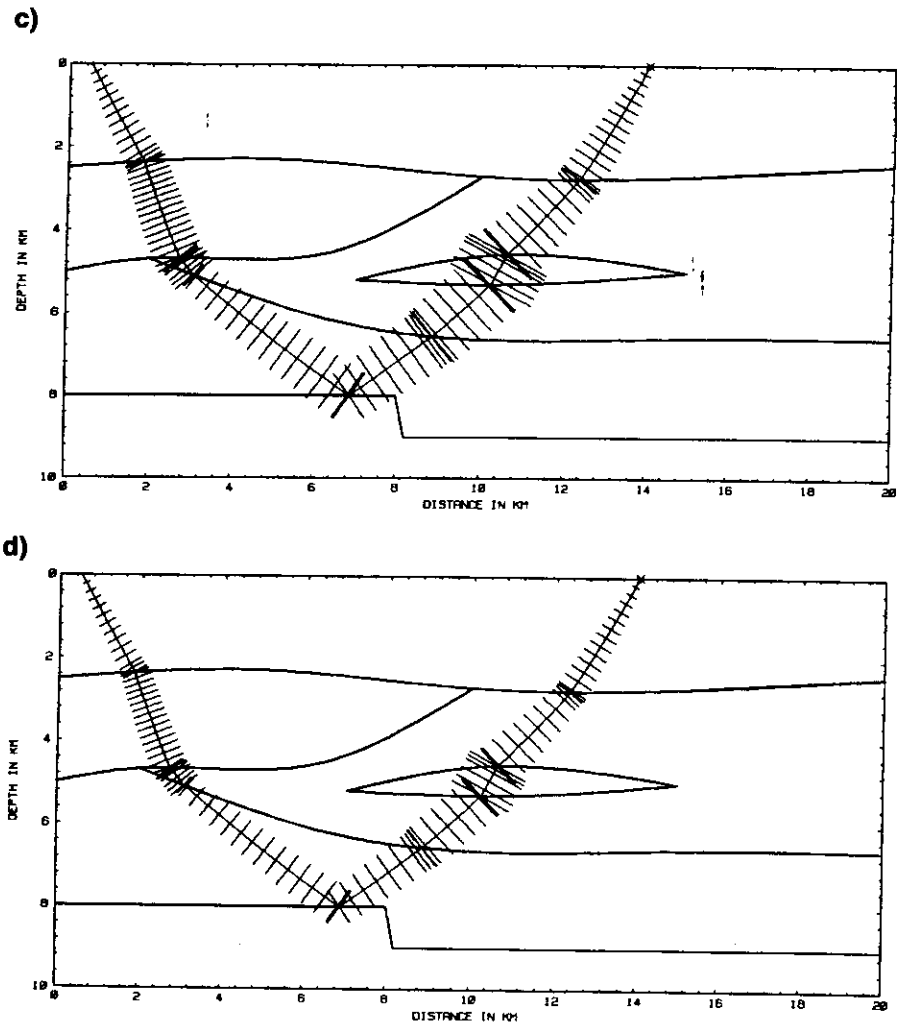

FIG. 11. Continued

wave propagating along the ray under consideration and recorded at a specified point. This property may play an important role in both the numerical modeling of seismic wavefields and in the inversion of seismic data.

ACKNOWLEDGMENTS

This work was carried out during the stay of the authors at the Federal University of Bahia, Salvador. We wish to thank Peter Hubral, Luděk Klimeš, Ivan Pšenčík, and Ru-Shan Wu for valuable comments and discussion. The research was sponsored by CNPq, FINEP, PETROBRAS and by the IBM Academic Initiative in Czechoslovakia.

REFERENCES

Aki, K., and Richards, P. G., 1980, Quantitative seismology: Theory and methods: W. H. Freeman & Co.

Asatryan, A. A., and Kravtsov, Yu. A., 1988, Fresnel zone of hyperbolic type from the physical point of view: Wave Motion, **10**, 45–57.

Babich, V. M., and Buldyrev, N. J., 1972, Asymptotic methods in problems of diffraction of short waves: Nauka, Moscow (in Russian).

Ben-Menahem, A., and Beydoun, W. B., 1985, Range of validity of seismic ray and beam methods in general inhomogeneous media, Part I: General theory: Geophys. J. Roy. Astr. Soc., **82**, 207–234.

Bertoni, H. C., Felsen, L. B., and Hessel, A., 1971, Local properties of radiation in lossy media: IEEE Trans., **Ap-19**, 226–238.

Beydoun, W. B., and Ben-Menahem, A., 1985, Range of validity of seismic ray and beam methods in general inhomogeneous media, Part II: A canonical problem: Geophys. J. Roy. Astr. Soc., **82**, 235–262.

Beydoun, W. B., and Keho, T. H., 1987, The paraxial ray method: Geophysics, **52**, 1639–1653.

Born, M., and Wolf, E., 1980, Principles of optics: Pergamon Press, Inc.

Červený, V., 1985, The application of ray tracing to the propagation of shear waves in complex media, *in* Dohr, G. P., Ed., Seismic shear waves, Part A: Theory; *in* Helbig, K., and Treitel, S., Eds., Handbook of geophysical exploration, Section I: Seismic exploration, **15A**: Geophysical Press.

——— 1987, Ray methods for three-dimensional seismic modeling, Lecture Notes: The University of Trondheim.

——— 1989a, Synthetic body wave seismograms for laterally varying media containing thin transition layers; Geophys. J. Int., **99**, 331–349.

——— 1989b, Seismic ray theory, *in* James, D. E., Ed., Encyclopedia of geophysics: D. Van Nostrand Co.

Červený, V., Klimeš, L., and Pšenčík, I., 1984, Paraxial ray approximation in the computation of seismic wavefields in inhomogeneous media: Geophys. J. Roy. Astr. Soc., **79**, 89–104.

——— 1988, Complete seismic ray tracing in three-dimensional structures, *in* Doornbos, D. J., Ed., Seismological Algorithms: Academic Press Inc.

Červený, V., Molotkov, I. A., and Pšenčík, I., 1977, Ray method in seismology: Univ. Karlova.

Červený, V., and Pšenčík, I., 1983, Gaussian beam and paraxial ray approximation in three-dimensional inhomogeneous media: Bull. Seis. Soc. Am., **70**, 47–77.

——— 1984, SEIS83-Numerical modeling of seismic wavefields in 2-D laterally varying layered structures by the ray method, *in* Engdahl, E. R., Ed., Documentation of earthquake algorithms, Report SE-35: World Data Center A for Solid Earth Geophysics, Boulder, CO.

Chapman, C. H., 1985, Ray theory and its extensions: WKBJ and Maslov seismograms: J. Geophys., **58**, 27–43.

Eaton, D. W. S., Stewart, R. R., and Harrison, M. P., 1991, The Fresnel zone for *P-SV* waves: Geophysics, **56**, 360–364.

Flatté, S. M., Dashen, R., Munk, W. H., Watson, K. M., and Zachariasen, F., 1979, Sound transmission through a fluctuating ocean: Cambridge Univ. Press.

Gelchinsky, B. Ya., 1985, The formulae for the calculation of the Fresnel zones or volumes: J. Geophys., **57**, 33–41.

Hagedoorn, T. G., 1959, A process of seismic reflection interpretation: Geophys. Prosp., **2**, 85–127.

Hilterman, F. T., 1970, Three-dimensional seismic modeling: Geophysics, **35**, 1020–1037.

Hubral, P., 1980, Wavefront curvatures in three-dimensional laterally inhomogeneous media with curved interfaces: Geophysics, **45**, 905–913.

Hubral, P., and Krey, T. H., 1980, Interval velocities from seismic reflection time measurements: Soc. Explo. Geophys.

Klem-Musatov, K. D., 1980, Theory of edge waves and its applications in seismic methods: Nauka, Siberian Branch, Novosibirsk (in Russian).

Kleyn, A. H., 1983, Seismic reflection interpretation, Applied Science Publ. Ltd.

Knapp, R. W., 1991, Fresnel zones in the light of broadband data: Geophysics, **56**, 354–359.

Kravtsov, Yu. A., and Orlov, Yu. I., 1979, On the validity conditions of the geometrical optics method, in Recent problems of propagation and scattering of waves: IRE Acad. Sci. USSR, Moscow (in Russian).

——— 1980, Geometrical optics of inhomogeneous media: Nauka, Moscow (in Russian).

Lindsey, J. P., 1989, The Fresnel zone and its interpretative significance: The Leading Edge, **8**, no. 10, 33–39.

Pant, D. R., and Greenhalgh, S. A., 1989, Lateral resolution in seismic reflection. A physical model study: Geophys. J., **97**, 187–198.

Sheriff, R. E., 1977, Limitations on resolution of seismic reflections and geological details derivable from them, *in* Payton, C. E., Ed., Seismic stratigraphy—Applications to hydrocarbon explorations: Mem. Am. Assn. Petr. Geol., **26**, 3–14.

——— 1980, Nomogram for Fresnel zone calculation: Geophysics, **45**, 968–972.

——— 1985, Aspects of seismic resolution, *in* Berg, O. R., and Woolverton, D. G., Eds., Seismic stratigraphy, II: An integrated approach to hydrocarbon exploration: Mem. Assn. Petr. Geol., **39**, 4–27.

——— 1989, Geophysical methods: Prentice-Hall, Inc.

Sheriff, R. E., and Geldart, L. P., 1982, Exploration seismology, vol. I: Cambridge Univ. Press.

Woodward, M. J., 1989, Bandlimited raypaths: An example: Stanford Explo. Proj. No. 60.

Wu, R. S., and Aki, K., 1988, Introduction: Seismic wave scattering in three-dimensionally heterogeneous Earth: PAGEOPH, **128**, 1–6.

PART 3

DIRECT COMPUTATION OF FIRST ARRIVAL TRAVEL TIMES. NETWORK RAY TRACING

The 3-D model is used in a discretized form: the velocities are specified in a rectangular grid of points.

Two basic methods have been proposed to compute the travel times of first arrivals in 3-D models:

a) Finite difference wavefront tracing techniques by Vidale (1988, 1990), Podvin and Lecomte (1991), etc.

b) Network shortest path ray tracing, see Nakanishi and Yamaguchi (1986), Saito (1989, 1990), Moser (1989, 1991).

The paper by Moser, Geophysics 56 (1991), 59-67, gives details of the network shortest path ray tracing, and a rich literature devoted to both methods. No additional notes related to this problem are included here.

PART 4

EXTENSIONS AND MODIFICATIONS OF THE SEISMIC RAY METHOD. HYBRID COMBINATIONS WITH OTHER METHODS

For various extensions of the ray method see the references shown in Part 1.

Two hybrid combinations of the ray method with some other methods are described here in a greater detail:

a) the hybrid combination of the ray method with the Born approximation. See Červený and Coppoli (1992).

b) The hybrid combination of the ray method with the reflectivity method. See Červený (1989), Červený and Andrade (1992), Červený and Aranha (1992).

Other suitable references can be found in these papers.

RAY-BORN SYNTHETIC SEISMOGRAMS FOR COMPLEX STRUCTURES CONTAINING SCATTERERS

VLASTISLAV ČERVENÝ [1,2] and ANASTASIA COPPOLI D.M. [2]

[1] *Institute of Geophysics, Charles University, Ke Karlovu 3, 121 16 Praha 2, Czechoslovakia.*
[2] *Instituto de Geociências, Universidade Federal da Bahia, Rua Caetano Moura 123, Federação, 40.210 Salvador, Bahia, Brasil.*

(Received November 29, 1991; revised version accepted January 3, 1992)

ABSTRACT

Červený, V. and Coppoli D.M., A., 1992. Ray-Born synthetic seismograms for complex structures containing scatterers. *Journal of Seismic Exploration*, 1: 191-206.

The hybrid method based on a combination of the ray theory with the Born approximation can be used to compute synthetic seismograms in complex, laterally varying layered structures containing small scatterers. The scatterers can be combined to form objects of a complex shape. The wave field in the background, laterally varying layered structure is computed by the ray method and the single scattered wave field by the Born approximation. A computer program package designed for such hybrid ray-Born computations in 2-D models is briefly described and numerical applications are presented. The ray-Born numerical modelling of seismic wave fields extends the possibilities of ray modelling considerably.

KEY WORDS: ray method, Born approximation, hybrid ray-Born method, scattering of seismic waves.

INTRODUCTION

The ray method has found many successful applications in seismic prospecting for oil and in seismology. It is very general and can be used to study the propagation of high-frequency seismic (or acoustic) waves in complex, laterally varying layered structures. Even though the accuracy of the ray method is only limited, it is the only method that is able to give an approximate answer to many wave propagation problems in 2-D and 3-D complex structures of a great practical importance.

0963-0651/92/$5.00

The ray method, however, can be applied only to wave fields in media with smooth variations of elastic parameters and density. The model may contain interfaces, but these interfaces must be also smooth. In regions of high velocity gradient, the ray method is not applicable. Similarly,the ray method is not directly applicable to study the interaction of the wave field with scatterers, the size of which is less than or comparable with the wavelength.

The scattered wave field generated by such scatterers can, however, be studied by other methods. If the velocities and the density within the scatterers do not differ considerably from the velocities and the densities in the surrounding media, the perturbation methods can be used, for example the Born or the Rytov appoximation.

Here we discuss the hybrid method based on a combination of the ray method and the Born approximation. We consider a general smooth, laterally varying layered structure, in which the ray method can be used. This structure is considered as a background medium. In addition, the structure contains a limited number of scatterers. The single scattered wavefield is then evaluated by the Born integrals.

In this contribution, we briefly describe both the ray and the Born computations for a general 3-D background model containing scatterers. For simplicity, we consider here only acoustic media; the generalization for elastic media is straightforward. We also briefly describe the computer program package used for the ray-Born numerical modelling of acoustic wavefields in complex 2-D stuctures, and present examples of computations.

ACOUSTIC RAY THEORY GREEN FUNCTION

The pressure wave field $p(\mathbf{x},t)$ satisfies in inhomogeneous medium the acoustic wave equation

$$\nabla\cdot(\sigma\nabla p) - \varkappa\ddot{p} = -\dot{q}(\mathbf{x},t), \tag{1}$$

where t is time, $\mathbf{x} \equiv (x_1, x_2, x_3)$ are Cartesian coordinates, $\varkappa(\mathbf{x})$ the compressibility, $\sigma(\mathbf{x})$ the specific volume and $q(\mathbf{x},t)$ the volume injection rate density. The dots above the letters denote partial derivatives with respect to time. Instead of σ and $\varkappa$, we can also use the density $\varrho(\mathbf{x})$ and the propagation velocity $c(\mathbf{x})$ using the following relations: $\sigma = 1/\varrho$, $\varkappa = 1/\varrho c^2$. We define the acoustic Green function $G(\mathbf{x},t\,;\mathbf{x}_0,t_0)$ as a solution of (1) at a point x and time t corresponding to the source function $\dot{q}(\mathbf{x},t)$ given by the relation

$$\dot{q}(\mathbf{x},t) = \delta(t - t_0)\,\delta(\mathbf{x} - \mathbf{x}_0). \tag{2}$$

Thus, the acoustic Green function satisfies the equation

$$\nabla\cdot(\sigma\nabla G) - \varkappa\ddot{G} = -\delta(t - t_0)\,\delta(\mathbf{x} - \mathbf{x}_0). \tag{3}$$

The Green function can be calculated by ray methods for very general 3-D laterally varying layered structures. At interfaces, proper interface conditions must be taken into account (continuity of the pressure and of the normal component of the particle velocity). Then the ray theory acoustic Green function is described by the following equation

$$G(\mathbf{x},t\,;\mathbf{x}_0,t_0) = \sum_{(\Omega)} G^{\Omega}(\mathbf{x},t\,;\mathbf{x}_0,t_0), \tag{4}$$

where the summation runs over all rays Ω connecting x and $\mathbf{x}_0$, corresponding to direct, reflected, multiply reflected, and other types of waves. The number of rays connecting x and $\mathbf{x}_0$ may be finite or infinite. If the number is infinite, the series (4) must be truncated. The Green function $G^{\Omega}(\mathbf{x},t\,;\mathbf{x}_0,t_0)$, corresponding to a selected ray Ω, will be called here the elementary Green function. It is given by the following equation

$$G^{\Omega}(\mathbf{x},t\,;\mathbf{x}_0,t_0) = \mathrm{Re}[A^{\Omega}(\mathbf{x},\mathbf{x}_0)\delta^{(A)}\{t - t_0 - T^{\Omega}(\mathbf{x},\mathbf{x}_0)\}]. \tag{5}$$

Here $\delta^{(A)}(\xi)$ is an analytic delta function and $T^{\Omega}(\mathbf{x},\mathbf{x}_0)$ is the travel time from $\mathbf{x}_0$ to x along the ray Ω. The analytic delta function is given by the well-known relation $\delta^{(A)}(\xi) = \delta(\xi) - i/(\pi\xi)$, where $\delta(\xi)$ is a standard real-valued delta function. The travel time $T^{\Omega}(\mathbf{x},\mathbf{x}_0)$ can be calculated by ray tracing. The complex-valued amplitude factor $A^{\Omega}(\mathbf{x},\mathbf{x}_0)$ is given by the relation

$$A^{\Omega}(\mathbf{x},\mathbf{x}_0) = [\varrho(\mathbf{x})\varrho(\mathbf{x}_0)c(\mathbf{x})c(\mathbf{x}_0)]^{1/2}\,\mathrm{Re}^{\,i\,\delta T(\mathbf{x},\mathbf{x}_0)} / 4\pi J(\mathbf{x},\mathbf{x}_0). \tag{6}$$

Here the function $J(\mathbf{x},\mathbf{x}_0)$ is the relative geometrical spreading. It can be calculated by dynamic ray tracing along the ray Ω, performed in the ray-centred coordinates. By the solution of the dynamic ray-tracing system along Ω from

$\mathbf{x}_0$ to $\mathbf{x}$, we can determine the 4×4 ray propagator matrix $\mathbf{\Pi}(\mathbf{x}, \mathbf{x}_0)$ which satisfies at $\mathbf{x} = \mathbf{x}_0$ the initial conditions $\mathbf{\Pi}(\mathbf{x}_0, \mathbf{x}_0) = \mathbf{I}$, where $\mathbf{I}$ is a 4×4 identity matrix. We introduce four 2×2 matrices $\mathbf{P}_1(\mathbf{x}, \mathbf{x}_0)$, $\mathbf{Q}_1(\mathbf{x}, \mathbf{x}_0)$, $\mathbf{P}_2(\mathbf{x}, \mathbf{x}_0)$ and $\mathbf{Q}_2(\mathbf{x}, \mathbf{x}_0)$ by the following equation

$$\mathbf{\Pi}(\mathbf{x}, \mathbf{x}_0) = \begin{bmatrix} \mathbf{Q}_1(\mathbf{x}, \mathbf{x}_0) & \mathbf{Q}_2(\mathbf{x}, \mathbf{x}_0) \\ \mathbf{P}_1(\mathbf{x}, \mathbf{x}_0) & \mathbf{P}_2(\mathbf{x}, \mathbf{x}_0) \end{bmatrix}. \tag{7}$$

Then the relative geometrical spreading $J(\mathbf{x}, \mathbf{x}_0)$ is given by the relation

$$J(\mathbf{x}, \mathbf{x}_0) = |\det \mathbf{Q}_2(\mathbf{x}, \mathbf{x}_0)|. \tag{8}$$

It is possible to show that the relative geometrical spreading $J(\mathbf{x}, \mathbf{x}_0)$ is reciprocal,

$$J(\mathbf{x}, \mathbf{x}_0) = J(\mathbf{x}_0, \mathbf{x}), \tag{9}$$

and that it does not depend on the parametrisation of the ray field. The function $\delta T(\mathbf{x}, \mathbf{x}_0)$ in (6) is the phase shift due to caustics and can be also calculated by dynamic ray tracing. In a homogeneous medium, $J(\mathbf{x}, \mathbf{x}_0)$ and $\delta T(\mathbf{x}, \mathbf{x}_0)$ can be determined analytically, $J(\mathbf{x}, \mathbf{x}_0) = c^2 |\mathbf{x} - \mathbf{x}_0|^2$ and $\delta T(\mathbf{x}, \mathbf{x}_0) = 0$. For a 2-D case, the matrix $\mathbf{Q}_2(\mathbf{x}, \mathbf{x}_0)$ has a diagonal form and the relative geometrical spreading can be expressed as follows:

$$J(\mathbf{x}, \mathbf{x}_0) = |Q_2''(\mathbf{x}, \mathbf{x}_0)|\, \sigma(\mathbf{x}, \mathbf{x}_0), \tag{10}$$

where $\sigma(\mathbf{x}, \mathbf{x}_0)$ is given by the relation,

$$\sigma(\mathbf{x}, \mathbf{x}_0) = \int_{\mathbf{x}_0}^{\mathbf{x}} c\, ds. \tag{11}$$

The integral in (11) is taken along the ray Ω. The function $|Q_2''(\mathbf{x}, \mathbf{x}_0)|$ is the relative geometrical spreading in a plane of the ray Ω and can be evaluated by a 2-D dynamic ray tracing, consisting of 2 equations only.

For a ray Ω crossing N interfaces at points Q_i, $i = 1,2,\ldots,N$, the ray propagator matrix should be multiplied by a 4×4 interface matrix $\mathbf{F}(Q_i)$ at any point Q_i, to satisfy the boundary conditions. The final expressions for the ray propagator matrix is then as follows,

$$\mathbf{\Pi}(\mathbf{x}, \mathbf{x}_0) = \mathbf{\Pi}(Q_{N+1}, Q_N) \prod_{i=N}^{1} [\mathbf{F}(Q_i)\, \mathbf{\Pi}(Q_i, Q_{i-1})], \tag{12}$$

where the point Q_0 corresponds to $\mathbf{x}_0$ and the point Q_{N+1} to $\mathbf{x}$. For more details on dynamic ray tracing and derivation of all above presented equations see Červený (1987, 1989a).

Finally, the symbol R in (6) denotes the complete reflection/transmission coefficient. It is given by the relation,

$$R = \prod_{i=1}^{N} R(Q_i), \tag{13}$$

where the product corresponds to points Q_1, Q_2, ..., Q_N of reflection/transmission along the ray. The reflection/transmission coefficients can be expressed by the following relations:

$$R_{refl.} = (\varrho_2 c_2 \cos i_1 - \varrho_1 c_1 \cos i_2) / (\varrho_2 c_2 \cos i_1 + \varrho_1 c_1 \cos i_2),$$

$$R_{transm.} = (\varrho_1 \varrho_2 c_1 c_2 \cos i_1 \cos i_2)^{1/2} / (\varrho_2 c_2 \cos i_1 + \varrho_1 c_1 \cos i_2). \tag{14}$$

Here c_1 and ϱ_1 are the velocity and density at the point of incidence Q_i, on the side of the incident wave, c_2, ϱ_2 have the same meaning, but on the opposite side of the interface, i_1 is the angle of incidence, i_2 is the angle of transmission. Note that both $R_{refl.}$ and $R_{transm.}$ are reciprocal, so that the complete reflection/transmission coefficient R given by (13) is reciprocal. Note also a non-traditional form of the reciprocal transmission coefficient in (14).

In the frequency domain, the acoustic Green function $G(\mathbf{x}, \mathbf{x}_0, \omega)$ is a solution of the acoustic wave equation

$$\nabla\cdot(\sigma\nabla G) + \omega^2 \varkappa G = -\delta(\mathbf{x} - \mathbf{x}_0). \tag{15}$$

The ray theory Green function $G(\mathbf{x}, \mathbf{x}_0, \omega)$ is again given by the summation (4) over all rays Ω, where the elementary Green functions $G^{\Omega}(\mathbf{x}, \mathbf{x}_0, \omega)$ are given by the equation

$$G^{\Omega}(\mathbf{x}, \mathbf{x}_0, \omega) = A^{\Omega}(\mathbf{x}, \mathbf{x}_0)\, e^{i\omega T^{\Omega}(\mathbf{x}, \mathbf{x}_0)}. \tag{16}$$

It should be emphasized that the acoustic ray theory Green function is spatially reciprocal, both in the time domain, see (5), and in the frequency domain, see (16);

$$G(\mathbf{x},t\,;\mathbf{x}_0,t_0) = G(\mathbf{x}_0,t\,;\mathbf{x},t_0)\,,$$

$$G(\mathbf{x}, \mathbf{x}_0, \omega) = G(\mathbf{x}_0, \mathbf{x}, \omega).$$

BORN APPROXIMATION

Let us consider a model in which the specific volume $\sigma(\mathbf{x})$ and the compressibility $\varkappa(\mathbf{x})$ are given by the equations

$$\sigma(\mathbf{x}) = \sigma_0(\mathbf{x}) + \sigma'(\mathbf{x})\,,$$

$$\varkappa(\mathbf{x}) = \varkappa_0(\mathbf{x}) + \varkappa'(\mathbf{x}). \tag{17}$$

Here $\sigma_0(\mathbf{x})$ and $\varkappa_0(\mathbf{x})$ correspond to the background model, and $\sigma'(\mathbf{x})$, $\varkappa'(\mathbf{x})$ are small perturbations. When a wave is incident on a region of non-vanishing $\sigma'(\mathbf{x})$, $\varkappa'(\mathbf{x})$, a scattered wavefield is generated.

Let us assume that a point source (2) is situated at a point $\mathbf{x} = \mathbf{x}_s$, and the receiver at $\mathbf{x} = \mathbf{x}_r$. Then the Born integral representation of the single scattered acoustic wave field $B(\mathbf{x}_r, \mathbf{x}_s, \omega)$ in the frequency domain is as follows:

$$B(\mathbf{x}_r, \mathbf{x}_s, \omega) = \iiint \{\omega^2 \varkappa'(\mathbf{x})\, G(\mathbf{x}_r, \mathbf{x}, \omega)\, G(\mathbf{x}, \mathbf{x}_s, \omega) - \sigma'(\mathbf{x})\, \nabla G(\mathbf{x}_r, \mathbf{x}, \omega)\, \nabla G(\mathbf{x}, \mathbf{x}_s, \omega)\}\, d\mathbf{x}. \tag{18}$$

The integration is over the whole space V in which $\sigma'(\mathbf{x})$ and $\varkappa'(\mathbf{x})$ are non-vanishing. The symbol G denotes the Green function in the background medium. In the following, we shall consider an asymptotic high-frequency expression for $B(\mathbf{x}_r, \mathbf{x}_s, \omega)$. In other words, in (18) we can use the ray expressions for the Green functions, see (4) and (16). For simplicity, we shall not write the summation (4) and the superscript Ω in the expressions for the Green function, its amplitude and relevant travel time. We will tacitly understand that the summation should be performed over all rays connecting $\mathbf{x}_s$ with $\mathbf{x}$ and $\mathbf{x}_r$ with $\mathbf{x}$. Our expressions will correspond to one, but arbitrary, selection of rays from $\mathbf{x}_s$ to $\mathbf{x}$ and from $\mathbf{x}_r$ to $\mathbf{x}$. Using (16), we can easily obtain an approximate high-frequency equation,

$$\nabla G(\mathbf{x}_r, \mathbf{x}, \omega) = i\omega\, A(\mathbf{x}_r, \mathbf{x})\, \nabla T(\mathbf{x}_r, \mathbf{x})\, e^{i\omega T(\mathbf{x}_r, \mathbf{x})}\,,$$

and similarly for $\nabla G(\mathbf{x}_s, \mathbf{x}, \omega)$. This yields

$$B(\mathbf{x}_r, \mathbf{x}_s, \omega) = \omega^2 \iiint \{\varkappa'(\mathbf{x}) + \sigma'(\mathbf{x}) \times c_0^{-2}(\mathbf{x}\ \cos\theta(\mathbf{x}_r, \mathbf{x}_s, \mathbf{x})\} \times a(\mathbf{x}_r, \mathbf{x}_s, \mathbf{x})\, e^{i\omega T(\mathbf{x}_r, \mathbf{x}_s, \mathbf{x})}\, d\mathbf{x}, \tag{19}$$

where

$$a(\mathbf{x}_r, \mathbf{x}_s, \mathbf{x}) = A(\mathbf{x}_s, \mathbf{x})\, A(\mathbf{x}_r, \mathbf{x})\,,$$

$$T(\mathbf{x}_r, \mathbf{x}_s, \mathbf{x}) = T(\mathbf{x}_s, \mathbf{x}) + T(\mathbf{x}_r, \mathbf{x})\,,$$

$$\cos\theta(\mathbf{x}_r, \mathbf{x}_s, \mathbf{x}) = c_0^2(\mathbf{x})\, \nabla T(\mathbf{x}_s, \mathbf{x})\, \nabla T(\mathbf{x}_r, \mathbf{x}). \tag{20}$$

All the quantities a, T and $\cos\theta$ are reciprocal. Let us emphasize that the expressions for the amplitudes A and travel times T in (20) can be calculated by ray tracing in the background medium, even inside the volume V.

Several alternative forms of (19) are possible. It is not difficult to show that the perturbation factor in (19) can be written as follows:

$$\varkappa'(\mathbf{x}) + [\sigma'(\mathbf{x})/c_0^2(\mathbf{x})] \cos\theta = -4\cos^2(\theta/2) R(\mathbf{x}_r, \mathbf{x}_s, \mathbf{x})/c_0(\mathbf{x})\, Z_0(\mathbf{x}), \tag{21}$$

where

$$R(\mathbf{x}_r, \mathbf{x}_s, \mathbf{x}) = \tfrac{1}{2}\,\delta Z + \tfrac{1}{2}\,\delta c \tan^2(\theta/2). \qquad (22)$$

Here $Z = \varrho c$ is the acoustic impedance, $\delta Z = (Z - Z_0)/Z_0$, $\delta c = (c - c_0)/c_0$; the subscript "0" corresponds to the background medium. The function R corresponds to a linearized form of the reflection coefficient $R_{refl.}$ from (14). Inserting (21) into (19) yields:

$$B(\mathbf{x}_r, \mathbf{x}_s, \omega) = -4\omega^2 \iiint R \cos^2(\theta/2)[c_0(\mathbf{x})\, Z_0(\mathbf{x})]^{-1} \times a(\mathbf{x}_r, \mathbf{x}_s, \mathbf{x})\, e^{i\omega\, T(\mathbf{x}_r, \mathbf{x}_s, \mathbf{x})}\, d\mathbf{x}. \qquad (23)$$

The equations (19) and (23) are final expressions for the 3-D Born integral.

In a 2-D case, Born integrals can be simplified. Let us assume that both the background model and the perturbations do not depend on x_2. In other words, the scatterers are infinitely prolongated along the x_2 axis. We also consider the source $\mathbf{x}_s$ and the receiver $\mathbf{x}_r$ situated in the plane $x_2 = 0$, so that $x_{s2} = x_{r2} = 0$. We do not consider a line source, but a point source at $\mathbf{x}_s$; such a configuration is often called a 2.5 dimensional case. Then the integral over x_2 in (19) and (23) can be calculated for high-frequency ω by the method of stationary phase to give

$$B(\mathbf{x}_r, \mathbf{x}_s, \omega) = (2\pi)^{1/2} \omega^{3/2} e^{i\pi/4} \iint \{\varkappa'(\mathbf{x}) + \sigma'(\mathbf{x})\, c_0^{-2}(\mathbf{x}) \cos\theta\} \times a(\mathbf{x}_r, \mathbf{x}_s, \mathbf{x})\, Y(\mathbf{x}_r, \mathbf{x}_s, \mathbf{x})\, e^{i\omega\, T(\mathbf{x}_r, \mathbf{x}_s, \mathbf{x})}\, dx_1\, dx_3, \qquad (24)$$

or, alternatively,

$$B(\mathbf{x}_r, \mathbf{x}_s, \omega) = -4\,(2\pi)^{1/2} \omega^{3/2} e^{i\pi/4} \iint R \cos^2(\theta/2)[c_0(\mathbf{x})\, Z_0(\mathbf{x})]^{-1} \times a(\mathbf{x}_r, \mathbf{x}_s, \mathbf{x})\, Y(\mathbf{x}_r, \mathbf{x}_s, \mathbf{x})\, e^{i\omega\, T(\mathbf{x}_r, \mathbf{x}_s, \mathbf{x})}\, dx_1\, dx_3, \qquad (25)$$

Here the function $Y(\mathbf{x}_r, \mathbf{x}_s, \mathbf{x})$ is given by the relation

$$Y(\mathbf{x}_r, \mathbf{x}_s, \mathbf{x}) = [\,1/\sigma(\mathbf{x}_s, \mathbf{x}) + 1/\sigma(\mathbf{x}_r, \mathbf{x})\,]^{1/2}, \qquad (26)$$

σ is given by (11). The integration is over the volume V' which represents a part of the plane $x_1 x_3$ in which δZ and δc are nonvanishing.

For more details on the Born approximation, including the elastodynamic case, see Beydoun and Mendes (1989), Beylkin and Burridge (1990), Coates and Chapman (1990), Wu (1989a,b). These papers also present extensive literature related to this subject.

HYBRID RAY-BORN MODELLING

The hybrid ray-Born modelling can be used to compute synthetic seismograms for laterally varying layered structures, containing scatterers of the size smaller than a prevailing wavelength. The scatterers can be, of course, combined to form bodies of a complex shape. To compute the wavefield corresponding to the background laterally varying layered structure, the ray method is used, and relevant synthetic seismograms are generated. To evaluate the single scattered wave field, eqs. (19) or (23) can be used for 3-D, and eqs. (24) or (25) for 2-D.

The program package BEAM87, see Červený (1989b), is modified to perform such hybrid ray-Born computations in two-dimensional laterally varying layered structures.

The wave field, generated by a point source situated at any point of the model, is computed by the ray method as a superposition of individual elementary waves. The elementary waves may be selected by the user (direct, reflected, transmitted, multiply reflected/transmitted). Zero-order approximation of the ray method is used in the computation.

The scatterers may be also situated at arbitrary positions. The elementary wave incident on the scatterer and generating the single scattered field may be again selected arbitrarily, similarly as the rays along which the scattered waves propagate from the scatterer to the receiver. The single scattered wave field is calculated by Born integrals.

NUMERICAL EXAMPLES

In the numerical examples, we shall consider a simple laterally varying 2-D background model with two curved interfaces (see Fig. 1). The velocity c in all layers is increasing downwards, and also laterally from the left to the right. The average velocities in the first layer are close to 3 km/s, in the second layer close to 4 km/s, and in the last layer close to 5 km/s. For example, in the first layer, the velocity changes from 2.7 km/s in the top left-hand corner of the

layer to 3.6 km/s in the bottom right-hand corner of the layer. The density is constant in the whole model, and the absorption is not considered.

In the model, the x_1-axis of the Cartesian coordinate system is taken along the upper boundary of the model, which is pressumably planar, and is situated inside the medium. (The effects of the surface are not taken into account). The x_3-axis of the Cartesian coordinate system is oriented downwards, the coordinate x_3 corresponds to depth. The receivers are distributed along the upper boundary of the model. The point source is situated at $x_1 = 2$ km, $x_3 = 0$ km. The source time function corresponds to the Gabor signal

$$x(t) = \exp [- (2 \pi f_M t/\gamma)^2] \cos (2 \pi f_M t + \upsilon),$$

with $\gamma = 4$, $f_M = 30$ Hz, $\upsilon = 0$. The scatterers are situated in different parts of the model in individual presented examples.

The ray-Born method has been used to evaluate the wave field at individual receivers. The standard ray method has been applied in the calculation of the waves reflected from both interfaces in the background model, and the scattered wave field from the scatterers was evaluated by the Born approximation.

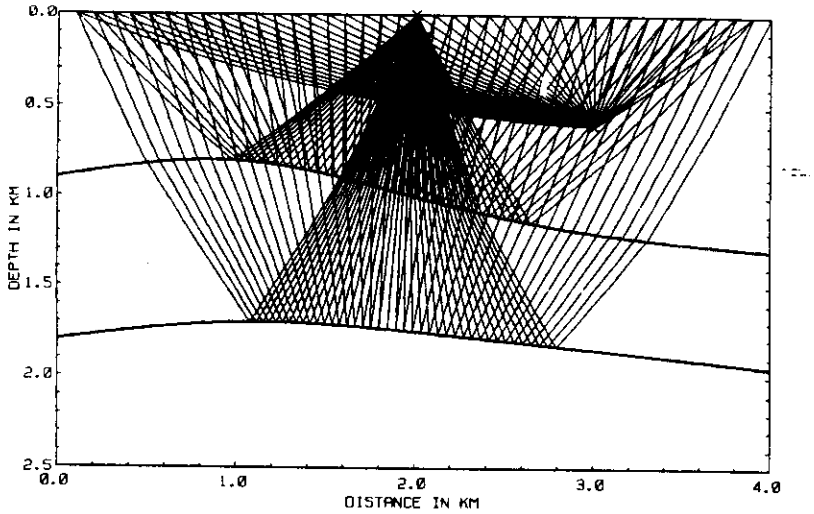

Fig. 1. A 2-D laterally varying structure with two curved interfaces and one single scatterer. A point source is situated in the middle of the upper boundary of the model. Ray diagrams of waves refleeted from both interfaces and of the scattered wave are shown.

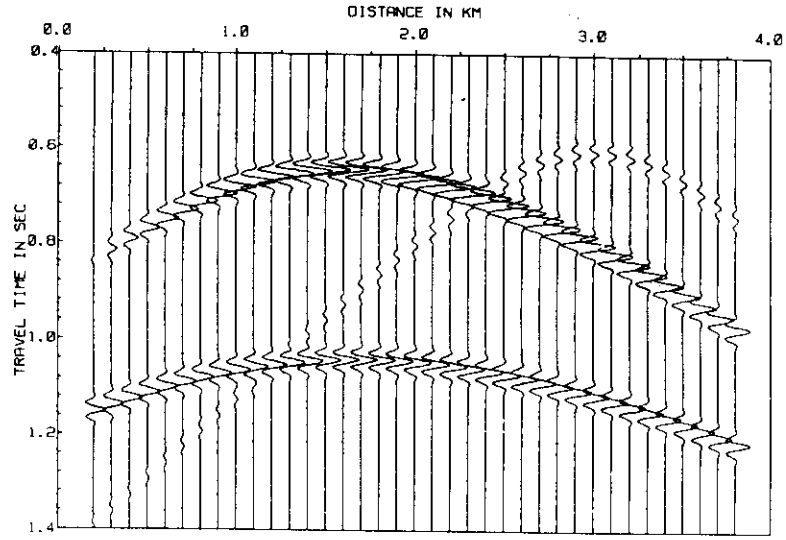

Fig. 2a. Ray-Born synthetic seismograms for the model corresponding to Fig. 1. The size of the scatterer is 25 × 25 m, and the velocity within the scatterer is by 10% higher than in the background model.

In the **first example**, the scatterers are situated close to the point $x_1 = 3$km, $x_3 = 0.6$ km. Fig. 1 shows the ray diagrams of waves reflected from both interfaces, and a ray diagram corresponding to one scatterer of the size $\Delta x_1 = \Delta x_3 = 25$ m, situated at $x_1 = 3.0$ km, $x_3 = 0.6$ km. The scatterer is, of course, infinitely prolongated along the x_2 axis. The velocity c within the scatterer (in the perturbed model) differs by 10% from the velocity in the background medium. The ray-Born synthetic seismograms for the model with the above described scatterer are shown in Fig. 2a. All the synthetic seismograms are normalized with respect to the maximum amplitude in the whole section. The scattered wave field has a simple hyperbolic appearence. A very interesting behaviour of the scattered wave field is a slow decrease of amplitudes along very long tails of the diffraction hyperbola. Fig. 2b shows the ray-Born synthetic seismograms corresponding to a thin plate scatterer situated roughly at the same place as the individual scatterer considered in Figs. 1 and 2a. The thickness of the plate is 25 m, and its length 275 m. Note that the wavelength in this part of the model is close to 110 m. The scatterer is again infinitely prolongated along the x_2 axis. The plate makes approximately an angle

of 45° with the x_1 and x_3 axes. From a numerical point of view, the plate scatterer is approximated by eleven individual scatterers. The velocity inside the scatterer is the same as in the individual scatterer in Fig. 2a. It is interesting to observe that the scattered wave field corresponding to a thin plate is of a different character than the scattered wave field corresponding to a single scatterer. The tails corresponding to individual scatterers forming the plate scatterer are mutually cancelled by a destructive interference. Only two tails are formed, corresponding to its end points. The tail amplitudes are weaker in this case than in Fig. 2a. In between, a regular reflected wavefield from the scattering thin plate is formed, see receivers at x_1 = 2.5 - 3 km. The scattered wave field is very intensive, comparable with the intensity of waves reflected from the two interfaces.

Several similar numerical experiments have been performed with different shapes and orientations of combined scatterers. In general, the amplitudes of the scattered wave field recorded on the surface of the model depend considerably on the orientation of the (plate) scatterer. The scattered wave field is rather strong for horizontal scatterers, but considerably weaker for vertical scatterers.

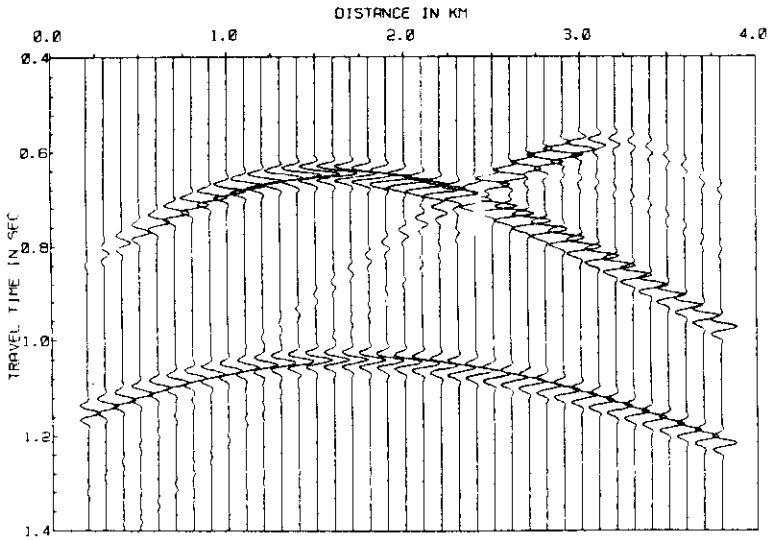

Fig. 2b. Ray-Born synthetic seismograms for the same configuration as in Fig. 2a, only the single scatterer is replaced by a scattering plate of the size 2[illegible] × 25 m, composed of 11 individual scatterers. The plate makes an angle of 45° with the x_1 and x_3 axis.

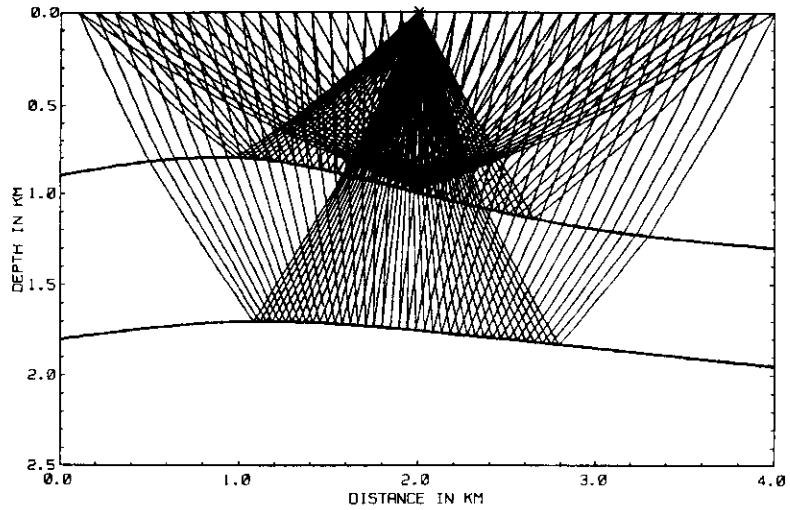

Fig. 3. Ray diagrams for the same structure as in Fig. 1, only the scatterer is situated directly above the first interface, in the first layer.

In the **second example**, the scatterers are situated directly on the upper side of the first interface. For one scatterer of the size $\Delta x_1 = \Delta x_3 = 25$ m, the ray diagram is shown in Fig. 3. In Figs. 4a,b,c, the ray-Born synthetic seismograms are shown, corresponding to different scatterer configurations. The velocity within scatterers corresponds to the velocity below the interface. The synthetic seismograms are again normalized with respect to the maximum amplitude in the whole section. Fig. 4a corresponds to one scatterer, see the ray diagrams on Fig. 3. Fig. 4b simulates a corrugated interface of a length of 325 m, between x_1 = 1.8 km and x_2 = 2.1 km. The scatterers, of a size of 25m, are situated along the interface, also with gaps of 25 m. Finally, Fig. 4c shows a continuous system of scatterers of a length of 325 m, without gaps. Thus the last model represents an elevation of the interface by 25 m in the total length of 325 m, with sharp edges at both sides of the elevation.

The wave field corresponding to a single scatterer in Fig. 4a is simple. The decrease of amplitudes along long tails is again very slow. The wavefields corresponding to the corrugated interface (Fig. 4b) and to the elevated interface

(Fig. 4c) are, of course, mutually very different. The corrugated interface generates strong and long reverberations, see the L.H.S. of Fig. 4b. It also destroys the regular reflected wave field at certain receivers, see e.g., receivers at x_1 = 3.2 - 3.4 km in Fig. 4b. On the other side, the local elevation of the interface does not yield such a strong scattered field (see Fig. 4c). The reverberations are considerably supressed. The local elevation generates only two scattered waves from the edges of the elevation. If we compare the arrival times of reflected waves at x_1 ~ 2.0 - 2.5 km in Figs. 4a and 4c, we can clearly observe the earlier arrivals in Fig. 4c, due to the elevated interface. Close to both edges of the elevation, the reflected wave field is considerably influenced by the edge effects. See the traces at x_1 = 1.6 - 1.9 km and at x_1 = 3.0 - 3.4 km. For other examples of computations, see Coppoli D.M. (1991).

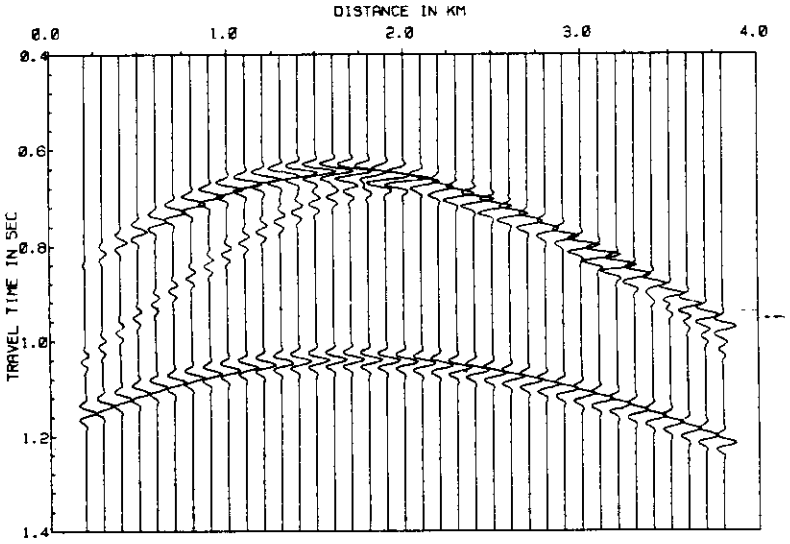

Fig. 4a. Ray-Born synthetic seismograms for the model corresponding to Fig.3. The size of the scatterer is 25 x 25 m. The velocity within the scatterer correspond to the velocity below the interface, in the second layer.

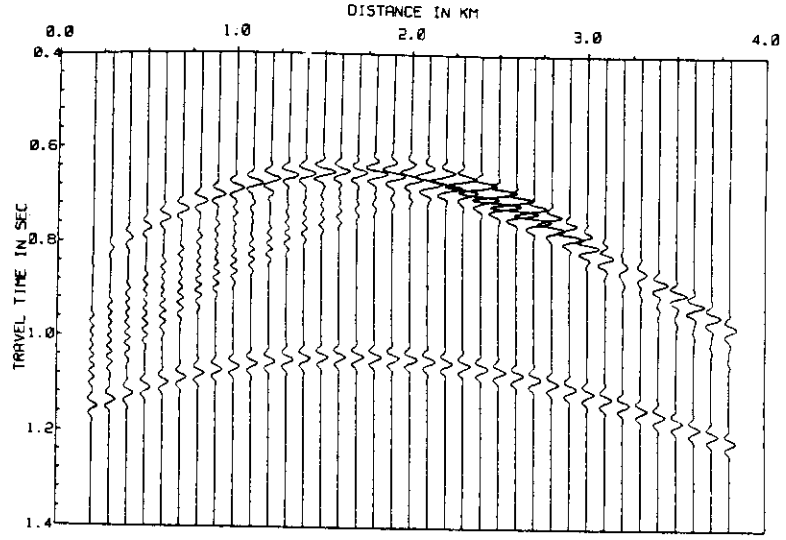

Fig. 4b. Ray-Born synthetic seismograms for the same configuration as in Fig. 4a, only a single scatterer is replaced by a system of seven scatterers. These individual scatterers form a corrugated interface of the length of 325 m. The scatterers are of the size of 25 x 25 m, the distance between them is also 25 m.

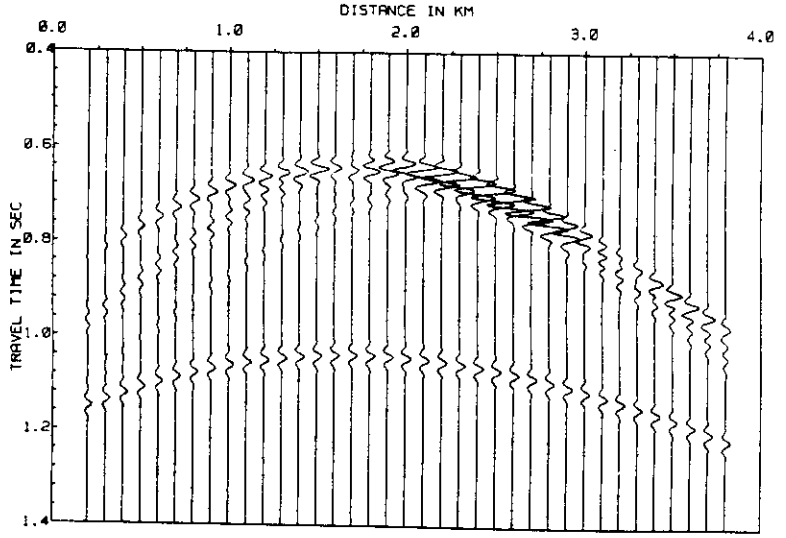

Fig. 4c. Ray-Born synthetic seismograms for the same configuration as in Fig. 4b, but the system of scatterers is continuous along the interface and simulates a continuous elevation of the interface in the length of 325 m. The elevation is formed by 13 single scatterers.

CONCLUSIONS

As we have shown, the numerical modelling of high-frequency seismic wave fields in 2-D laterally varying layered structures containing small scatterers can be simply performed by the combination of the ray theory with the Born approximation. Even though the presented numerical examples are very simple, the method could be applied to considerably more complex situations, e.g. to a random distribution of horizontal and/or vertical scatterers within some region, to combined scatterers of an arbitrary shape, etc. To simplify the explanations, only the acoustic case is discussed here, but the modification for an elastic isotropic and/or elastic anisotropic case is straightforward. Similarly, any algorithm for 3-D ray computations could be simply generalized to include the 3-D ray-Born modelling. The proposed method has several important limitations. It can only be used if the perturbations of the model are weak and if the wave field is of a high-frequency character. Moreover, only the single scattering is considered; multiple reflections between individual scatterers and inside the bodies of complex shape are not obtained.

ACKNOWLEDGEMENTS

This work was done during the first author's stay at the Federal University of Bahia, Salvador. The research was sponsored by the CNPq, FINEP, PETROBRAS and by the IBM Academic Initiative in Czechoslovakia.

REFERENCES

Beydoun, W.B. and M. Mendes, 1989. Elastic ray-Born l_2-migration/inversion. J. Geophys. Res., 97: 151-160.

Beylkin, G. and Burridge, R., 1990. Linearized inverse problems in acoustics and elasticity. Wave Motion, 12: 15-52.

Červený, V., 1987. Ray methods for three-dimensional seismic modelling. Lecture notes, The University of Trondheim and The Norwegian Inst. of Technology, Trondheim, Norway.

Červený, V., 1989a. Seismic ray theory. In: Encyclopedia of Solid Earth Geophysics, D.E. James (ed.), pp. 1098-1118, Van Nostrand Reinhold Co., New York.

Červený, V., 1989b. Synthetic body wave seismograms for laterally varying media containing thin transition layers. Geophys. J. Int., 99: 331-349.

Coates, R.T. and C.H. Chapman, 1990. Ray perturbation theory and the Born approximation. Geophys. J. Int., 100: 379-392.

Coppoli D.M., A., 1991. Ray-Born synthetic seismograms for complex structures containing scatterers. M.Sc. Thesis, PPPG/Federal University of Bahia, Salvador.

Wu, Ru-Shan, 1989a, Seismic wave scattering. In: Encyclopedia of Solid Earth Geophysics, D.E. James (ed.), pp. 1166-1187, Van Nostrand Reinhold Co., New York.

Wu, Ru-Shan, 1989b. The perturbation method in elastic wave scattering. Pageoph, 131: 605-637.

Geophys. J. Int. (1989) **99**, 331–349

Synthetic body wave seismograms for laterally varying media containing thin transition layers

V. Červený

Institute of Geophysics, Charles University, Ke Karlovu 3, 12116 *Praha* 2, *Czechoslovakia*

Accepted 1989 February 7. Received 1989 January 22; in original form 1988 October 2

SUMMARY

An approximate hybrid approach to computing high-frequency body wave synthetic seismograms in 2-D and 3-D laterally varying layered structures containing thin transition layers is suggested. It combines the ray method with the matrix (reflectivity) method. The ray method is applied to thick layers with smooth variations of velocity and the reflectivity method is applied to thin transition layers. Alternatively, the method of summation of Gaussian beams is used instead of the ray method in the hybrid code. An algorithm and the relevant program package BEAM87, designed for such hybrid computations in 2-D laterally varying layered structures containing one laterally varying thin transition layer, are briefly described. The thin transition layer may represent a region of a high velocity gradient, a laminated region, a region of a low Q, etc. It is simulated by a stack of very thin layers. The accuracy of the hybrid computations is tested on 1-D models by the comparison with reflectivity-method computations. The hybrid method yields sufficiently accurate results for transition layers, the thickness of which is smaller than one half of the prevailing wavelength of the wavefield under consideration, particularly for small angles of incidence. For reflected waves, the best accuracy is obtained for subcritical reflections, but the accuracy is lower for critical and overcritical reflections. The accuracy in the critical region is improved, if the Gaussian beam summation method is used instead of the ray method in the hybrid scheme. Numerical examples of synthetic body wave seismograms for a laterally varying model containing thin transition layers of various types are presented.

Key words: Gaussian beam summation method, ray method, reflectivity method, synthetic seismograms, thin transition layers

1 INTRODUCTION

The ray method and the Gaussian beam summation method are particularly suitable for the computation of high-frequency seismic wave fields in 2-D and 3-D laterally varying layered structures, if the model consists of thick layers with smooth variations of velocity, separated by smooth interfaces of the first order. These methods, however, cannot be applied to regions of high-velocity gradients. The zero-order ray theory predicts an approximate separation of P- and S-waves in regions of smooth velocity variations. In regions of a high-velocity gradient, the P- and S-waves interact and are coupled together. We speak about gradient coupling of P- and S-waves. The applicability of the ray method to regions of a high-velocity gradient is not improved, even if we consider higher terms of the ray series, or if we consider some extensions of the ray method, such as the method of the summation of the Gaussian beams, the Maslov method, etc.

The ray method is a high-frequency method; it gives best results for frequencies approaching infinity. In practical seismological applications, however, only finite frequencies are needed and considered in computations. The cut-off frequency used in computations depends mainly on the source time function under consideration. It is usually lower in seismological applications and higher in seismic prospecting. In numerical modelling of high-frequency seismic wave fields, the cut-off frequency is usually two- or three-times higher than the prevailing frequency of the source time function. Thus, even though we speak about a high-frequency method, we actually consider a cut-off frequency and relevant minimum wavelengths in the computations. If we investigate the interaction of the wavefield with objects of dimensions less than this minimum wavelength, the wavefield has, in fact, a relatively low-frequency character.

In seismology and in seismic prospecting, it is often useful to consider models in which certain layers are separated by some thin transition layers instead of interfaces of the first order. Under a thin transition layer we shall understand such a layer, the thickness of which is less than one half of the prevailing wavelength of the wavefield under consideration. The distribution of the velocity and of the velocity gradient across the thin transition layer may be arbitrary (a

ansition zone of a high velocity gradient, a laminated zone, c.). If the transition layer is thin, we expect that the wave cident on the transition layer will again generate two flected and two transmitted waves, similar to the case of 1 interface of the first order. Thus, we can divide the mplete wave field into individual contributions corsponding to rays with different trajectories, similarly as in ie case of smooth models containing interfaces of the first rder only.

In this paper, we shall concentrate on the numerical odelling of high-frequency seismic body waves, propagatg in 2-D and 3-D laterally varying layered structures, hich contain thin transition layers. Similar problems have een discussed by many authors, particularly for 1-D odels, and various methods have been proposed. As xamples, we refer to Scholte (1962), Richards & Frasier 1976), Chapman (1981, 1985), Chapman, Chu Jen-Yi & yness (1988), Kennett & Illingworth (1981) and Kennett 1983, 1988), where many other references can be found.

Here we propose and discuss an approximate hybrid nethod, which combines a numerically very efficient ray nethod, applied to the smoothly varying parts of the model, vith matrix (reflectivity) computations across thin transition ayers. The frequency-dependent reflection/transmission oefficients at thin transition layers computed by matrix nethods automatically include not only all multiply eflected, possibly converted, waves within stacks of thin ayers, but also various non-ray effects within the stacks evanescent waves, etc.). Various alternatives of such a ıybrid method were used previously in seismological iterature, mostly for 1-D media (see, e.g. Ratnikova 1973; Daley & Hron 1982; Baag & Langston 1985; Cummins & Johnson 1988). Following Daley & Hron, we shall call the above-described hybrid method the ray–reflectivity method.

For a 1-D medium, the justification of the hybrid method is based on the method of stationary phase, see Daley & Hron (1982). Even though the solution cannot be written in a closed integral form in a laterally varying structure, a modified approach can be used to justify the hybrid ray–reflectivity method even there (Babich, personal communication, an article is under preparation).

A similar hybrid method can be also obtained by combining the Gaussian beam summation approach and the reflectivity method (hybrid Gaussian beam summation–reflectivity method). As in the hybrid ray–reflectivity method, the Gaussian beam summation approach is applied to the smoothly varying parts of the model, and the reflectivity method is applied across the transition layers. The Gaussian beam summation method in the hybrid combination with the reflectivity method has several advantages over the ray–reflectivity method. The integration over the angles of incidence, which is automatically included in the Gaussian beam summation method, introduces automatically some smoothing and yields better results than the ray method in singular regions (caustics, critical regions, boundaries of shadow zones), particularly for waves reflected/transmitted at thin transition layers.

In Section 2, we propose a very efficient numerical algorithm for the computation of synthetic body wave seismograms in media containing thin transition layers. The program package BEAM87, written to perform such computations, is briefly outlined. In Section 3.1, the synthetic seismograms computed by the above described hybrid methods for several 1-D models are compared with those computed by the reflectivity method, in order to assess the accuracy of the proposed hybrid methods. Section 3.2 is devoted to numerical examples for laterally varying models, including laterally varying thin transition layers. Conlusions following from these test computations are briefly summarized in Section 4.

2 METHOD

As mentioned in the Introduction, the proposed method is based on the hybrid combination of the ray method (or the Gaussian beam summation method) and the matrix (reflectivity) method. The hybrid method is conceptually and algorithmically simple, particularly for vertically inhomogeneous media simulated by stacks of thick and thin parallel homogeneous layers. For this reason, we shall first describe the method for such a model, see Section 2.1. In Section 2.2, we shall then propose a generalization of this method for laterally varying structures, which contain thin, slightly curved, transition layers.

Under the medium parameters, we shall understand the velocities of P- and S-waves, the density and the quality factors of P- and S-waves.

2.1 Vertically inhomogeneous model

The model consists of thick layers, in which medium parameters slightly depend on the depth. The layers are separated either by interfaces of the first order or by thin transition layers, see Fig. 1. In transition layers, the medium parameters also depend on the depth, but the changes may be arbitrarily sharp (strong gradients of velocity, thinly layered inversion zones, etc.). Such a transition layer is

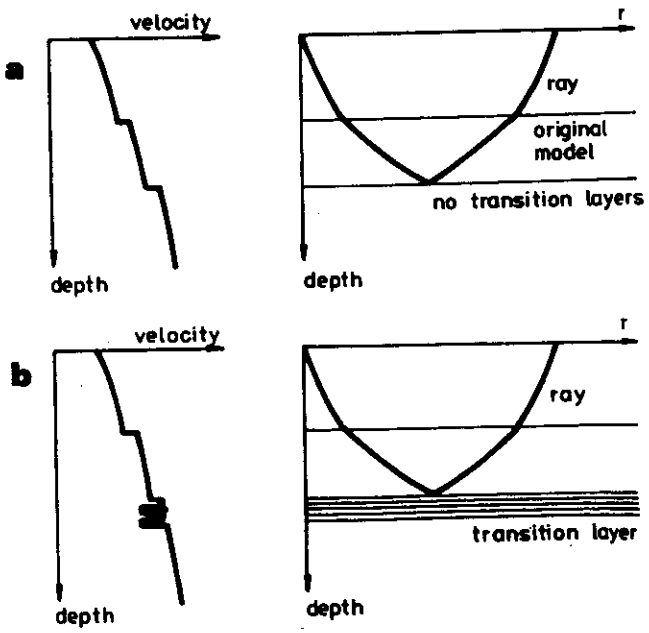

Figure 1. Top: vertically inhomogeneous layered model composed of thick layers with smooth velocity variations, separated by interfaces of the first order (original model). Bottom: a thin transition layer is inserted into the original model in the place of one of the interfaces of first order.

simulated by a stack of thin homogeneous parallel layers. Let us emphasize that all interfaces within the model are horizontal, including the top and bottom boundaries of the transition layer and the inner interfaces within the transition layer.

For such a 1-D model, the frequency response corresponding to an arbitrarily situated point source may be written in the well-known integral form (reflectivity integrals). The integral may be evaluated as a whole; then it includes all multiple reflections, including converted reflections. The other possibility is to divide the integral into contributions corresponding to rays. If these contributions are approximately evaluated by the method of stationary phase, we obtain standard ray contributions, which may be also obtained by the standard ray theory. In the case of thinly layered transition zones, however, the number of these ray contributions would be too great and computationally intractable. The third possiblity is to perform partial expansions, in which stacks of thin layers corresponding to transition zones are treated as a whole. Let us consider, for example, a wave reflected from such a stack of thin layers. In the integrand of the integral expression for this wave reflected from the stack, we obtain the frequency-dependent reflection coefficient from the stack as a multiplicative factor. If the reflection coefficient varies only slowly with the angle of incidence, and if the receiver is not in any singular region, the method of the stationary phase may be again used and an expression for the wave reflected from the stack of thin layers is obtained in an explicit form. The expression for the displacement vector of the reflected wave from a stack of thin layers will be quite the same as the ray method expression for a wave reflected from a single interface of the first order, situated on the place of the top boundary of the stack, only the relevant reflection coefficient from the interface of the first order must be replaced by the frequency-dependent reflection coefficient from the stack of thin layers.

Thus, the high-frequency seismic body waves propagating in a vertically inhomogeneous medium containing stacks of thin layers may be evaluated in the following two steps. In the first step, the ray method is applied to a fictitious model, from which all the thin transition layers were removed. The model is composed of thick layers with smooth velocity variations only, separated by interfaces of the first order. We shall call such a fictitious model the original model, see Fig. 1(a). In the second step, the new model, which also includes the thin transition layers is considered. Where the transition layers were introduced, the coefficients of reflection/transmission corresponding to the interfaces of the first order in the original model are replaced by frequency-dependent reflection/transmission coefficients at thin transition layers, computed by matrix methods (reflectivity method). Let us note that the traveltime correction, corresponding to the traveltime through the thin transition layer in the case of a transmitted wave, is automatically included in the transmission coefficients.

As the method has been derived for vertically inhomogeneous models, it only represents an approximate alternative of the reflectivity method which can be used to evaluate the wave field in such models exactly. The hybrid method gives the best accuracy for very thin transition layers, particularly for small angles of incidence. If we consider waves reflected from a thin transition layer, a high accuracy is obtained for subcritical reflections. The accuracy is lower in critical and overcritical regions.

Let us note that the frequency-dependent reflection/transmission coefficients automatically include all multiply reflected and converted waves generated within individual transition layers (stacks). Thus, the hybrid method drastically reduces the number of waves which should be included into computations since the multiply reflected and converted waves generated within individual stacks are included automatically. Moreover, the frequency-dependent reflection/transmission coefficients include even certain waves of a non-ray character, such as evanescent waves. Such waves cannot be computed by a standard ray method, even if they again transform to regular ray waves outside the transition layer.

2.2 Laterally varying structures

The approach discussed in Section 2.1 for a vertically inhomogeneous model may be simply generalized for laterally varying models. As in the standard ray method, the above-discussed procedures will be applied locally. Let us consider a wave incident on the top boundary of a thin transition layer. Let us select one ray of the incident waves, which intersects the top boundary of the transition layer at Q, and construct a normal to this boundary at Q. Then we locally simulate the actual thin transition layer in the vicinity of Q by a uniform stack of thin parallel homogeneous layers, perpendicular to the normal constructed at Q. The medium parameters in individual homogeneous layers are determined from the known distribution of medium parameters within the transition layers at Q. All other computations remain analogous to the case of vertically inhomogeneous media.

Let us discuss the approach in greater detail. We shall first consider a 2-D or 3-D model, consisting of thick layers separated by smooth interfaces of the first order, see Fig. 2(a). The medium parameters within the layers may vary both vertically and laterally, but only smoothly. We shall again call such a model the original model. Thus, the original model does not contain any thin transition layers.

Now we wish to construct a new model in which one of the interfaces of the first order is replaced by a thin transition layer, see Fig. 2(b). We assume that the interface under replacement varies only smoothly horizontally and

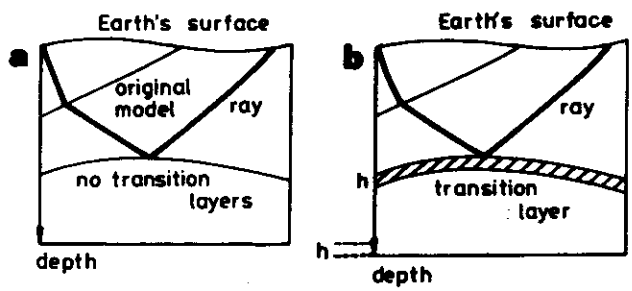

Figure 2. Left: laterally varying layered model composed of thick layers and blocks with smooth velocity variations, separated by interfaces of first order (original model). Right: a thin transition layer of constant vertical thickness h is inserted into the original model in the place of one of the interfaces of first order.

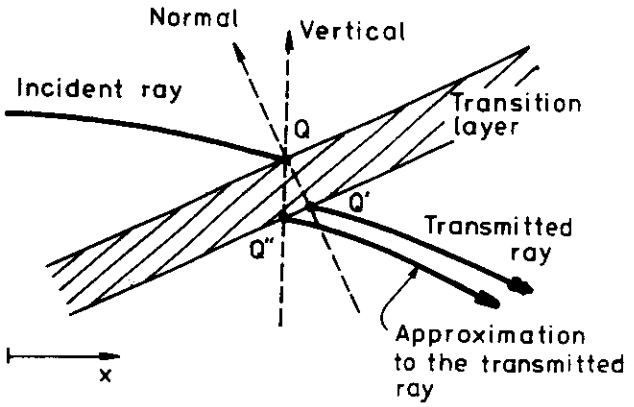

Figure 3. Transmission through a non-horizontal thin transition layer.

that it crosses the whole model over its entire horizontal extent. Also assume that the transition layer has a constant vertical thickness h and that the top and bottom boundaries of the thin transition layer have exactly the same geometrical shape as the interface which is to be replaced. The interface is replaced by the transition layer of constant vertical thickness h in the following way: The original model is divided by the interface into two parts, the overburden and the substratum, and the substratum is shifted down by h. The transition layer of constant vertical thickness h is then inserted into the free space between the overburden and the substratum. The structure of the overburden and/or of the substratum is not changed at all. Let us emphasize here that the transition layer has a constant vertical thickness, not a constant normal thickness. See Fig. 3, where the normal thickness corresponds to the distance QQ′, and the vertical thickness to the distance QQ″. The normal thickness of the transition layer may vary horizontally; it depends on the local dip of the layer. The higher the dip of the layer, the smaller its local normal thickness. The transition layer of constant vertical thickness can replace the interface of first order of the same shape; such a replacement only changes the vertical extent of the model. The total vertical extent of the new model equals the vertical extent of the original model plus the vertical thickness h of the transition layer. It is obvious that a thin transition layer of a constant normal thickness could not be inserted into the free space described above; any attempt to insert such a transition layer into the original model would deform the whole model.

It should be noted that an interface of the first order may be perhaps replaced by a transition layer even in some other ways; but all other ways would change the structure of the overburden and/or the substratum. The above described method leads to a simplest computational algorithm.

The medium parameters within the transition layer may vary arbitrarily in the vertical direction (sharp gradients, laminas, low or high-velocity layers, etc.). We shall again simulate the transition layer by a stack of thin homogeneous layers.

Let us now consider an elementary wave reflected from a thin transition layer. Then the computation of rays, traveltimes, global absorption factors t^* and ray propagators in the new model (containing the thin transition layer) may be performed in the same way as in the original model. The only difference is in the computation of the reduced amplitudes: the reflection coefficient from the interface of first order is replaced by the frequency-dependent reflection coefficient from the thin transition layer. Thus the computations for the original and for the new model differ only in the evaluation of the reflection coefficients.

The simulation of the thin transition layer of constant vertical thickness by a stack of thin homogeneous layers may be generalized. We can allow the medium parameters in individual thin layers, forming the transition layer, and their thicknesses to vary slightly horizontally. We can even allow to vary the effective thickness of the transition layer laterally by choosing the velocities in individually thin boundary layers within the transition layer locally close to the velocities in the overburden and/or in the substratum. The only requirements are that the variations are smooth and that the vertical thickness of the transition layer remains constant over the entire horizontal extent of the model. The computational algorithm remains the same as above, even if we consider the modified model.

The fact that the rays, traveltimes, global absorption factors and ray propagators need not be recomputed if we replace the interface of first order by a transition layer of constant vertical thickness (or if we replace one transition layer by another transition layer of a different vertical thickness and/or a different medium parameter distribution) plays a very important role in the computations; it leads to a very efficient algorithm.

For elementary waves transmitted through a transition layer, the situation is somewhat more complicated, see Fig. 3. Let us consider a wave incident on a thin transition layer and select a ray of the incident wave which impinges on the top boundary of the transition layer at point Q. We consider the top, bottom and inner boundaries of the transition layers locally plane and parallel in the vicinity of point Q, perpendicular to the normal at Q. Let us construct a vertical line and a normal line to the top boundary of the transition layer at point Q. The normal line intersects the bottom boundary of the transition layer at point Q′ and the vertical line at point Q″. In the original model, in which the transition layer is reduced to an interface of first order, all the three points Q, Q′ and Q″ coincide on the interface. The initial point of the ray of the wave transmitted through the interface is at point Q″, situated on the other side of the interface than the point of incidence Q. The frequency-dependent transmission coefficients at a thin transition layer, however, correspond to the normal, not to the vertical. Thus, we should use point Q′, not Q″, as the initial point of the ray of the transmitted wave in this case. This requires the recomputation of all rays, traveltimes, local absorption factors and ray propagators, if we consider the waves transmitted through the thin transition layer. Similarly as in a vertically inhomogeneous model, the traveltime correction, corresponding to the traveltime through the transition layer from Q to Q′ is automatically included in the frequency-dependent transmission coefficients.

For transition layers of very small dip and very small thickness, the distance between points Q′ and Q″ is very small and we can consider a simplification. If we use point Q″ instead of Q′, the error of computations will be small. Using Q″ instead of Q′, we may considerably simplify the

algorithm, in a similar way as for elementary reflected waves. The rays, traveltimes and the ray propagators need again be computed only once, for the original model, and the results are stored in a data file. The data file can then be used for the computation in new models which contain various transition layers (different vertical thicknesses, different inner structures, etc.).

In the explanations above, we have considered only one thin transition layer in the model. In principle, any number of transition layers may be used. The necessary requirements regarding these transition layers are as follows: (i) they are thin, (ii) they have constant vertical thickness, (iii) they cross the model over the entire horizontal extent of the model, (iv) they are only slightly curved and (v) the structure within the transition layers varies only slightly horizontally.

Program package BEAM87 was written to perform the proposed algorithm in 2-D models. It uses many parts from the earlier packages SEIS83 and BEAM84 described in Červený & Pšenčík (1984) and in Červený (1985a, b). In the present version, only one transition layer is considered, with at most three points of incidence on the transition layer along a single ray. The transition layer is simulated by a stack of very thin layers, the number of which remains the same along the whole transition layer. The structure within the transition layer is specified along vertical grid lines. At any grid line, the vertical thicknesses of individual thin layers forming the transition layer may be arbitrary, but the number of thin layers must be the same and the total vertical thickness of the transition layer must remain constant. The distribution of the medium parameters at individual grid lines may be quite arbitrary in the vertical direction, but their changes within the thin layers in the horizontal direction must be smooth. Between neighbouring grid lines, the thicknesses of thin layers and the medium parameters within the thin layers are determined by linear interpolation.

To evaluate the reflection/transmission coefficients for stacks of thin layers, routines RTMAT (for non-dissipative media) and RTMATQ (for dissipative media) written by G. Müller are used (see Müller 1985).

The algorithm used in BEAM87 does not require repeating the time consuming ray tracing and other relevant ray computations, if we change the thickness or the internal structure of the transition layer. In other words, as soon as a data file with the results of ray computations is available, we can use it for successive computations of frequency responses and synthetic seismograms corresponding to various thin transition layers. Computations may be optionally performed either by the ray–reflectivity or by the Gaussian beam summation–reflectivity approaches, by using the same data file with the results of ray computations.

3 NUMERICAL EXAMPLES

In this section we shall present several examples of 2-D computations of synthetic seismograms for models containing a transition layer. The computations were performed by program package BEAM87 based on the hybrid combination of the ray method with the reflectivity method, or, alternatively, on the hybrid combination of the Gaussian beam summation method and the reflectivity method.

In Section 3.1, we shall compare the synthetic seismograms, computed by the above-mentioned hybrid methods, with synthetic seismograms, computed by the reflectivity method (Fuchs 1968; Fuchs & Müller 1971). As the reflectivity method can be used (in its standard variant) only for models consisting of homogeneous plane parallel layers (including vertically inhomogeneous media simulated by a system of plane parallel homogeneous layers), for comparison we shall use only such a simple model. More specifically, we shall consider two homogeneous half-spaces separated by a transition layer of constant thickness. The object of this example is to assess the accuracy of the hybrid methods. In Section 3.2, we shall consider a laterally varying model, containing a thin transition layer of constant vertical thickness. We shall consider even a slightly laterally varying inner structure of the transition layer. In both sections, the thin transition layer is simulated by a stack of very thin layers.

As a source–time function, a standard Gabor signal is considered,

$$x(t) = \exp\{-[2\pi f_M(t-t_0)/\gamma]^2\}\cos[2\pi f_M(t-t_0)+\delta],$$

with four free parameters f_M, γ, t_0, δ. In all computations, the following parameters are selected: $\gamma = 4$, $f_M = 4$ Hz (prevailing frequency), $t_0 = 0$s, $\delta = 0$. All computations are performed in the frequency domain, with a frequency increment of 0.05 Hz. All synthetic siesmograms are bandpass filtered from 1.0 to 10 Hz, with the use of a zero phase-shift filter having a cosine taper from 1.0 to 1.5 Hz and from 9.5 to 10 Hz. The seismograms correspond to a vertical component of the displacement vector.

In the Gaussian beam computations, an important role is played by the choice of initial parameters of Gaussian beams used in the summation procedure. The parameters of the Gaussian beams are specified by the values of real and imaginary parts of the function M, representing the second derivative of the traveltime field with respect to the in-plane ray centred coordinate at the endpoint of the ray O_S, $M(O_S) = \mathcal{R}e\, M(O_S) + i\, \mathcal{I}m\, M(O_S)$. Note that $\mathcal{R}e\, M(O_S)$ controls the properties of the phase front of the Gaussian beam at O_S. It is related to the curvature of the phase front K, $K = v\, \mathcal{R}e\, M(O_S)$, where v is the relevant propagation velocity. $\mathcal{I}m\, M$ controls the width of the Gaussian beam at O_S. The relation between $\mathcal{I}m\, M(O_S)$ and the halfwidth of the Gaussian beam L for the frequency f(Hz) is as follows: $L = (\pi\, \mathcal{I}m\, M/f)^{-1/2}$. In all computations, we used the so called EPPF (effective plane phase front) choice to determine $\mathcal{R}e\, M(O_S)$, in which the phase front of any Gaussian beam is chosen locally plane at a point under consideration. The quantity $\mathcal{I}m\, M(O_S)$ was chosen manually and is constant for all termination points in a given computation. For more details on the choice of parameters of Gaussian beams in the summation formulae see Červený (1985b).

In all examples, the P-wave velocity varies from 6.4 to 8.2 km s^{-1} in the whole model, and the thickness of the transition layer is 1 km. As the prevailing frequency equals 4 Hz, the prevailing wavelength of P-waves varies from 1.6 to 2.05 km. Thus, the thickness of the transition layer is smaller than the prevailing wavelength of P-waves in all examples, the ratio thickness/wavelength is about 0.5–0.6.

We shall consider only perfectly elastic media. We shall

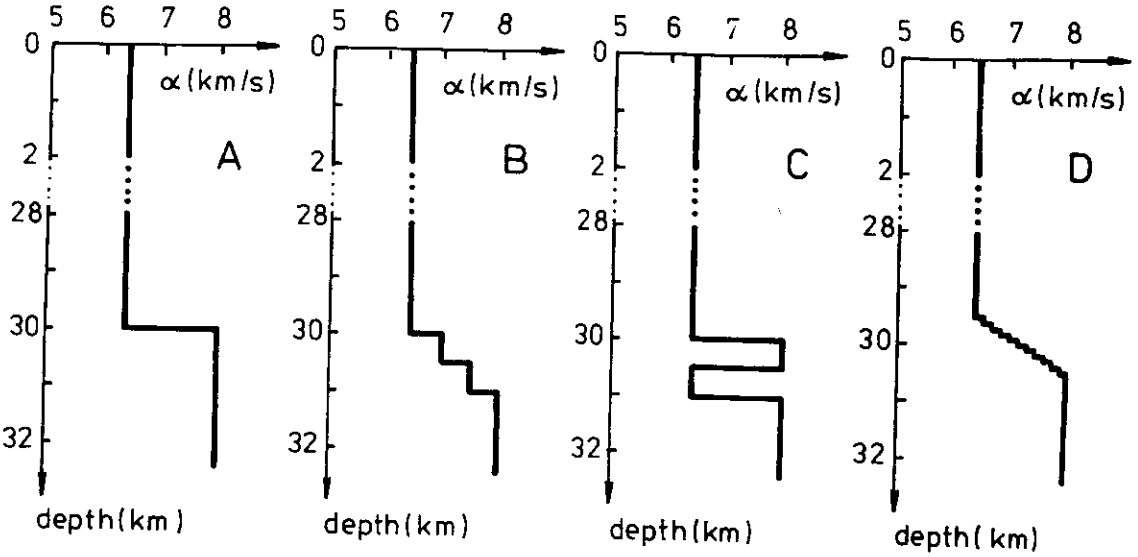

Figure 4. Models of the MOHO transition layer in a simple one-layer homogeneous Earth's crust, used in several numerical examples. (A) Interface of the first order, (B) 1-km thick stack of two homogeneous layers simulating a linear increase of velocity, (C) laminated zone 1 km thick (two laminae), (D) 1-km thick stack of 10 layers simulating a linear increase of velocity.

specify the structure by the distribution of the *P*-wave velocity α only. We assume that the *S*-wave velocity β and the density are related to the *P*-wave velocity α as follows: $\beta = \alpha/1.732$, $\rho = 1.7 + 0.2\alpha$.

3.1 Comparison with the reflectivity method

The simplest model which can be used to test the accuracy of synthetic seismograms, computed by the hybrid methods described above, is a model, consisting of two homogeneous half-spaces separated by a thin stack of layers of constant thickness. We shall consider here a model typical of the Earth's crust, with a transition layer simulating the Mohorovičić discontinuity (MOHO). Such a model is of some practical importance in deep seismic sounding of the Earth's crust. Moreover, many computations for such a model have been performed so that we have a good seismological feeling for the main peculiarities of seismic waves, reflected from this simple model of the MOHO.

This section is composed of four parts, 3.1.1–3.1.4. In the first part (3.1.1), we shall consider the model not containing the transition layer, the MOHO is simulated by an interface of the first order, see Fig. 4(A). In the next two parts (3.1.2 and 3.1.3), we simulate the MOHO by two different stacks of thin layers, see Figs. 4(B) and 4(C). In these three parts, synthetic seismograms of *PP*-waves, reflected from the MOHO, are computed by both hybrid methods and are compared with synthetic seismograms of the same waves, computed by the reflectivity method. Finally, in the fourth part (3.1.4), we present the frequency-dependent amplitude distance curves of all four reflected waves (*PP*, *PS*, *SP*, *SS*), including converted waves. These amplitude distance curves are computed by the hybrid Gaussian beam summation–reflectivity method.

3.1.1. *Model not containing a transition layer*

The model consists of a homogeneous crust (thickness 30 km, *P*-wave velocity 6.4 km s^{-1}) and a homogeneous upper mantle (*P*-wave velocity 8 km s^{-1}). An isotropic point source of explosive type is situated immediately close to the Earth's surface, at a point of horizontal coordinate $x = 320$ km. As we shall only discuss receivers situated at $x > 320$ km, the quantity $r = x - 320$ km represents the epicentral distance. Even though the point source is situated in the immediate vicinity of the Earth's surface, for simplicity we do not consider the effects of the Earth's surface on the radiation pattern of the source. The receivers are situated at points of x-coordinates $x = 330$, 335, . . . , 505, 510 km (i.e. at epicentral distances $r =$ 10, 15, . . . , 185, 190 km). At the receivers, the effects of the Earth's surface are considered, i.e. the conversion coefficients are applied.

Only one elementary wave is considered in our computations: the reflected *PP*-wave from the MOHO. The ray diagram, reduced traveltime curves (reduction velocity is 8 km s^{-1}) and ray amplitudes of radial and vertical amplitudes are shown in Fig. 5. The two-point ray tracing was used to perform these ray computations, so we can use both the ray method and the Gaussian beam method in all next computations. Although the synthetic seismograms are computed only at $x = 330$, 335, . . . , 505, 510 km, rays with termination points even outside this range are computed and shown in Fig. 5. The reason is that the Gaussian beam method will be optionally used for computations, and the Gaussian beam method requires the termination points of rays also in some vicinity of the receiver region to be considered. In the Gaussian beam summation computations, the quantity $\mathcal{S}_m M(O_S)$ was chosen as follows: $\mathcal{S}_m M(O_S) =$ 0.0003 s km^{-2}. This corresponds to the halfwidth of the Gaussian beams $L = 16.3$ km for the frequency of 4 Hz.

Let us note that the critical point is situated at epicentral distance $r = 80$ km ($x = 400$ km) in our simple model. The critical point is expressed by an anomalous increase of the amplitudes of reflected waves in Fig. 5.

Figure 6(a–c) shows the ray synthetic seismograms, the Gaussian beam synthetic seismograms and the reflectivity synthetic seismograms of *PP*-waves reflected from the MOHO in the simple model without a transition layer (see Fig. 4A). The ray synthetic seismograms are computed by a

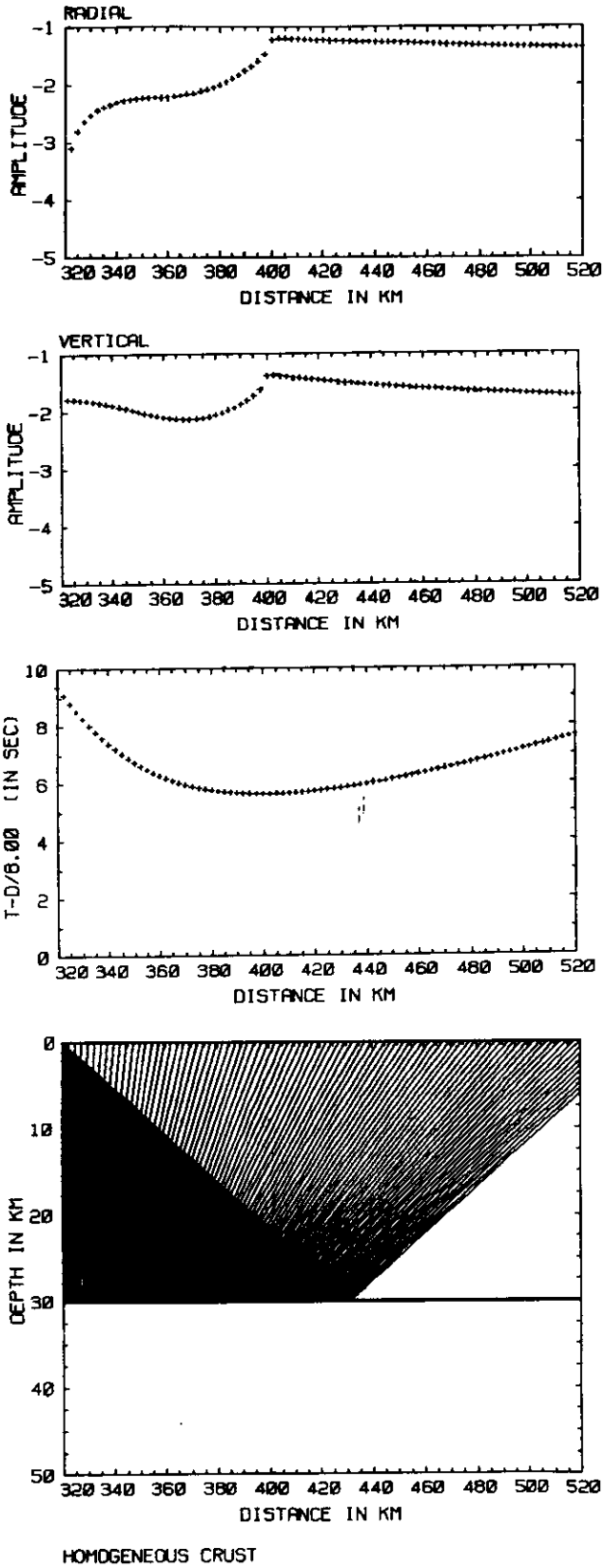

Figure 5. Ray computations for a *PP*-wave reflected from the MOHO in the original model of the one-layer homogeneous Earth's crust, see Fig. 4(A). Two-point ray tracing ray diagrams, reduced traveltimes and reduced amplitudes of the radial and vertical components of the displacement vector are shown.

standard ray method, so that the *PPP* head wave propagating under the MOHO is not considered.

Figure 6(a–c) is presented here only to remind us of the general pecularities of computed synthetic seismograms of reflected waves and to show the differences between individual methods of computation. The knowledge of these peculiarities and differences will be very useful in the next computations, which will take transition layers into account.

The general character of the synthetic seismograms in Fig. 6(a–c) is practically the same for both subcritical and overcritical regions. In the critical region, however, the differences are greater.

In ray synthetic seismograms (Fig. 6a) the amplitudes of reflected waves increase abruptly just before the critical point, attain their maxima at the critical point, and then slowly decrease. As mentioned before, the head wave is not computed here; that is why it does not appear in Fig. 6(a). It would, of course, be possible to compute the head wave by the ray method, see Červený & Ravindra (1971), but this is not done here.

The results obtained by the reflectivity method (Fig. 6c), are very similar to those obtained by the ray method, with two exceptions. (i) Reflectivity synthetic seismograms are different in the critical region. They do not display a sharp maximum at the critical point, but amplitudes smoothly increase in the vicinity of the critical point, and the maximum is shifted to larger distances. (ii) The weak head wave is well observable in the reflectivity seismograms.

Gaussian beam synthetic seismograms (Fig. 6b), are very similar to those computed by the two other methods in subcritical and overcritical regions. In the critical region, they are closer to the reflectivity synthetic seismograms. The Gaussian beam summation synthetic seismograms are more accurate than the ray synthetic seismograms in the critical region. The *PPP* head wave, however, has not appeared even in the Gaussian beam synthetic seismograms. In principle, it would be possible to obtain even the head waves by the summation of Gaussian beams, but it would be necessary to choose considerably broader Gaussian beams (lower $\mathcal{I}_m M$), see Konopásková & Červený (1984) and Section 3.1.4. Such a choice would not cause any difficulty in the case of a homogeneous crust, but may cause difficulties in computations for laterally varying structures. As we are concentrated here particularly on laterally varying models, we do not wish to use very broad Gaussian beams, which are not suitable for such models. This, of course, implies that the head wave does not appear in our Gaussian beam synthetic seismograms in Fig. 6b.

3.1.2 *Stack of two layers simulating a linear increase of velocity*

In this example, we replace the interface of the first order by a transition layer 1 km thick, simulating a linear increase of velocity. The linear transition layer is simulated by two homogeneous thin layers of 0.5 km thickness, see Fig. 4(B). The *P*-wave velocities in the two layers are 7 and 7.5 km s^{-1}, from the top to the bottom. All other parameters of computations remain the same as in the preceding example, including the choice of the parameters of Gaussian beams. Fig. 7(a–c) shows the synthetic seismograms of the waves reflected from the MOHO,

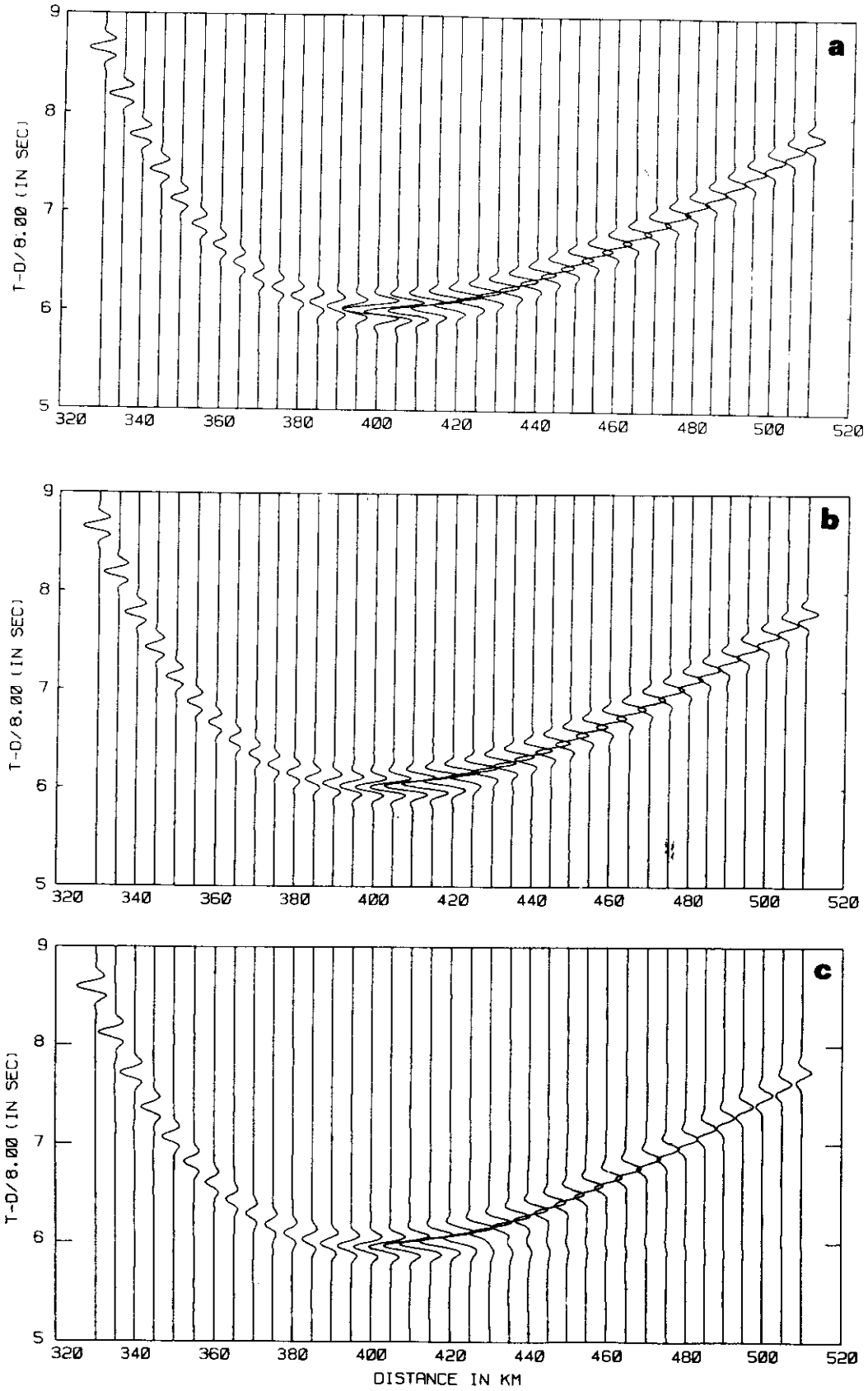

Figure 6. Synthetic seismograms of the vertical component of the displacement vector of the *PP*-wave reflected from the MOHO in the original model of a one-layer homogeneous Earth's crust, not containing any transition layer, see Fig. 4(A). (a) Hybrid ray–reflectivity computations, (b) hybrid Gaussian beam summation–reflectivity computations, (c) reflectivity computations.

computed by the hybrid ray–reflectivity, the Gaussian beam summation–reflectivity and the reflectivity method, respectively. Also in this case, the synthetic seismograms, computed by both hybrid methods, give a very good agreement with the reflectivity method in the subcritical region. As we can see from Fig. 7, the synthetic seismograms of subcritically reflected *PP*-waves virtually coincide. They are considerably weaker for the transition layer than for a sharp interface; compare with Fig. 6. Moreover, the time duration of the wavelet of the reflected wave is larger. Of course, all these phenomena were expected. In the critical region, the hybrid ray–reflectivity synthetic seismograms deviate considerably from the reflectivity seismograms. The Gaussian beam summation–reflectivity seismograms are again closer to the reflectivity seismograms. In the overcritical region, the accuracy of both hybrid methods is surprisingly good.

3.1.3 *Laminated zone*

In this example, we regard the MOHO as a 1-km thick laminated inversional zone, simulated by two laminas 0.5 km thick, see Fig. 4(C). In the top lamina, the *P*-wave velocity equals 8.0 km s^{-1}, in the bottom lamina 6.4 km s^{-1}. All other parameters of computations remain the same as in Section 3.1.1, including the choice of the parameters of Gaussian beams. Figure 8(a–c) shows the synthetic seismograms of *PP*-waves reflected from the MOHO, computed by the hybrid ray–reflectivity, by the hybrid Gaussian beam summation–reflectivity and by the reflectivity method, respectively. As we can see, the hybrid computations are again quite accurate in the subcritical region. As expected, the subcritical *PP* reflections are considerably stronger in this case than in the two preceding ones. Even the frequency content of subcritically reflected *PP*-waves is obviously rather different from that of the reflected waves in the two preceding cases. In critical and overcritical regions, the conclusions remain practically the same as in Section 3.1.2.

3.1.4 *Stack of* 10 *layers simulating a linear increase of velocity*

In the fourth example, we consider the MOHO as a transition layer 1-km thick, simulating a linear increase of velocities. The linear increase of velocities is simulated by 10 homogeneous thin layers 0.1 km thick. The source is situated 29.5 km from the upper boundary of the transition region. The purpose of these computations is different from that in the previous three examples. We do not present synthetic seismograms of *PP* reflected waves from the MOHO, but only the frequency-dependent amplitude distance curves in order to see the effects of the transition layer on the amplitude distance curves. But we consider not only *PP* reflected waves, but all four possible reflections: monotypic *PP*- and *SS*-waves and converted *PS*- and *SP*-waves. For *SS* and *SP* reflected waves, we consider an isotropic point source of *S*-waves polarized in the plane of the model, at the same place and of the same strength as the source of *P*-waves. Such an isotropic source of *S*-waves has only a formal meaning.

All computations are performed by the hybrid Gaussian beam summation–reflectivity method. To show that the hybrid method yields even head waves for sufficiently broad Gaussian beams, we choose broader Gaussian beams than in the previous cases. More specifically, we use $\mathcal{S}_m M(O_S) = 0.000043\ \mathrm{s\ km^{-2}}$, i.e. $L = 43$ km for *PP*- and *PS*-waves, and $\mathcal{S}_m M(O_S) = 0.000075\ \mathrm{s\ km^{-2}}$, i.e. $L = 32.6$ km for *SS*- and *SP*-waves, for the frequency 4 Hz. Such broad Gaussian beams guarantee a high accuracy of computations, see Konopásková & Červený (1984). Owing to considerably more accurate computations, a denser ray diagram for a broader range of initial angles was computed.

Figure 9 shows the amplitude distance curves of reflected *PP*-, *PS*-, *SP*- and *SS*-waves for the frequency 4 Hz. To make the figures more illustrative, amplitude distance curves for the model described in Section 3.1.1 (without the transition layer) are presented in all of them for comparison. As we can see, the amplitude distance curves are not simple, particularly for *SS* reflected waves. To understand these curves better, let us give here critical distances for individual reflected waves:

PP reflected wave: the critical point corresponding to the *PPP* head wave is situated at $r = 80$ km.

PS reflected converted wave: the critical point corresponding to the *PPS* head wave is situated at $r = 55.6$ km.

SP reflected converted wave: the critical point corresponding to the *SPP* wave is situated at $r = 55.6$ km.

SS reflected wave: there are three critical points in this case. The critical point, corresponding to the SP_2S head wave is situated at $r = 31.2$ km, to the SP_1S head wave at $r = 42.4$ km and to the *SSS* head wave at $r = 80$ km. Here the SP_1S head wave has a *P* element above the interface, and the SP_2S head wave has it below the interface.

In the amplitude distance curves of *SS* and converted waves, we can observe even other anomalous regions. They correspond to the Brewster angles, for which the relevant reflection coefficients vanish. The Brewster angle for the *PS*-wave corresponds to the epicentral distance $r = 52$ km, for the *SS*-wave to $r = 27$ km and for the *SP*-wave to $r = 52$ km.

The oscillations of the amplitude distance curves beyond the critical points indicate the existence of head waves of the relevant type. The strongest oscillations of the amplitude distance curves can be observed in the graphs for *PP* and *SS* reflected waves, indicating strong *PPP* and *SSS* head waves. The *PPS* and *SPP* head waves are relatively weaker, and the oscillations due to head waves SP_1S and SP_2S are not observed at all. As we can see in all figures, the amplitude distance curves close to the relevant critical points are smooth, they do not display sharp amplitude changes. This is due to the smoothing effect of Gaussian beams. A similar behaviour can be observed even in the vicinity of the Brewster angles.

If we compare the amplitude distance curves of reflected waves from an interface of the first order and from a linear transition layer, we can draw the following conclusions. (i) In subcritical regions, the amplitudes of waves reflected from a linear transition layer are in general considerably weaker than the amplitudes of waves reflected from an interface of the first order. This applies to all reflected waves under consideration (*PP*, *PS*, *SP*, *SS*). We have presented here the results for one frequency only, but it would be

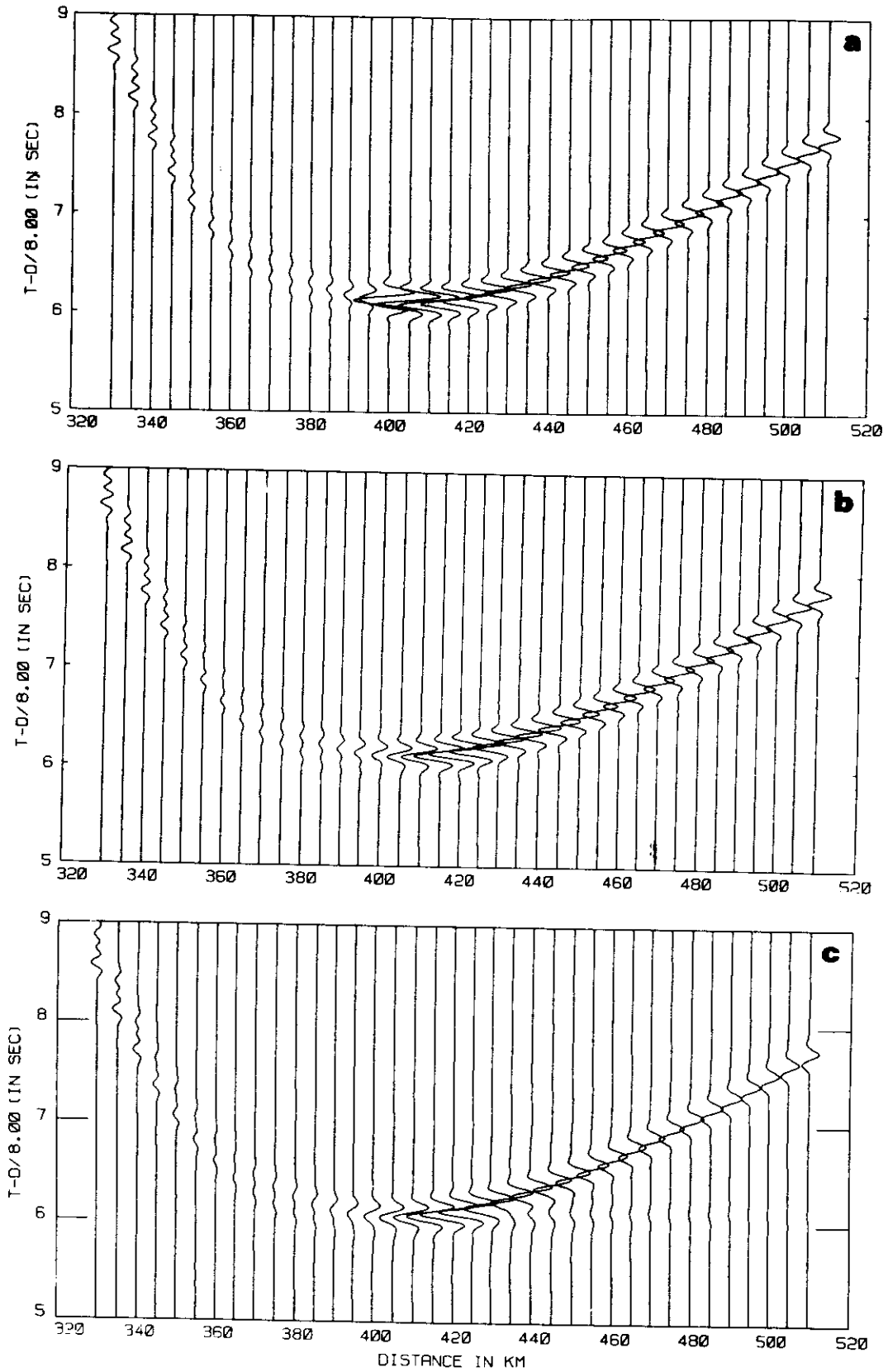

Figure 7. Synthetic seismograms of the vertical component of the displacement vector of the *PP*-wave reflected from the MOHO in the model of a one-layer homogeneous Earth's crust. The MOHO is represented by a 1-km thick stack of two homogeneous thin layers simulating a linear increase of velocity, see Fig. 4(B). (a) Hybrid ray–reflectivity computations, (b) hybrid Gaussian beam summation–reflectivity computations, (c) reflectivity computations.

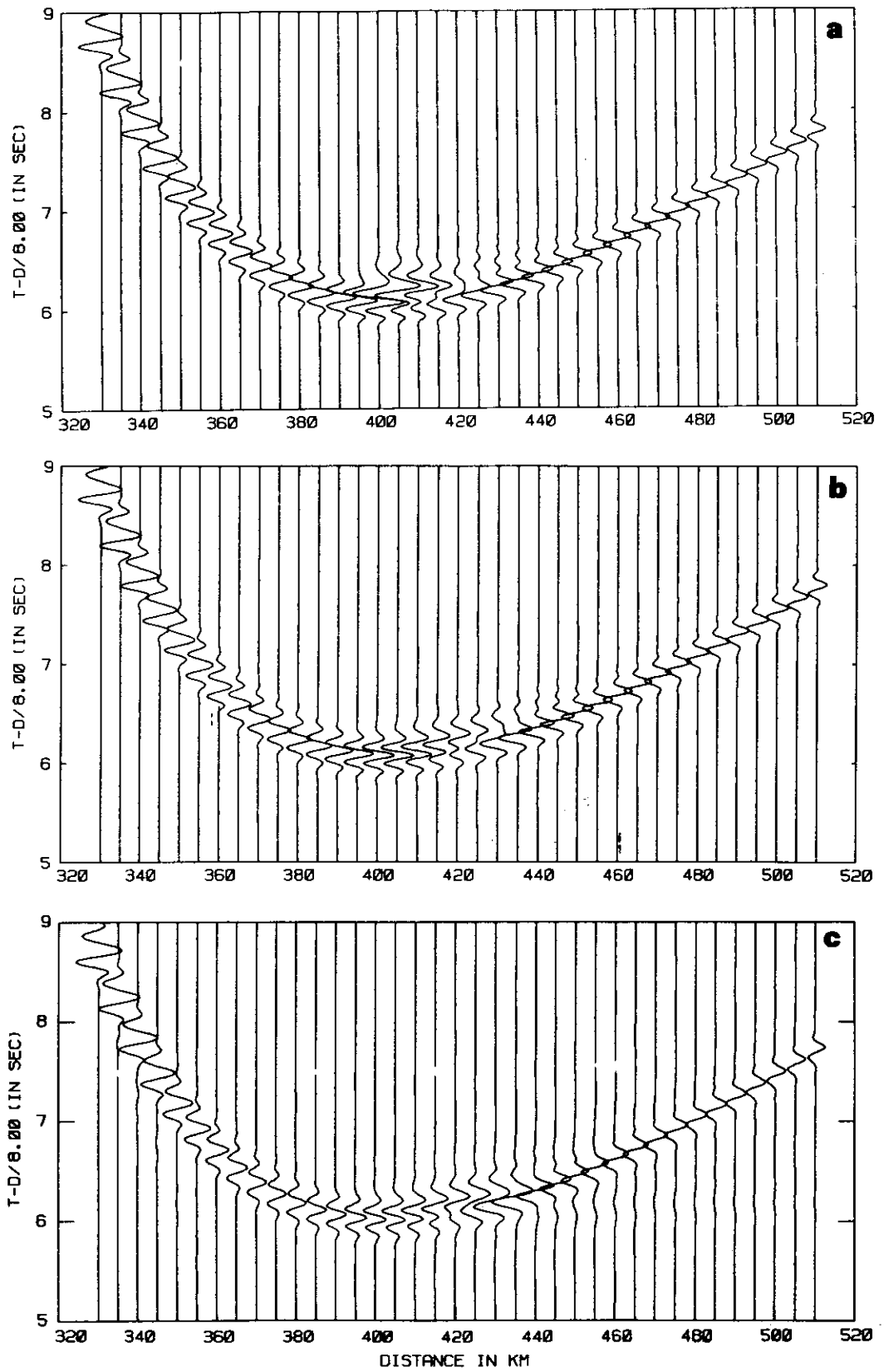

Figure 8. Synthetic seismograms of the vertical component of the displacement vector of the *PP*-wave reflected from the MOHO in the model of a one-layer homogeneous Earth's crust. The MOHO is represented by a 1-km thick stack of two homogeneous laminae, see Fig. 4(C). (a) Hybrid ray–reflectivity computations, (b) hybrid Gaussian beam summation–reflectivity computations, (c) reflectivity computations.

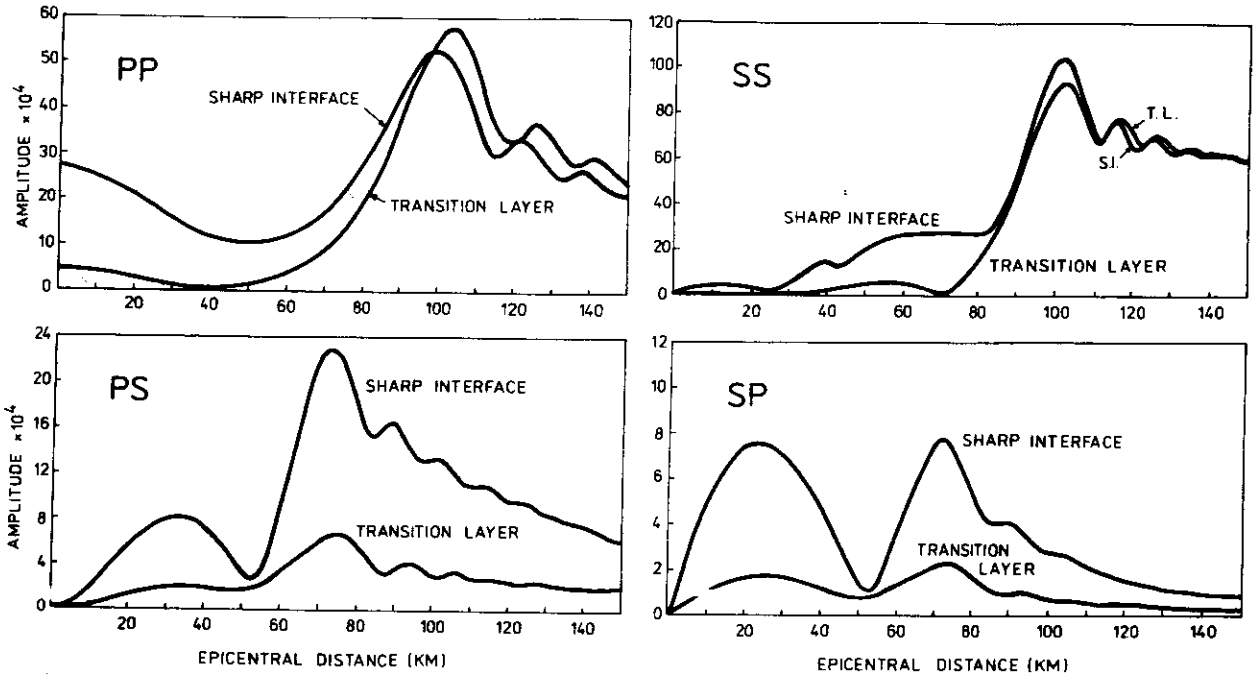

Figure 9. Amplitude distance curves of the vertical component of the displacement vector of the *PP*-, *PS*-, *SP*- and *SS*-waves reflected from the MOHO in a one-layer homogeneous Earth's crust, for frequency 4 Hz. Two models of the MOHO are considered: (a) interface of the first order, see Fig. 4(A), (b) 1-km thick stack of 10 thin homogeneous layers, simulating a linear increase of velocity, see Fig. 4(D). Computations are performed by the hybrid Gaussian beam summation–reflectivity method. The oscillations correspond to relevant head waves.

possible to see from similar computations for other frequencies that the subcritical reflections from a linear transition layer are the lower, the higher the frequency is. (ii) For overcritical reflections of converted waves, the results are the same as for subcritical regions. (iii) For overcritical reflections of the *PP* reflected wave and for the overcritical reflection of the *SS* reflected wave beyond the critical point corresponding to the *SSS* head wave, the amplitudes of the reflected waves from an interface of first order and from a linear transition layer remain roughly the same. The reflected wave from a transition layer may be even stronger than the reflected wave from the interface of first order. See also Töpferová & Červený (1987) for other similar examples.

3.2 Laterally varying structures

In this section, we shall demonstrate the possibilities of the hybrid ray–reflectivity (Gaussian beam summation–reflectivity) method in the computation of high frequency seismic wave fields in laterally varying layered models, containing one transition layer of constant vertical thickness. In all examples, the ratio vertical thickness/prevailing wavelength is close to 0.5–0.6. The transition layer may be slightly curved like other interfaces of first order in the model. The changes of the medium parameters within the transition layer may be arbitrarily strong in the vertical direction. We shall, however, allow even smooth changes of the medium parameters in the horizontal direction.

For laterally varying structures, the reflectivity method (in its standard variant) cannot be used in computing synthetic seismograms. For this reason, we shall present here only synthetic seismograms, computed by the hybrid ray–reflectivity method and by the hybrid Gaussian beam summation–reflectivity method.

As a laterally varying layered model, we shall consider here model ZURICH, which has been used many times in various test computations, both in ray computations and in the Gaussian beam summation computations. Model ZURICH is a 2-D model of a two-layer Earth's crust. Both the Mohorovičić discontinuity and the intermediate interface within the Earth's crust vary laterally. The *P*-wave velocity within individual layers varies laterally, see Fig. 10. The isotropic point source of *P*-waves is situated in close vicinity of the Earth's surface, at $x = 320$ km. The interaction of the source with the Earth's surface is not taken into account. The source time function again corresponds to a Gabor signal with the same parameters as in Section 3.1. The receivers are situated on the Earth's surface, at the same epicentral distances as in Section 3.1, i.e. at $r = 10, 15, \ldots, 185, 190$ km ($x = 330, 335, \ldots, 505, 510$ km). Fig. 11 shows ray diagrams, traveltimes and ray amplitudes of radial and vertical components of three important waves: the *PP* reflected wave from the intermediate interface (left column), the reflected *PP*-wave from the MOHO and the refracted wave within the second layer (right column). As we can see in Fig. 11, the reflected wave from the intermediate interface has a critical point at $x = 385$ km ($r = 65$ km) and a boundary point at $x = 500$ km ($r = 180$ km). Likewise, the critical point, corresponding to the *PP*-wave reflected from the MOHO, is situated at $x = 410$ km ($r = 90$ km) and the boundary point at $x = 485$ km ($r = 165$ km). Naturally, the *P* refracted wave in the second crustal layer exists between the epicentral distances 65 and 165 km (x from 385 to 485 km). The slightly

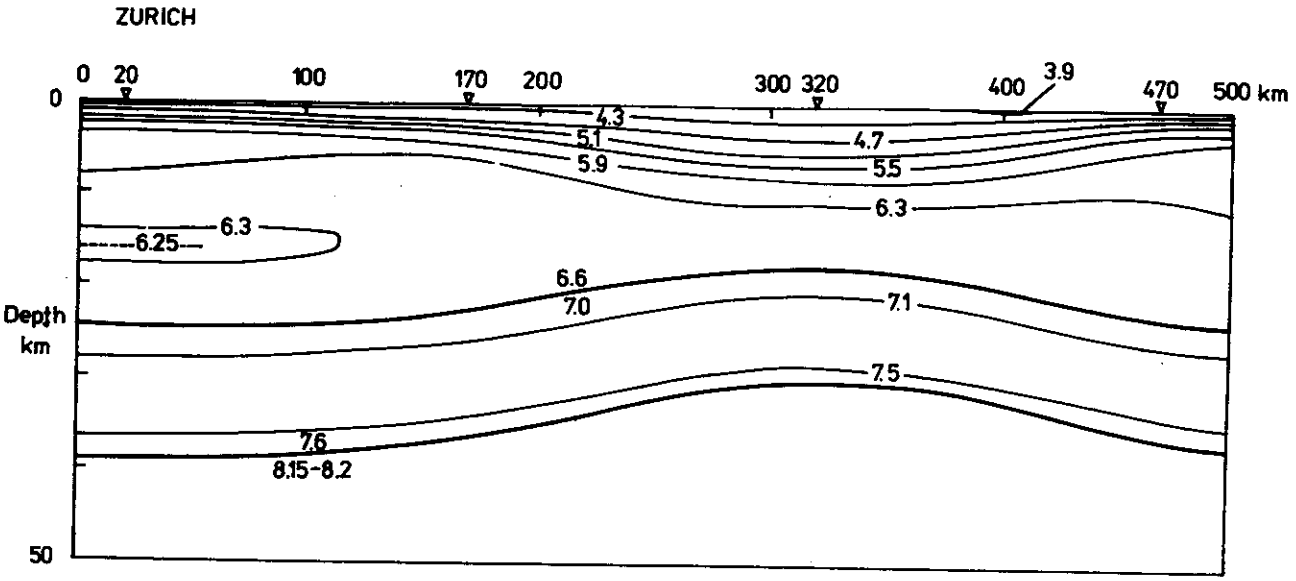

Figure 10. 2-D model ZURICH used for the computations of several numerical examples. It represents an original laterally varying layered model of a two-layer Earth's crust, not containing any transition layer. The bold lines denote interfaces, the thin lines isolines of velocity. The shot point is situated at $x = 320$ km.

refracted wave below the MOHO (not shown in Fig. 11) exists only beyond $x = 410$ km.

As we are mainly interested in the properties of reflected waves, we shall not consider here the *P*-wave refracted in the first layer. Since the refracted *P*-wave in the first layer is very intensive at small epicentral distances, it would be necessary to introduce an amplitude scaling to decrease its amplitudes at small epicentral distances in the synthetic seismogram sections. Such an amplitude scaling would, however, completely destroy the weak *PP* subcritical reflections which are of primary interest. Thus, in all cases we shall present synthetic seismograms in absolute (non-scaled) amplitudes. In all hybrid Gaussian beam summation–reflectivity computations, we shall use the choice of the parameters of Gaussian beams as in Section 3.1; we only use a larger $\mathcal{I}_m M(O_S)$: $\mathcal{I}_m M(O_S) = 0.001\ \mathrm{s\,km^{-2}}$, i.e. $L = 8.9$ km for frequency 4 Hz. In other words, the Gaussian beams used here in the summation are even narrower than in Sections 3.1.1–3.1.3; with the halfwidth $L = 8.9$ km for frequency 4 Hz at O_S. We choose a smaller width because of the stronger lateral variations of velocity in the model. Such stronger variations require narrower Gaussian beams, see Červený (1985b).

We shall consider four models which will only differ in the structure of the MOHO, see Fig. 12. In the first model (4.1.1), no transition layer is considered, the MOHO is an interface of the first order. In the other three models (4.1.2–4.1.4), the MOHO discontinuity is replaced by a 1 km thick transition layer. The velocity distribution does not change laterally in the models in Sections 4.1.2 and 4.1.3, but varies laterally in the model in Section 4.1.4.

4.1.1 *Model not containing a transition layer*

As in Section 3.1, we shall first consider the original model ZURICH not containing any transition layer; see Fig. 12(A). Ray synthetic seismograms for this model are shown in Fig. 13(a) and the Gaussian beam summation synthetic seismograms in Fig. 13(b). Remember that the refracted wave in the top crustal layer is not shown in Fig. 13(a–b). Like in Section 3.1.1, we can see that the differences between the synthetic seismograms, computed by the two methods, are very small at subcritical distances. Close to the relevant critical points, we can observe well-known differences. The ray synthetic seismograms yield a sharp increase of amplitudes at the critical point, but the Gaussian beam summation seismograms are smooth there; their maximum amplitudes are shifted to larger epicentral distances. Other great differences can be observed at the boundaries of shadow zones. The ray amplitudes abruptly vanish at the relevant distances, but the Gaussian beams give a smooth transition from an illuminated region to the shadow zone. All sharp changes of amplitudes are smoothed in the Gaussian beam summation method.

4.1.2 *Stack of two layers simulating a linear increase of velocity*

In this example we shall replace the first order MOHO by a 1-km thick transition layer, simulating a linear increase of velocity with depth. The transition layer is simulated by two thin homogeneous layers 0.5 km thick; see Fig. 12(B). Synthetic seismograms, computed by the hybrid Gaussian beam summation–reflectivity method for this model, are shown in Fig. 14. We shall not present here the synthetic seismograms computed by the hybrid ray–reflectivity method, but only the synthetic seismograms computed by the hybrid Gaussian beam summation–reflectivity method. As we can again see, the transition layer exerts great influence mainly on the subcritical reflections. The subcritical reflections from the transition layer with a linear increase of velocity practically vanish. As in Section 3.1, we do not observe any pronounced differences between the reflected *PP*-waves from a sharp-interface MOHO and from the linear-transition-layer MOHO at overcritical distances.

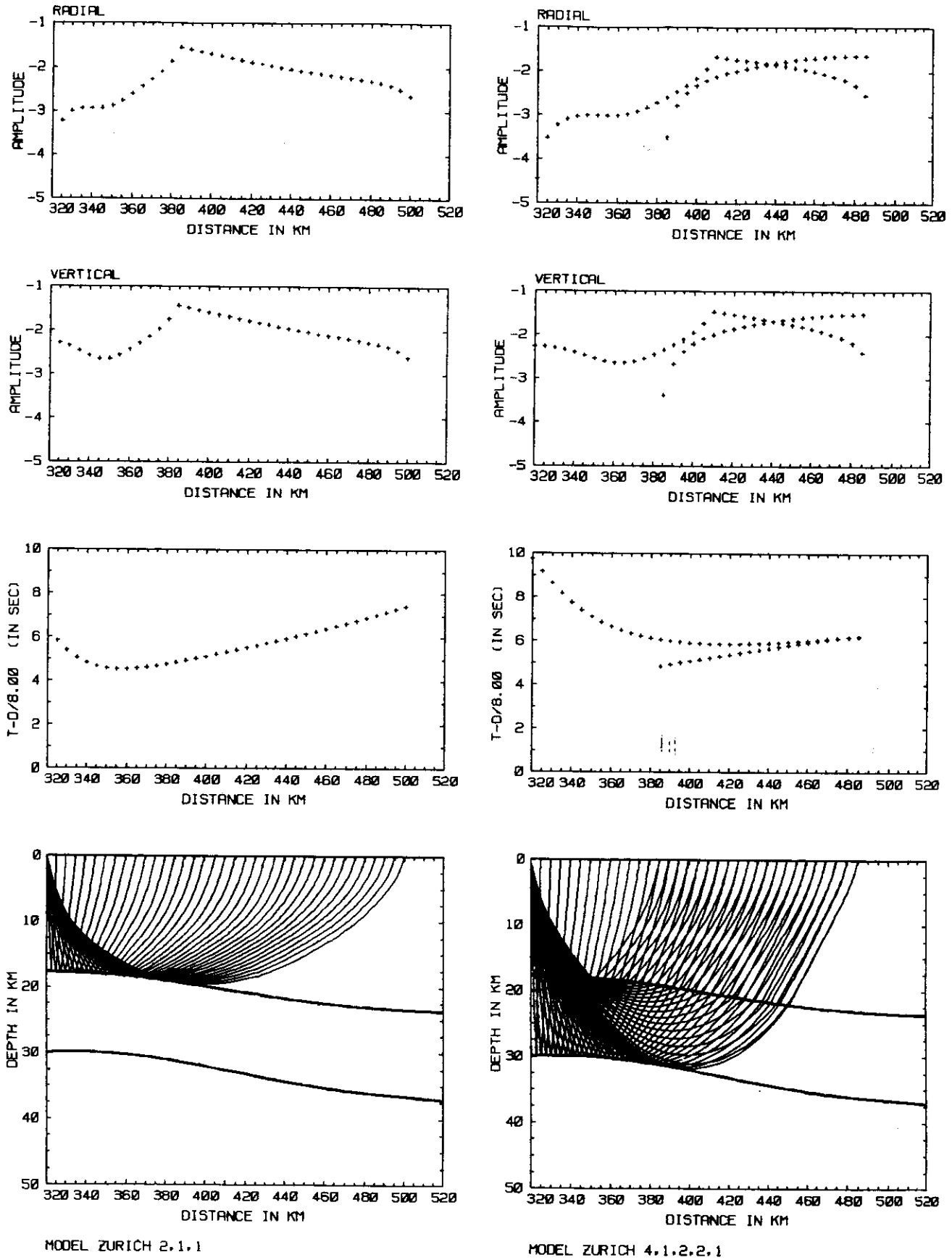

Figure 11. Some ray computations for the *PP*-waves, reflected from the intermediate interface and from the MOHO, and for the *P*-wave, refracted in the second layer, all of them in model ZURICH, see Fig. 10. The *P*-waves refracted in the first layer and below the MOHO are not shown. Two-point ray tracing ray diagrams, reduced traveltimes and reduced ray amplitudes of radial and vertical components of the displacement vector are shown.

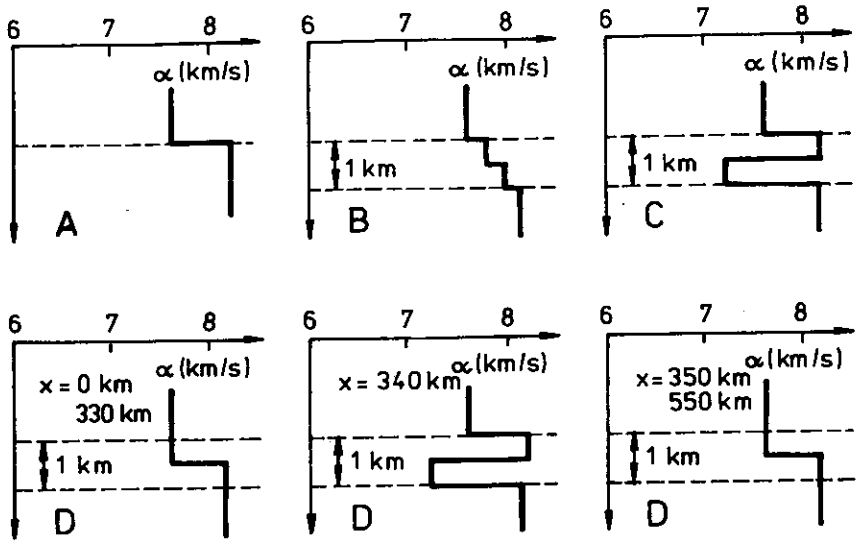

Figure 12. Models of the MOHO transition layer in model ZURICH, used in numerical examples. (A) Interface of the first order, (B) 1-km thick stack of two homogeneous layers simulating a transition layer with a linear increase of velocity, (C) 1-km thick laminated zone (two laminae), (D) 1-km thick laterally varying stack of two layers. The *P*-wave velocity distribution is shown along five vertical grid lines. Horizontal linear interpolation is used to determine the velocity between individual grid lines.

4.1.3 *Laminated zone*

In this example we replace the first order MOHO by a 1-km thick laminated inversional stack of layers. The stack is composed of two laminae 0.5 km thick. The *P*-wave velocity in the top layer is 8 km s^{-1}, close to the velocity in the uppermost mantle. The *P*-wave velocity in the bottom layer is 7.2 km s^{-1}, close to the velocity in the deep crust; see Fig. 12(C). From the seismological point of view, the transition region represents an upper mantle material intruded into the deep crust. Synthetic seismograms computed by the hybrid Gaussian beam summation–reflectivity method for the model above are presented in Fig. 15. As we can again see, the most pronounced changes in the amplitudes of the *PP* reflected waves from the MOHO due to the laminated stack of layers can be observed at subcritical distances. The amplitudes for these distances are rather high; they are close in magnitude to the amplitudes in the critical region. It would be difficult to identify the critical region from an increase in amplitudes in this case. In the overcritical region, the differences in amplitudes for different types of the MOHO transition region are not as distinct as in the subcritical region.

4.1.4 *Laterally varying stack of thin layers*

In this example we replace the first order MOHO by a 1-km thick laterally varying transition layer. The transition layer is composed of two thin layers 0.5 km thick. The *P*-wave velocity in these two layers is specified on vertical grid lines at five distances, as shown in Table 1, see also Fig. 12(D). The *P*-wave velocity between these distances is determined by a linear interpolation. Let us now briefly describe the model from a seismological point of view. We remind that the *P*-wave velocity just above the MOHO in the original model is close to 7.6 km s^{-1}, and the *P*-wave velocity below it is 8.15 km s^{-1}. Thus, the stack with the velocities 7.6 km s^{-1} in the top layer and 8.15 km s^{-1} in the bottom layer actually represents again an interface of the first order, but shifted 0.5 km down. With the exception of the region $330 < x < 350$ km, model 4.1.4 represents a MOHO interface of the first order, but shifted 0.5 km down. This type of the MOHO discontinuity is, however, disturbed at $x = 340$ km, where the model represents a laminated stack composed of two laminae 0.5 km thick: the velocity in the top layer roughly corresponds to the uppermost mantle material, the velocity in the bottom layer to the deep crust material. As we know, such a inversional zone generates very strong *PP* subcritical reflections, see Section 3.2.3. Thus, we can locally expect very strong subcritical *PP* reflections, approximately at epicentral distance $2 \times 20 = 40$ km ($x = 360$ km). But the linear interpolation between the grid lines at $x = 330$ and 340 km will generate a linear transition layer stack $x = 332$–334 km, which will yield very weak reflections at $x = 344$–348 km. A similar decrease of amplitudes will be observed also at 372–376 km.

Synthetic seismograms computed by the hybrid Gaussian beam summation–reflectivity method for this model are shown in Fig. 16. The amplitudes of *PP*-waves reflected from the MOHO at epicentral distances less than 340 km and greater than 380 km roughly correspond to the amplitudes of *PP*-waves reflected from a first order MOHO, see Section 3.2.1 and Fig. 13. In regions $x = 344$–348 km and $x = 372$–376 km, they correspond to waves reflected from a linear transition zone, see Section 3.2.2 and Fig. 14. Finally, at distances close to $x = 360$ km, they correspond to waves reflected from a laminated transition layer, see Section 3.2.3 and Fig. 15. For critical and overcritical regions, we obtain practically the same results as in Section 3.2.1.

4 CONCLUDING REMARKS

The inner structure and physical properties of various thin transition layers within the Earth's interior are of great importance in seismology and in seismic prospecting. Even

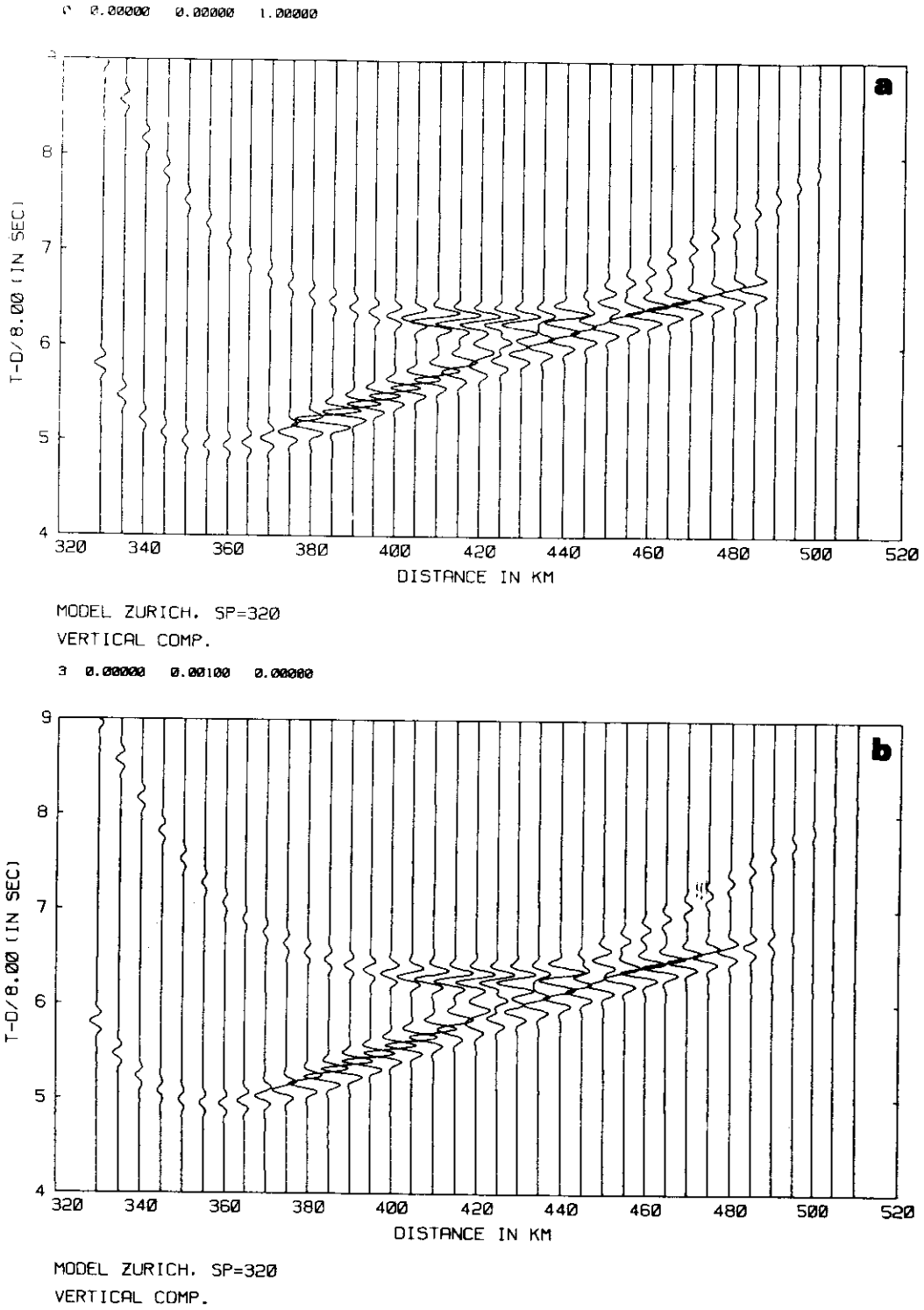

Figure 13. Synthetic seismograms of the vertical component of the displacement vector of the *PP* primary reflected waves, for model ZURICH (see Fig. 10) with the MOHO discontinuity respresented by an interface of the first order (see Fig. 12A). The *P* refracted wave in the first crustal layer is not considered in computations. (a) Hybrid ray–reflectivity computations, (b) hybrid Gaussian beam summation–reflectivity computations.

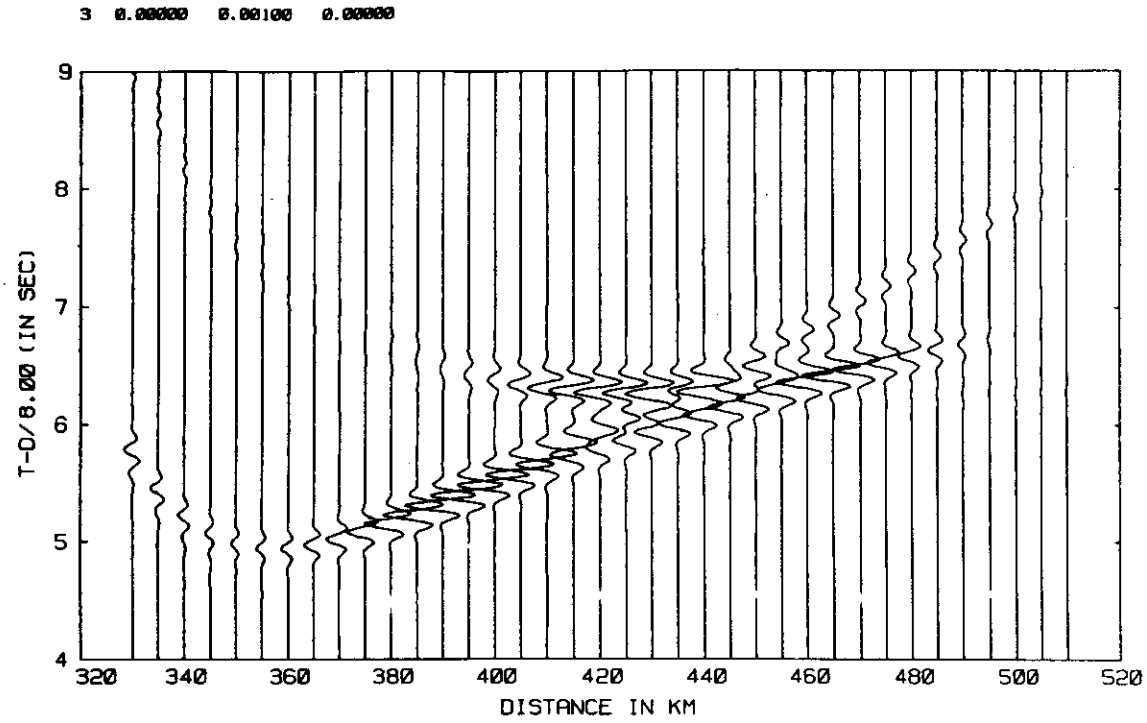

Figure 14. Synthetic seismograms of the vertical component of the displacement vector of *PP* primary reflected waves, for model ZURICH (see Fig. 10) with the MOHO discontinuity represented by a 1-km thick stack of two homogeneous layers simulating a transition layer with a linear increase of velocity (see Fig. 12B). The *P* refracted wave in the first crustal layer is not considered in computations. Computations are performed by the hybrid beam summation–reflectivity method.

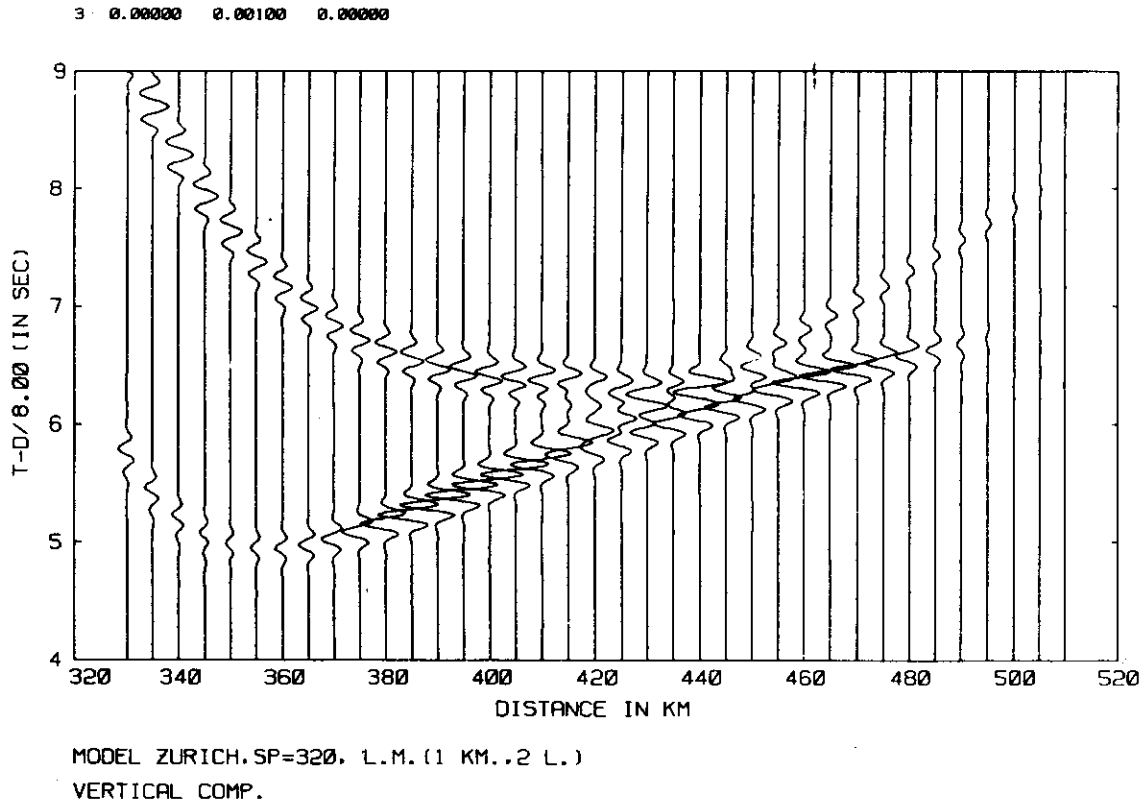

Figure 15. Synthetic seismograms of the vertical component of the displacement vector of *PP* primary reflected waves, for model ZURICH (see Fig. 10) with the MOHO dicontinuity represented by a 1-km thick laminated zone (see Fig. 12C). The *P* refracted wave in the first crustal layer is not considered in computations. Computations are performed by the hybrid Gaussian beam summation–reflectivity method.

Table 1. P velocities in laterally varying layered MOHO model.

	α(km s^{-1})	
x(km)	top layer	bottom layer
0	7.6	8.15
330	7.6	8.15
340	8.2	7.20
350	7.6	8.15
550	7.6	8.15

though the hybrid ray–reflectivity and Gaussian beam summation–reflectivity methods proposed in this article are only approximate, they may find very useful applications in a detailed investigation of such thin transition layers, the vertical thickness of which is less than one half of the prevailing wavelength of the wavefield under consideration. For subcritically reflected waves from thin transition layers, which are only slightly curved and in which the inner structure changes horizontally only slightly, the accuracy of the proposed hybrid codes seems to be quite sufficient for practical seismological investigations. The hybrid codes allow us to perform very efficient computations of synthetic seismograms, frequency responses, Fourier spectra, frequency-dependent amplitude distance curves and particle ground motion diagrams (polarization diagrams) of various seismic body waves interacting with the transition layers. These waves may be investigated independently from other waves if we wish to do so. In this article, we have not presented examples of frequency responses, Fourier spectra and particle ground motion diagrams of waves interacting with a thin transition layer, even though in various seismological investigations they may be more important than the synthetic seismograms themselves.

The hybrid approach proposed in the paper is only approximate and has various limitations. Similarly as in other high-frequency asymptotic methods, the validity conditions have mostly only qualitative character. The hybrid method, of course, fails in all cases when the ray method or the Gaussian beam summation method fails. We shall not review here these validity conditions, as they have been discussed broadly in the seismological literature. These validity conditions apply to the whole part of the medium through which the wave under consideration propagates. In addition to these general validity conditions, we have some special requirements related to thin transition layers. We require that the vertical thickness of the thin transition layer is less than one half of the prevailing wavelength. This condition, however, has again more or less a qualitative character. Finally, we require that the radius of curvature of the thin transition layer is considerably larger than the prevailing wavelength, and that the angle of incidence on the transition layer is small. In any case, the hybrid algorithm cannot guarantee sufficient accuracy of computations for critical and overcritical incidence and it will surely fail for grazing incidence. On the other hand, the medium

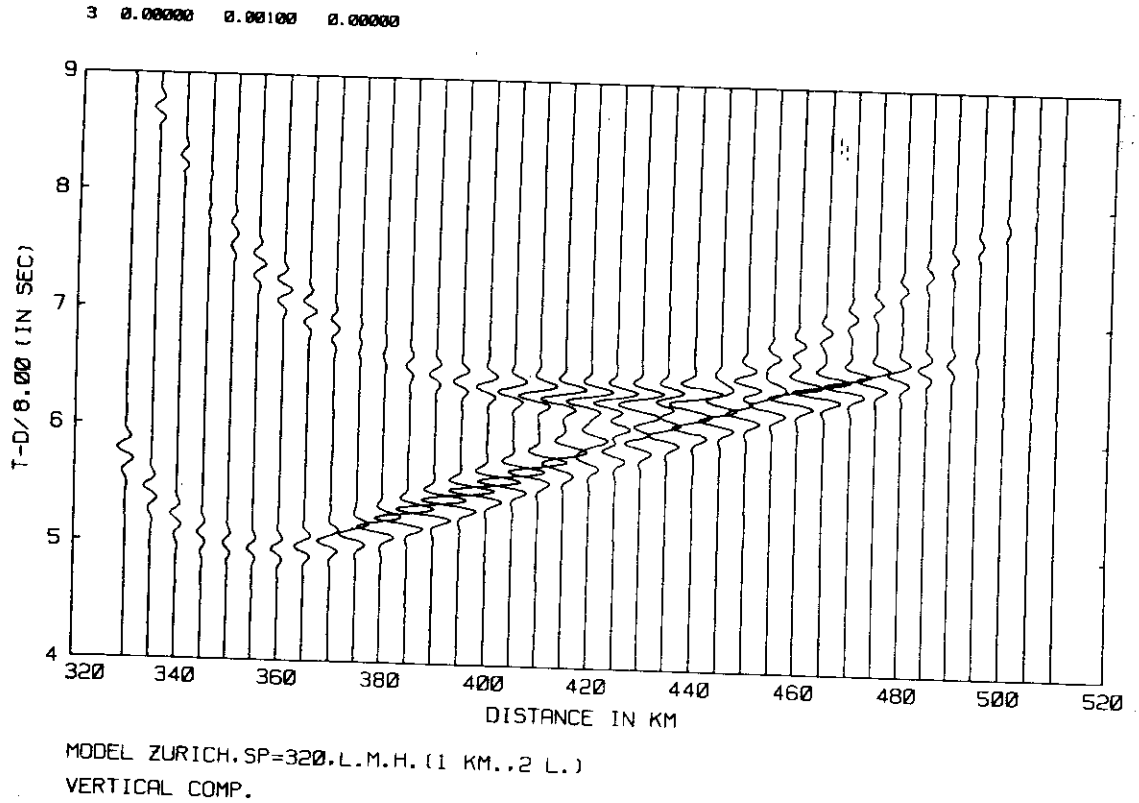

Figure 16. Synthetic seismograms of the vertical component of the displacement vector of PP primary reflected waves, for model ZURICH (see Fig. 10) with the MOHO discontinuity represented by a 1-km thick transition layer with a laterally varying internal structure (see Fig. 12D). The P-wave refracted in the first crustal layer is not considered in the computations. Computations are performed by the hybrid Gaussian beam summation–reflectivity method.

parameters within the transition layer may vary arbitrarily in the vertical direction.

The thin transition layers within the Earth's interior may have different inner structures and physical properties. They may represent a smooth transition layer, a linear transition layer with a high gradient of velocity, a laminated zone (i.e. a thinly layered inversional zone), a low velocity layer (e.g. a coal seam), a high velocity layer, a region of a low Q (high absorption), etc. Moreover, the properties of such thin transition layers may vary laterally. For example, they may form thin lense-like inclusions of high or low velocity, of low Q, etc. All such regions may be simply included into the proposed hybrid code and the relevant wave fields may be computed. The numerical examples presented in this article are very simple and have a more-or-less methodological character only.

A quite similar hybrid approach may be applied also in the case of a model with a thin transition region close to the surface. Since the structure of such regions is usually rather complex, the hybrid codes may considerably improve the ray method numerical modelling (or the Gaussian beam summation modelling). This fact was realized already a long time ago by Douglas, Hudson & Blamey (1973), who introduced a similar hybrid code in their programs. It would also be possible to use the thin subsurface layer to solve certain problems of seismic microzoning for laterally varying structures, and/or in the study of combined effects of seismic source, wave propagation and local geological structures close to the receivers.

REFERENCES

Baag, C. & Langston, C. A., 1985. A WKBJ spectral method for computation of SV synthetic seismograms in a cylindrically symmetric medium, *Geophys. J. R. astr. Soc.*, **80**, 387–417.

Červený, V., 1985a. Ray synthetic seismograms for complex two-dimensional and three-dimensional structures, *J. Geophys.*, **58**, 2–26.

Červený, V., 1985b. Gaussian beam synthetic seismograms, *J. Geophys.*, **58**, 44–72.

Červený, V. & Pšenčík, I., 1984. SEIS83—Numerical modelling of seismic wave fields in 2-D laterally varying layered structures by the ray method, in *Documentation of Earthquake Algorithms*, Report SE-35, pp. 36–40, ed. Engdahl, E. R., World Data Center for Solid Earth Geophysics, Boulder.

Červený, V. & Ravindra, R., 1971. *Theory of Seismic Head Waves*, University of Toronto Press, Toronto.

Chapman, C. H., 1981. Long-period corrections to body waves: theory, *Geophys. J. R. astr. Soc.*, **64**, 321–372.

Chapman, C. H., 1985. Ray theory and its extensions: WKBJ and Maslov seismograms, *J. Geophys.*, **58**, 27–43.

Chapman, C. H., Chu Jen-Yi & Lyness, D. G., 1988. The WKBJ seismogram algorithm, in *Seismological Algorithms*, pp. 47–74, ed. Doornbos, D. J., Academic Press, London.

Cummins, P. & Johnson, L., 1988. Synthetic seismograms for an inner core transition of finite thickness, *Geophys. J.*, **94**, 21–34.

Daley, P. F. & Hron, F., 1982. Ray–reflectivity method for SH waves in stacks of thick and thin layers, *Geophys. J. R. astr. Soc.*, **69**, 527–536.

Douglas, A., Hudson, J. A. & Blamey, C., 1973. A quantitative evaluation of seismic signals at teleseismic distances III—Computed *P* and Rayleigh wave seismograms, *Geophys. J. R. astr. Soc.*, **28**, 345–410.

Fuchs, K., 1968. The reflection of spherical waves from transition zones with arbitrary depth-dependent elastic moduli and density, *J. Phys. Earth*, **16**, 27–41.

Fuchs, K. & Müller, G., 1971. Computation of synthetic seismograms with the reflectivity method and comparison with observations, *Geophys. J. R. astr. Soc.*, **23**, 417–433.

Kennett, B. L. N., 1983. *Seismic Wave Propagation in Stratified Media*, Cambridge University Press, Cambridge.

Kennett, B. L. N., 1988. Systematic approximations to the seismic wavefields, in *Seismological Algorithms*, pp. 237–259, ed. Doornbos, D. J., Academic Press, London.

Kennett, B. L. N. & Illingworth, M. K., 1981. Seismic waves in a stratified halfspace—III. Piecewise smooth models, *J. geophys. Res.*, **66**, 663–675.

Konopásková, J. & Červený, V., 1984. Numerical modelling of time harmonic seismic wave fields in simple structures by the Gaussian beam method, Part I, *Studia geoph. et geod.*, **28**, 19–35, Part II, *Studia geoph. et geod.*, **28**, 113–128.

Müller, G., 1985. The reflectivity method: A tutorial, *J. geophys*, **58**, 153–174.

Ratnikova, L. I., 1973. *The Method of Seismic Wave Computation in Thinly Layered Media*, Nauka, Moscow (in Russian).

Richards, P. G. & Frasier, C. W., 1976. Scattering of elastic waves from depth dependent inhomogeneities, *Geophysics*, **41**, 441–458.

Scholte, J. G. J., 1962. Oblique propagation of waves in inhomogeneous media, *Geophys. J. R. astr. Soc.*, **7**, 244–261.

Töpferová, D. & Červený, V., 1987. Numerical modelling of seismic wave fields in models containing stacks of thin layers, *Studia geoph. et geod.*, **31**, 344–358.

INFLUENCE OF A NEAR-SURFACE STRUCTURE ON SEISMIC WAVE FIELDS RECORDED AT THE EARTH'S SURFACE

VLASTISLAV ČERVENÝ [1,2] and FERNANDO C.M. DE ANDRADE [2]

[1] *Institute of Geophysics, Charles University, Ke Karlovu 3, 121 16 Praha 2, Czechoslovakia.*
[2] *Instituto de Geociências, Universidade Federal da Bahia, Rua Caetano Moura 123, Federação, 40.210 Salvador, Bahia, Brasil.*

(Received October 3, 1991; revised version accepted October 30, 1991)

ABSTRACT

Červený, V. and de Andrade, F.C.M., 1992. Influence of a near-surface structure on seismic wave fields recorded at the earth's surface. *Journal of Seismic Exploration*, 1: 107-116.

The hybrid ray-reflectivity method is applied to the numerical modelling of seismic wave fields in laterally varying layered models containing a thin near-surface low-velocity layer. The computations within the laterally varying layered model are performed by the ray method, but the thin near-surface layer is attacked locally by the matrix methods. The thin layer need not be homogeneous, it may include arbitrary inner layering and it may vary slightly laterally. All multiples within the layer are automatically taken into account. Numerical examples of hybrid ray-reflectivity seismograms for two models of the thin near-surface layer are presented. An inverse algorithm to remove the effects of a thin near-surface layer from seismograms recorded at the earth's surface is proposed.

KEY WORDS: seismic waves, ray method, hybrid-ray reflectivity method, near-surface structure, multiple suppression

INTRODUCTION

Seismic wave fields recorded at the earth's surface are greatly influenced by the local structure close to the receiver. Commonly, the structure close to the

0963-0651/92/$5.00

receiver (meters or tens of meters in depth) is rather complex. In a near-surface thin layer, the velocities of propagation of seismic waves are usually very low, considerably lower than the velocities at greater depths. The structure of the near-surface thin layer plays an important role both in the numerical modelling of seismic wave fields and in the inversion of seismic data.

Within the thin near-surface layer, there are very favorable conditions for the generation of strong multiple reflections of a high multiplicity, as the surface of the earth and the bottom interface of the layer are very good reflectors, with strong velocity contrasts.

In the numerical modelling of seismic wave fields by the high-frequency methods (such as the ray method or the method of summation of Gaussian beams), any of the multiple reflections generated within the thin near-surface layer may easily be taken into account. However, if the number of multiples is high, such computations are cumbersome, particularly if the near-surface thin layer consists of several sublayers.

In this contribution, a hybrid ray-reflectivity method proposed by Červený (1989) is modified to perform such computations for models containing thin near-surface layers. The method automatically includes all multiples, including converted multiples. It can, however, be used only for thin near-surface layer, the thickness of which is roughly less than one half of the prevailing wavelength. Attempts have also been made to solve the opposite problem: to remove the effects of a near-surface thin layer from calculated (or observed) seismograms. Such 'clean' seismograms are required in many recent applications, particularly in the inversion of complete seismograms (Born inversion, etc.).

Note that the proposed algorithms can play an important role even in seismology, mainly in seismic microzoning. The near-surface geological structure has a great influence on an earthquake's effects on a given locality.

HYBRID RAY-REFLECTIVITY METHOD

The hybrid ray-reflectivity method has been designed to compute body wave synthetic seismograms in 2-D and 3-D laterally varying layered structures containing thin transition layers. A thin transition layer is not necessarily homogeneous; it may be represented by a stack of roughly parallel sublayers. The velocity, density and absorption contrasts between individual sublayers may be quite arbitrary (in the vertical direction). In the lateral direction, the velocities, densities and absorbing parameters within individual sublayers are also allowed to vary, but only smoothly. The thin transition layers may be

smoothly curved. The total thickness of a layer should not greatly exceed one half of the wavelength.

The hybrid ray-reflectivity method combines the ray and matrix calculations. The ray calcalutations are applied in the parts of the model where the rays are not in contact with the thin transition layer. On the contrary, the matrix methods are applied locally at the points of reflection (transmission) on the thin transition layer.

Programs for the calcalution of ray-syntethic seismograms can be modified to yield such hybrid computations. Assume that a single interface of the first order in the model is replaced by a thin transition layer. Then the reflection/transmission coefficient corresponding to the interface should be replaced by the reflection/transmission coefficient at the thin layer, calculated by matrix methods. Such a reflection transmission coefficient at a thin transition layer is, of course, frequency dependent. Thus, the modification consists, in fact, in an application of a frequency filter.

A program package designed for such hybrid computations in general 2-D laterally varying layered structures containing a thin transition layer was written and described in Červený (1989). For the matrix computation of frequency-dependent reflection/transmission coefficients, the routines written by Müller (1985) were used. The package was used to study the properties of PP reflected waves from thin transition layers of different types, see Červený (1989). In Červený and Aranha (1991), the method was applied to the problem of tunneling of the reflected wave field through a high-velocity stack of thin layers situated in the overburden of the reflector. Both these papers present an extensive literature related to these problems. To test the accuracy of the method, the hybrid ray-reflectivity synthetic seismograms were compared with the full reflectivity computations for 1-D models. It was found that the accuracy of the hybrid ray-reflectivity computations was quite sufficient for pratical purposes. The hybrid method is most successful in the case of a near-normal incidence of the wave on the thin layer. With an increasing angle of incidence, the accuracy may decrease.

HYBRID RAY-REFLECTIVITY METHOD FOR A STRUCTURE WITH A THIN NEAR-SURFACE LAYER

In this contribution, the hybrid ray-reflectivity method is modified to include a thin near-surface layer. Above the top boundary of the thin layer, a vacuum is assumed. The modification is as follows: In the ray method, the complex-valued amplitude of the wave incident on the earth's surface should be multiplied by the so-called conversion coefficients to obtain the horizontal and

vertical displacement components. If a thin near-surface layer is considered, it is necessary to compute the conversion coefficients corresponding to the wave incident on the bottom of the layer and the receiver situated on the top of the layer at the same lateral position. It is possible to show that such conversion coefficients can be expressed in terms of 'transmission' coefficients through a thin layer, corresponding to the transmitted wave passing formally into the vacuum. Such coefficients can be evaluated simply by matrix methods. In the algorithm, the upper boundary of the earth is replaced by the thin layer, and the standard conversion coefficients are replaced by the relevant conversion coefficients evaluated by matrix methods. In other words, the spectrum of each single event, computed by the ray method at the bottom of the near-surface layer, is multiplied by a scalar filter $F(i,\omega)$ corresponding to the ratio of the local conversion coefficients computed by the two methods,

$$F(i,\omega) = C(i,\omega) / C_o(i) \qquad (1)$$

Here $C(i,\omega)$ is the conversion coefficient corresponding to the thin near-surface layer, computed by the matrix method, $C_o(i)$ is the standard conversion coefficient for a free surface, ω is the frequency and i is the angle of incidence. There are four different scalar filters (1); they correspond to incident P- and S-waves and to recorded horizontal and vertical components. The filters, of course, depend on the local structure in the vicinity of the receiver.

REMOVING THE EFFECTS OF THE NEAR-SURFACE LAYER FROM SEISMOGRAMS

The scalar filter (1) can be inverted,

$$F^{-1}(i,\omega) = C_o(i) / C(i,\omega) . \qquad (2)$$

The application of (2) to the data calculated (or observed) on the top of the thin near-surface layer removes the effects of the near-surface layer. In greater detail: the filtered wave field corresponds to the receiver situated on the surface of the earth, situated in the place where the bottom of the thin layer was. The filter F^{-1}, of course, includes even the so-called static correction.

Such a scalar filter (2) may be applied to synthetic or to observed seismograms of individual single events. The main problem in the application of the procedure to the observed seismograms consists primarily in a decomposition of the seismogram into single P- and S-events and in an

inaccurate knowledge of the local structure and of the angles of incidence of individual events.It would be useful to transform the complete vertical- and horizontal- component seismograms into seismograms corresponding to incident P- and S-waves. After this, it would be possible to apply the inverse filters independently to P- and S-seismograms, considering some average angles of incidence. Both the transformation and inversion filters could, of course, be combined.

EXAMPLES

We will present here two simple examples of the application of the proposed algorithms.

In both examples, we consider a PP reflected wave from a horizontal interface, situated at a depth of 1 km below the surface of the earth. The P-wave velocities above and below the interface are: $\alpha_1 = 3$ km/s and $\alpha_2 = 5$ km/s, respectively. The S-wave velocities β and the densities ϱ are determined from α using the relations: $\beta = \alpha / \sqrt{3}$ and $\varrho = 1.7 + 0.2\,\alpha$. The absorption is not considered. An isotropic point source is situated close to the earth's surface; the interaction of the source with the surface is not taken into account. The source time function is represented by a Gabor signal

$$x(t) = \exp[-(2\pi f_M(t-t_0)/\gamma)^2]\cos[2\pi f_M(t-t_0)+v], \qquad (3)$$

where $f_M = 30$ Hz, $\gamma = 5$, $v = 0$, $t_0 = 0.043$ s. Here f_M represents a prevailing frequency, t_0 is a small time shift which is used to shift the time zero to the effective onset of the signal (Fig. 1).

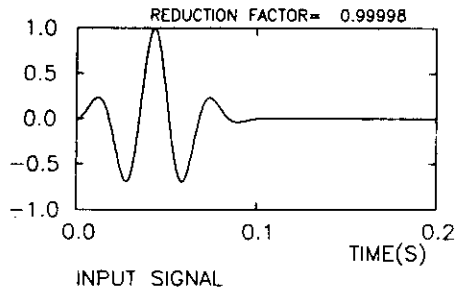

Fig. 1. The source time function used in examples.

The ray synthetic seismograms of the vertical component of the PP reflected wave for receivers situated along the earth's surface at offsets from 0.2 km to 2.5 km (with steps of 0.1 km) are shown in Fig. 2a. The critical distance for a given configuration equals 1.5 km; see the increase of amplitudes and non-zero phase changes immediately behind 1.5 km.

In the first example, we shall modify the global model described above by inserting a thin low-velocity layer of a constant thickness on its surface. We shall also place the receivers on the top of the thin layer. The total thickness of the layer is 20 m. The layer consists of two thin sublayers of 5 m and 15 m thicknesses, with the P-wave velocities of 0.7 km/s and 1.4 km/s, respectively. The S-wave velocities and the densities within the sublayers are determined from the P-velocities using the same relations as in the global model. The absorption inside the sublayers is assumed to be zero.

The synthetic seismograms of the vertical component of the P-wave are shown in Fig. 2b., displaying clear effects of multiple arrivals generated inside the thin layer. The greatest effects can be observed in the critical region. The time shift of the signal due to the thin near-surface layer is also clearly seen in Fig. 2b.

An attempt has been made to apply the inverse filter locally on the seismograms shown in Fig. 2b. The resulting seismograms from which the effects of the thin near-surface layer are removed, are shown in Fig 2c. If we compare the synthetic seismograms shown in Figs. 2a and 2c, we can see that they are practically the same. We can also see that the signals are shifted to a proper time position so that the inverse filter includes the static correction.

In the second example, we shall use the same global model of the structure. We shall, however, use a different thin low-velocity near-surface layer. The layer is homogeneous, with a P-wave velocity of 1.2 km/s, and with the S-wave velocity β and density ϱ determined using the same relations as in the global model. The thickness of the thin layer, however, varies linearly along the profile. It is 40 m at the first receiver and 0 m at the last receiver. The synthetic seismograms of PP reflected waves are shown in Fig. 3a. If we compare Fig. 2a and Fig. 3a, we can observe great changes at small offsets, with expressive multiples. As the offset gets larger, the differences between these seismograms are becoming smaller. We cannot see any difference at the last trace. We can also observe distinct differences in arrival times due to the variation of the thickness of the thin layer.

In addition, a random noise was introduced in the seismograms of Fig.3a, as shown in Fig. 3b. Applying the position-dependent inverse filter to these noisy seismograms, the removal of the effects of the thin near-surface layer is again excellent; compare Figs. 3c and 2a. Even the noise is partially suppressed.

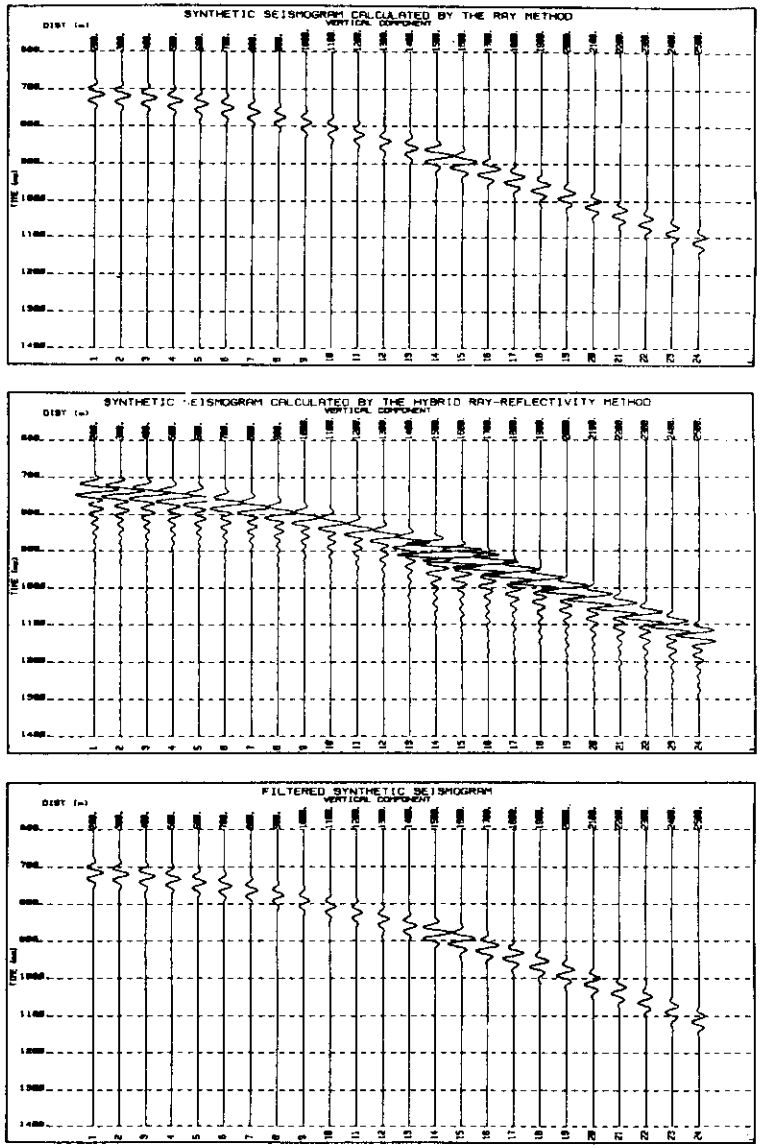

Fig. 2. Synthetic seismograms of a vertical component of a PP reflected wave from a reflector situated at a depth of 1 km. Fig. 2a: No thin low-velocity near-surface layer is considered. Fig. 2b: A thin low-velocity near-surface layer of a constant thickness is considered. Fig. 2c: An inverse filter is applied locally to the seismograms shown in Fig. 2b to remove the effects of the thin layer.

The reason why the removal of the near-surface structure effects in the two synthetic examples presented is so successful consists mainly in the simple form of the seismograms, corresponding to one single event only. Thus, the simple scalar filter (2) can be directly applied. Moreover, the structure and the angles of incidence have been perfectly known. If several different events, e.g., the reflections from different reflectors, arrive at the same detector, the removal of the near-surface effects would be more complicated. For a more detailed discussion and numerical examples of the application of the hybrid ray-reflectivity method and of the removal of the effects of the near-surface layer see Andrade (1991). The examples include the removal of the effects of the near-surface layer from P-reflection seismograms containing reflections from different non-planar reflectors situated in a complex laterally varying structure, the removal with an incorrectly known structure and incorrect angles of incidence, and even the effects of a near-surface layer on incident S-waves. The results are promising.

CONCLUSIONS

A hybrid ray-reflectivity algorithm can be used to compute the seismic wave fields in general 2-D and 3-D laterally varying layered structures containing a thin low-velocity near-surface layer. In an opposite way, the algorithm can be used to remove the effects of a such a thin layer from computed (or observed) seismograms.

Even though the examples presented here consider only a very simple global model, the algorithm and relevant program package can be used to compute synthetic seismograms for very general, 2-D laterally varying layered global models. A slight absorption in the global model is also allowed. Not only P- (as in the examples presented here) but also S- and converted waves propagating in such a model may be taken into account. The structure within the thin layer may also be very complex, with an arbitrary number of sublayers of arbitrary contrasts of velocities, densities and absorption parameters.

As follows from many other computed examples, the influence of a thin low-velocity near-surface layer on S-waves is, as a rule, considerably greater than on P-waves.

Here we have considered only a low-velocity thin layer. The algorithm used can also consider the near-surface high-velocity layers, e.g., permafrost layers. In such a case, the hybrid algorithm will automatically include even certain important non-ray effects, such as the inhomogeneous waves behind the critical angle of incidence on the near-surface layer.

a

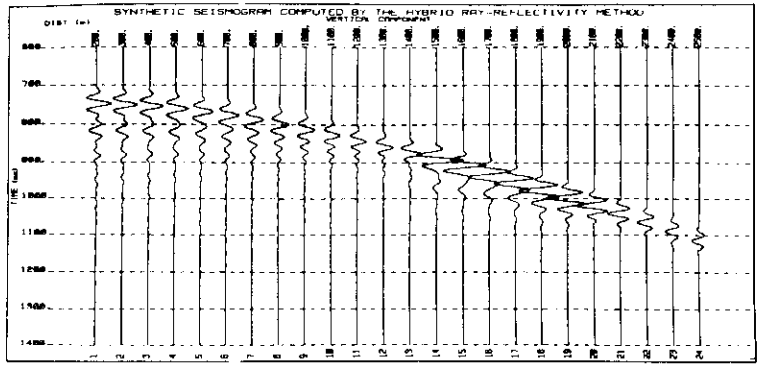

b

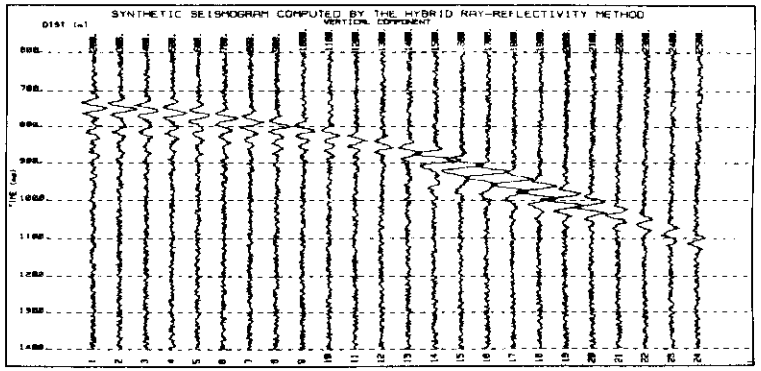

c

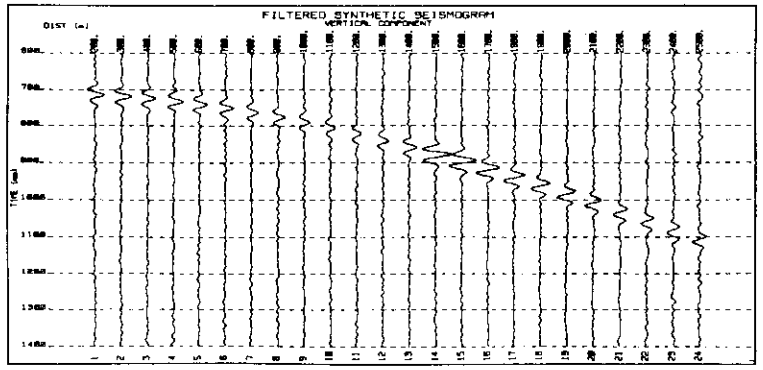

Fig. 3. Synthetic seismograms of a vertical component of a PP reflected wave for the same global model as in Fig. 2. Fig. 3a: A thin low-velocity near-surface layer of a variable thickness is considered. Fig. 3b: Random noise is added to the seismograms shown in Fig. 3a. Fig. 3c: An inverse filter is applied locally to the seismograms shown in Fig. 3b to remove the thin-layer effects.

ACKNOWLEDGEMENTS

This work was done during the first author's stay at the Federal University of Bahia, Salvador. The research was sponsored by the CNPq, FINEP, PETROBRAS and by the IBM Academic Initiative in Czechoslovakia.

REFERENCES

de Andrade, F.C.M., 1991. Influência de camadas finas superficiais nos dados sísmicos gravados na superfície. Dissertação de Mestrado. PPPG/UFBa, Univ. Federal da Bahia. To be published.

Červený, V., 1989. Synthetic body wave seismograms for laterally varying media containing thin transition layers. Geophys. J. Int., 99: 331-349.

Červený, V. and Aranha, P.R.A., 1991. Tunelling of seismic body waves through thin high-velocity layers in complex structures. Studia geoph. et geod., submitted.

Müller, G., 1985. The reflectivity method: A tutorial. J. Geophys., 58: 153-174.

TUNNELING OF SEISMIC BODY WAVES THROUGH THIN HIGH-VELOCITY LAYERS IN COMPLEX STRUCTURES

VLASTISLAV ČERVENÝ

Institute of Geophysics, Charles University, Prague)*

PAULO R. A. ARANHA

*Instituto de Geociencias, Universidade Federal da Bahia, Salvador**)*

Summary: *The hybrid ray-reflectivity method is applied to the problem of the transmission of the reflected wave field through a thin high-velocity layer (or through a thin stack of high velocity layers), situated in the overburden of the reflector. In the hybrid ray-reflectivity method, the standard ray method is applied in the smooth parts of the model, and the reflectivity method is used locally at the thin high-velocity layer. With the exception of small epicentral distances, the standard ray method itself fails in such computations. The reason is that a considerable part of the energy for overcritical angles of incidence may be tunneled through the thin high-velocity layer along complex ray-paths, corresponding to inhomogeneous waves. The reflectivity method, applied locally at the thin high-velocity layer, automatically includes all inhomogeneous wave contributions. Thus, the hybrid ray-reflectivity method removes fully the limitations of the standard ray method, but still retains its main advantages, such as its applicability to 2-D and 3-D complex layered structures, flexibility, and low-cost computations. In the numerical examples, the hybrid ray-reflectivity synthetic seismograms are compared with standard ray synthetic seismograms and with full reflectivity computations. The numerical examples show that the hybrid ray-reflectivity method describes the tunneling of seismic energy through a thin high-velocity layer with sufficient accuracy.*

1. INTRODUCTION

The hybrid ray-reflectivity method can be used to compute body wave synthetic seismograms in 2-D and 3-D laterally varying layered structures containing thin transition layers, see [10]. By a thin transition layer we understand a layer the thickness of which is roughly 1/2 or less of the prevailing wavelength. In the hybrid ray-reflectivity method, ray calculations are applied to those parts of the model which do not contain the thin high-velocity layers and which are assumed to be smooth. On the contrary, matrix (reflectivity) computations are applied locally to the thin transition layers. The BEAM87 program package, designed for such hybrid computations in 2-D laterally varying layered structures containing a thin transition layer, was described in [10]. The method and the program package were used there to study the P waves reflected from a thin transition layer separating two halfspaces.

In this paper, we apply the hybrid ray-reflectivity method also to reflected P waves, but in a more general configuration. We will not compute the waves reflected from a thin transition layer, but passing through a thin high-velocity layer. The waves are reflected from a single structural first-order interface, and the thin high-velocity layer is situated in the overburden. The thin high-velocity layer is not necessarily homogeneous; it may be represented by a stack of very thin homogeneous layers. It is well known that the standard ray method is not able to treat such a problem, with the exception of small epicentral distances. An important role in

*) Address: Ke Karlovu 3, 121 16 Praha 2.

**) Address: Campus Universitário de Federação, 40210 Salvador, Bahia, Brasil.

the transmission of the seismic energy through the thin high-velocity layer is played by inhomogeneous waves. The inhomogeneous waves do not propagate through the thin layer along real-valued rays, but along complex-valued ray-paths. As the contribution of inhomogeneous waves to the transmission of energy through a thin high-velocity layer may be rather high, the standard ray method itself fails in such computations [23, 9]. Fuchs and Schulz [23] speak of tunneling of seismic energy through the thin layer. These effects are frequency-dependent, the tunneling is stronger for lower frequencies. The hybrid ray-reflectivity method automatically includes all inhomogeneous waves propagating through the thin layer, since the reflectivity algorithm includes them [30]. Thus, the hybrid ray-reflectivity method removes fully this serious limitation of the standard ray method.

In the algorithm of the hybrid ray-reflectivity method, only the ray method in its zero-order approximation is used. The zero-order approximation of the ray method is fully based on the concept of real rays. It is used in many of the computer algorithms and program packages. To simplify the terminology, we speak of the standard ray method. It would, of course, be possible to generalize it by using certain higher-order waves (head waves, etc.). Moreover, it would also be possible to consider complex rays (in addition to real rays). From a theoretical point of view, there is no fundamental problem in the generalization for complex rays [2, 5, 12, 18, 26, 27, 34]. Complex rays have even been used successfully in applications, see, e.g. [25, 33]. The above list is far from complete; many other important references can be found in the papers given above.

However, we have no intention of proposing an algorithm and developing a computer package for the numerical modelling of seismic wave fields using complex rays here. Just the opposite. We merely wish to show that the hybrid ray-reflectivity method can be used to solve certain problem, which involve complex rays, without difficulties.

Various alternatives of the hybrid method used in this paper have been described in the seismological literature. They are designed mostly for one-dimensional computations only [16, 32]. The hybrid ray-reflectivity code proposed by Bernasconi and Drufuca [6] can even be used for a non-horizontal stack of layers. Some of the hybrid methods use the WKBJ method instead of ray computations [1, 15]. Also the method of summation of Gaussian beams can be used instead of the standard ray method [10]. Another hybrid method was proposed for models with localized heterogeneities. It uses finite differences in a heterogeneous region and the frequency-wavenumber method outside the region [19]. The ray method can also be efficiently combined with modal summation. However, we do not intend to review here all the used or possible hybrid methods in the numerical modelling of seismic wave fields; we only wish to say that the hybrid codes are very promissing.

To avoid a terminological misunderstanding, it would be useful to add one remark. In the hybrid ray-reflectivity method, by the reflectivity method we understand just matrix computations of frequency-dependent plane-wave reflection/transmission coefficients of a stack of thin layers, for a given angle of incidence. We do not perform any integration over angles of incidence as in the full reflectivity method [22, 30]. Thus, it would perhaps be more suitable to speak about the hybrid ray-matrix method, not about the hybrid ray-reflectivity method. We will, however, follow the terminology introduced in the seismological literature [16]. Only in the Gaussian beam summation method and, consequently, in the hybrid Gaussian beam-reflectivity method, some sort of integration (summation) over angles of incidence is performed.

In Section 2, we will briefly discuss the problem of the transmission of reflected waves through a thin high-velocity layer. In Section 3, we will present several numerical examples and discuss the results from a seismological point of view. In all cases, we will compare the ray synthetic seismograms with hybrid ray-reflectivity synthetic seismograms. To assess the accuracy of the hybrid ray-reflectivity seismograms, we will compare them with the full reflectivity method computations for one simple 1-D model.

2. TUNNELING EFFECTS IN MEDIA CONTAINING THIN HIGH-VELOCITY LAYERS

Before we present and discuss the results of numerical computation, we will briefly describe several important properties of homogeneous and inhomogeneous, reflected and transmitted waves propagating in layered structures. This will help us to understand better the results of numerical computations. We will mainly concentrate our attention on the role of inhomogeneous waves in the transmission of energy of seismic waves through a thin high-velocity layer. See also [3, 4, 7, 13, 14, 20, 21, 34].

Homogeneous and inhomogeneous reflected and transmitted waves at a single interface

We consider a plane interface between two homogeneous halfspaces, and a point source of seismic waves situated in one of these halfspaces. We call the halfspace containing the source the first (or the upper) halfspace, and the halfspace without the source the second (or the bottom) halfspace. We denote the compressional and shear velocities in the first halfspace by α_1, β_1, and in the second halfspace by α_2, β_2. We assume that $\alpha_2 > \alpha_1$.

Let us consider compressional incident, reflected and transmitted waves. We introduce the critical angle i_1^* in a standard way,

$$\sin i_1^* = \alpha_1/\alpha_2 . \tag{1}$$

For a subcritical angle of incidence ($i_1 < i_1^*$), the angle of transmission is real-valued and a standard transmitted ray-theory wave, with a real-valued ray, is obtained. For an overcritical angle of incidence, however, the angle of transmission is complex-valued. The corresponding transmitted wave cannot be studied by the standard ray method. We call such a wave a transmitted inhomogeneous wave.

The properties of inhomogeneous waves are well known from the seismological literature, see [7, 31] for the acoustic case and [8] for the elastic case. The most important property of time-harmonic inhomogeneous waves is that their amplitudes decrease exponentially with increasing distance from the interface. The exponential decrease of amplitudes is frequency dependent: for higher frequencies it is faster and for lower frequencies slower.

In contrast to the transmitted waves, the rays of reflected compressional waves are always real-valued, for any real-valued angle of incidence of a compressional incident wave. However, the critical angle still plays an important role even for reflected waves. We will explain this role from the point of view of the standard ray approximation. In the subcritical region ($i_1 < i_1^*$), the amplitudes of reflected waves are usually small. The amplitudes increase rapidly as the angle of incidence i_1 approaches the critical angle, $i_1 \to i_1^*$. At the critical angle of incidence, the amplitudes of the reflected waves reach their maximum. Beyond the critical angle, the amplitudes

are large, and decrease slowly with increasing epicentral distance. The reflection coefficients are real-valued for subcritical angles of incidence, but complex-valued for overcritical angles of incidence. This implies that the shape of the wavelet of the reflected wave is the same as the shape of the wavelet of the incident wave for subcritical angles of incidence. For overcritical angles of incidence, however, the shape of the wavelet of the reflected wave is different from the shape of the wavelet of the incident wave. All these conclusions are only approximate, and valid only in the approximation of the standard ray method. Exact computations yield some well-known differences, namely in the region close to the critical point. In exact computations, the maximum of the amplitude-distance curve of the compressional reflected wave is shifted from the critical point to some distance beyond the critical point. The shift is frequency-dependent, it is small for high frequencies. In addition to the reflected waves, classical head waves are also obtained in the overcritical region. (The head wave is not obtained by the standard ray method, but can also be evaluated by the higher approximation of the ray method.)

Let us add one note to inhomogeneous waves. Consider an inhomogeneous transmitted wave generated by a regular incident wave (with a real-valued ray element between the source and the interface). If we exchange the source and the receiver and use the principle of reciprocity, we obtain waves which propagate as inhomogeneous from the source to the interface and then along a regular ray from the interface to the receiver. Such waves were also described and discussed in the references given above. They were even experimentally verified in seismic laboratory modelling, using a schlieren technique. See [11], where these waves are called pseudospherical waves. At present, such waves are also called "star" waves (P^*, S^*), see [17]. The inhomogeneous waves propagating from the P-wave point source may also generate regular S waves. Recently, certain S^* waves attracted the attention of seismologists, namely the S^* wave generated at the Earth's surface by a P-wave source situated close to the Earth's surface [4, 5, 21, 24].

Transmission through a thin high-velocity layer

We will first discuss the compressional wave transmitted through the thin layer, without any multiple reflections within the layer. Assume that the P velocities in the upper halfspace and in the bottom halfspace are the same, α_1. Also assume that the velocity α_2 in the thin layer separating these two halfspace is higher, $\alpha_2 > \alpha_1$. We consider two cases of incidence: the subcritical angle of incidence ($i_1 < i_1^*$) and the overcritical angle of incidence ($i_1 > i_1^*$). The critical angle of incidence i_1^* is given by (1). The situation is simple for subcritical angles of incidence, see Fig. 1a. The wave propagates through the thin layer along a real-valued ray; the angle between the ray and normal to the interfaces inside the thin layer is given by Snell's law,

$$\frac{\sin i_2}{\alpha_2} = \frac{\sin i_1}{\alpha_1}. \tag{2}$$

For the overcritical angle of incidence, the transmission has a more complicated character. Only an inhomogeneous wave propagates within the thin layer, see Fig. 1b. The inhomogeneous wave, however, changes again into a regular transmitted

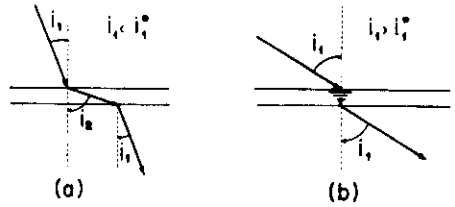

Fig. 1. A schematic explanation of the transmission of a P wave through a thin high-velocity layer. (a) Subcritical angle of incidence i_1. (b) Overcritical angle of incidence i_1: Tunnel wave.

wave in the bottom halfspace. This is obvious, as Snell's law must be valid at both the upper and lower interfaces of the thin layer; no matter whether the angles are complex or real-valued. Thus, the angle of transmission below the thin layer is again i_1. Even though the transmitted wave below the thin layer again propagates along a real-valued ray, it has different properties than the transmitted wave corresponding to the subcritical angle of incidence. It does not propagate along a real-valued ray through the thin layer. We also speak of the tunneling effect and tunnel wave, see Fuchs and Schulz [23]. This type of wave, of course, cannot be calculated by the standard ray method. The amplitude of the transmitted time-harmonic wave for an overcritical angle of incidence (tunnel wave) depends considerably on h/λ, where h is the thickness of the thin layer, and λ is the prevailing wavelength within the layer. The larger h/λ, the smaller the amplitude; the amplitude decreases exponentially with increasing h/λ. For small h/λ (say, $h/\lambda < 0{\cdot}5$), the amplitude of the transmitted wave may be rather distinct.

As the amplitudes of the transmitted waves depend on h/λ, i.e. on frequency, the thin transition layer acts as a low-pass filter at overcritical distances: the lower frequencies propagate easily through the thin layer, but the high frequencies will be mostly filtered out.

Let us emphasize one important point. The above discussion indicates that the angle of transmission i_1 in the bottom halfspace cannot exceed the critical angle i_1^* if the standard ray method is used for computation. A real-valued angle of transmission greater than i_1 in the lower halfspace can be obtained only if some more sophisticated method is used for computation, in which the inhomogeneous wave propagating within the thin layer is taken into account. As the standard ray method does not consider inhomogeneous waves, angle i_1 in the lower halfspace never exceeds i_1^* in the ray computations. Thus, the angles $i_1 > i_1^*$ are screened by the thin high-velocity layer in ray computation. We can also speak of angular filtering by a thin high velocity layer in the standard ray method.

If also shear waves are considered, several different inhomogeneous waves can carry energy through the thin layer. The discussion of such cases, however, is straightforward. The situation is considerably worse if an inner layering inside the thin layer is considered (laminas, etc.). Many multiple reflections, including converted waves, have to be taken into account. It would be impossible, or at least numerically inefficient, to consider all these elementary rays in ray computations. Thus, we have at least two reasons for combining locally the standard ray method with the reflectively method. The reflectivity method automatically yields all multiple reflections and conversions within the thin layer. In addition, it also yields all inhomogeneous waves, which cannot be evaluated by the standard ray method at all.

Effects of a thin high-velocity layer in the overburden on amplitudes of waves reflected from a first-order interface

The model under consideration is shown in Fig. 2a. We are interested in waves reflected from the bottom reflector, see Fig. 2b. The *P*-wave velocity below the reflecting interface is again α_2, and in the overburden α_1, with $\alpha_1 < \alpha_2$. We, however, assume that a thin layer with velocity $\alpha_3 \geqq \alpha_2 > \alpha_1$ is situated in the overburden.

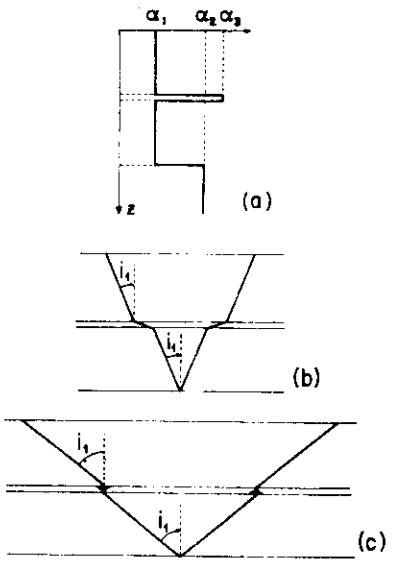

Fig. 2. A schematic explanation of the transmission of a *P* reflected wave through a thin high-velocity layer situated in the overburden. (a) Velocity depth distribution. (b) Subcritical angle of incidence at the thin high-velocity layer. (c) Overcritical angle of incidence at the thin high-velocity layer: Tunneling of energy through the thin high-velocity layer.

The wave field of the wave reflected from the bottom halfspace will obviously be considerably influenced by the high-velocity thin layer.

If we use the standard ray method for the computation (and do not consider inhomogeneous waves), the amplitude-distance curve of the reflected wave differs considerably from the amplitude-distance curve calculated for a model without the thin transition layer. The main reason for this difference is a follows. As discussed above, the amplitudes of reflected waves are small in the subcritical region ($i_1 < i_1^*$) and large in the critical and overcritical region ($i_1 > i_1^*$), where i_1^* is given by (1). If $\alpha_3 \geqq \alpha_2$, no rays with angles i_1 close to i_1^* penetrate through the thin layer; such rays are screened by the thin high-velocity layer. Only rays with angles i_1 satisfying the relation $\sin i_1 < \alpha_1/\alpha_3$ penetrate below the thin layer and strike the bottom reflector. Thus, the critical region related to the reflector with strong amplitudes is completely suppressed by these computations. The calculated amplitudes are, in general, considerably weaker than in a model without the thin layer (as reflected waves correspond only to subcritical reflections). This effect is, however, fully due to the inaccuracy of the standard ray method, i.e. due to its inability to consider inhomogeneous waves. Actually, the inhomogeneous waves carry most of the energy through the thin layer in this case. If we do not use the standard ray method, but some other more sophisticated method which includes computations of inhomogeneous waves, the situation is quite different. For thin transition layers (small h/λ) sufficient seismic energy is tunneled through the thin layer, even for angles of incidence i_1 with $\sin i_1 > \alpha_1/\alpha_3$, see Fig. 2c. We then obtain strong critical reflections from the bottom interface, even though regular rays with angles i_1 close to i_1^* do not penetrate through the layer. The differences between the reflected wave fields computed by the ray method and by any more sophisticated method (e.g., by the hybrid ray-reflectivity method) are very dramatic in this case. Numerical examples will be presented in the next section.

For a detailed discussion of the effects of a thin high-velocity layer on the reflected wave field see [23, 29]. Fuchs and Schulz [23] presented interesting example of synthetic seismograms for models containing a high-velocity layer, computes by the reflectivity method. The paper also gives many other references related to the effects of a high-velocity layer, both theoretical and observational.

3. NUMERICAL EXAMPLES

In this section, we will study numerically the effects of a thin high-velocity layer, situated in the overburden, on amplitudes and seismograms of reflected *P* waves. The hybrid ray-reflectivity method will be used for computations. The results will be compared with standard ray theory computations and with full reflectivity method computations.

The numerical examples were computed using the BEAM87 program package, described in [10]. The program package is designed for hybrid ray-reflectivity

computations in general 2-D laterally varying layered structures, containing a thin transition layer. Instead of the standard ray method, the Gaussian beam summation method can also be optionally used in combination with the reflectivity method. The model may contain isolated bodies, blocks, fractures and pinchouts. The structure within the thin layer is simulated by a system of very thin layers; the velocities and densities in these layers may be arbitrary. Thus, the thin transition layer may represent a laminated layer, a high-velocity layer, an actual transition region with a high gradient of velocity, etc. The thin layer may be smoothly curved and the structure within the thin layer may also slightly vary laterally. Slight absorption can also be considered.

A point source may be situated at any point of the medium, with the exception of the thin layer. Various radiation patterns and source-time functions may be considered. In our computations, we will use isotropic radiation patterns, and a source-time function representing a Gabor signal,

$$x(t) = \exp\{-(2\pi f_m(t - t_0)/\gamma)^2\} \cos(2\pi f_m(t - t_0) + \delta), \quad (3)$$

with $f_m = 5$ Hz, $\gamma = 4$, $t_0 = 0{\cdot}4$ s and $\delta = 0$. Note that f_m has the meaning of the prevailing frequency.

We will present three examples of computations. In the first one, the model is one-dimensional, and the thin layer represents a homogeneous high-velocity layer. In the second example, the thin high-velocity layer has a laminated character. In the third example, a 2-D laterally varying structure is considered. The reflecting interface is dipping and the thin layer is curved. The velocity distribution within the individual layers varies both vertically and laterally.

Thin homogeneous high-velocity layer

The first model is very simple. It consists of one homogeneous layer, bounded by the plane surface of the Earth at the top, and overlaying a homogeneous halfspace at the bottom. The bottom interface (reflector) is placed at a depth of 4·0 km and is horizontal. The P and S velocities and densities in the layer are $\alpha = 1{\cdot}5$ km/s, $\beta = 0{\cdot}87$ km/s, $\varrho = 2\,000$ kg m^{-3}, and in the halfspace $\alpha = 2{\cdot}9$ km/s, $\beta = 1{\cdot}15$ km/s, $\varrho = 2\,100$ kg m^{-3}. The P-wave point source with an isotropic radiation pattern is situated close to the Earth's surface. The interaction of the source with the Earth's surface is not taken into account. The source-time function is given by (3).

Four alternative computations are performed. In the first version, no thin high-velocity layer is considered, and the standard ray method is used for computation. The ray diagram of the P waves reflected from the reflector is then very simple, see

Fig. 3. Ray diagrams of a P wave reflected from a single interface. (a) No thin high-velocity layer is situated in the overburden. (The bold line at a depth of 2·0 km has only a formal meaning, the interface is fictitious). (b) A thin homogeneous high-velocity layer is situated in the overburden. Standard ray computations. (c) A thin homogeneous high-velocity layer is situated in the overburden. Hybrid ray-reflectivity computations. Note the great difference between (b) and (c).

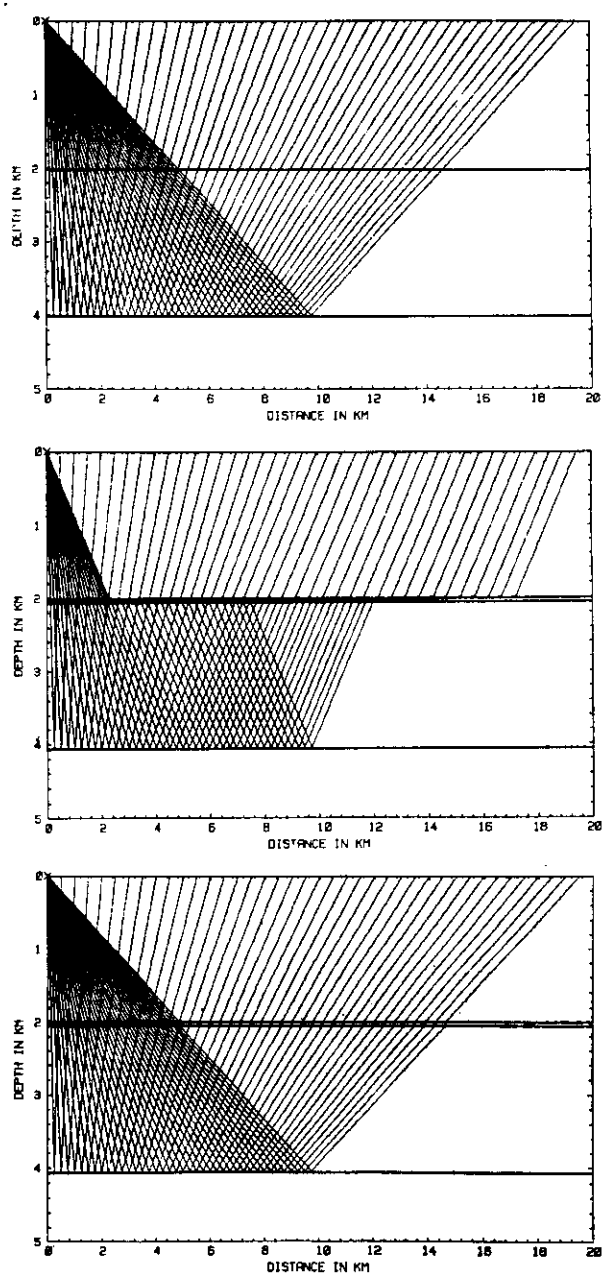

Fig. 3a. The bold horizontal line at a depth of 2·0 km does not represent any interface; it merely indicates where a thin high-velocity layer will be inserted in the next three versions.

In the second, third and fourth versions, a thin high-velocity layer, 0·05 km thick, is inserted into the overburden, at depths between 2·0 and 2·05 km. The reflector is then also shifted from 4·0 to 4·05 km. The P and S velocities and density within the thin layer are $\alpha = 2{\cdot}0$ km/s, $\beta = 1{\cdot}15$ km/s, $\varrho = 2100$ kg m^{-3}. Thus, the medium parameters within the thin layer are exactly the same as in the halfspace below the reflector. Note that the ratio of the thickness of the layer to the prevailing wavelength is 0·125. This number indicates that the hybrid ray-reflectivity method can be applied.

In the second version, the standard ray method is again used for computations, but in a model containing the thin high-velocity layer. The relevant ray diagram is shown in Fig. 3b. As we can see in the figure, the thin high-velocity layer influences the ray diagram considerably. For larger epicentral distances, the ray elements within the thin layer are very close to horizontal. The angle of incidence at the reflector is less than the relevant critical angle, at all epicentral distances. It is obvious that this behaviour of the ray diagram will influence considerably the synthetic seismograms of waves reflected from the reflector situated at a depth of 4·05 km.

In the third version, the hybrid ray-reflectivity method is used for computations, again in the model containing the thin high-velocity layer. The relevant ray diagram is shown in Fig. 3c. The transmission through the thin high-velocity layer is locally evaluated by the reflectivity method. To express this fact graphically in Fig. 3c, normal lines to interfaces are plotted instead of rays through the thin layer; they connect the ray elements which would form the ray if the thin high-velocity layer were removed. They also indicate the tunneling of the inhomogeneous waves through the thin layer.

In the fourth version, the full reflectivity method [22, 30] is used for the computation. The reflectivity zone extends from a depth of 2 km to 4·05 km and contains both the high-velocity layer and the bottom reflector. Thus, the reflectivity code yields not only the waves reflected from the bottom interface at a depth of 4·05 km but also the reflections from the thin high-velocity layer at depths of 2 – 2·05 km, and the relevant converted waves.

The relevant synthetic seismograms corresponding to the discussed four versions are presented in Figs. 4a, b, c, d. Let us first briefly explain Figs. 4a, b, c, showing synthetic seismograms of the P waves reflected from the bottom interface. Fig. 4a shows the ray synthetic seismograms for the model without the thin high-velocity layer (see Fig. 3a); Fig. 4b the ray synthetic seismograms for the model with the thin high-velocity layer (see Fig. 3b), and Fig. 4c the hybrid ray-reflectivity seismograms for a model with the thin high-velocity layer (see Fig. 3c). In Figs. 4a, b, c, the relevant head waves generated at the bottom reflector and the waves reflected from the thin high-velocity layer are not computed. Moreover, only simple transmissions through the thin layer are taken into account in Fig. 4b; multiple reflections inside the thin layer and under it are not considered. Finally, the reflectivity method computations for a reflectivity zone extending from a depth of 2·0 km to 4·05 km are shown in Fig. 4d. All multiple reflections, converted, inhomogeneous and head waves, etc., are automatically included in these computations.

In all synthetic seismograms, the time axis is oriented down (as is common in seismic prospecting), and the time is shown in milliseconds. The receivers are distributed regularly along the Earth's surface, with a spacing of 0·5 km. The traces are numbered: number 1 corresponds to an epicentral distance of 1·0 km. Thus, the n-th trace corresponds to an epicentral distance of $(n + 1)/2$ km.

Figure 4a displays the well-known ray theory properties of P waves reflected from a plane reflector. The strongest reflections are obtained close to the critical point which is situated at an epicentral distance of 9·07 km (close to the trace 18). At small epicentral distances the amplitudes gradually decrease with increasing epicentral distance and have a minimum at an epicentral distance of 4·5 km. After this, they increase and reach a maximum at the critical distance, and again slowly decrease. Amplitudes are sufficiently strong in the whole range of epicentral distances under consideration. The shape of the signal changes beyond the critical point. (Head waves were not considered in these computations.)

The ray synthetic seismograms for the same P reflected wave, but in a model with a thin high-velocity layer in the overburden, are shown in Fig. 4b. The ray theory computations now yield a quite different picture. They agree roughly with the computations presented in Fig. 4a only with traces 1 – 14, i.e. for epicentral distances of less than 7·5 km. The relevant angle of incidence is about 40°. Thereafter, the amplitudes remain practically constant at several traces (or slighty increase), but then they decrease radically. They practically vanish at traces 20 – 21, corresponding to an epicentral distance of about 10·5 – 11 km. The critical region with its strong amplitudes and phase changes has been removed completely. Note that the critical angle equals 41·8°.

The hybrid ray-reflectivity computations are shown in Fig. 4c. At small epicentral distances (at first 14 traces) they agree fully with the previous results shown in Figs. 4a and 4b. This means that the thin high-velocity layer has practically had no influence on the amplitudes of the waves reflected from the bottom reflector, even though the wave has been transmitted twice through it (up-down and down-up). This is, of course, valid only for small angles of incidence and for a very thin layer. For larger epicentral distances, the hybrid ray-reflectivity computations yield all critical region effects. The decrease of the amplitudes beyond the critical region is, however, faster than in the model without the thin layer. Moreover, it can be observed that the high frequencies are gradually filtered out. However, these effects are not very pronounced in Fig. 4c as the thickness of the thin high-velocity layer is small, and the Gabor signal under consideration has a very narrow-band amplitude spectrum. They are more pronounced in the computations with a high-

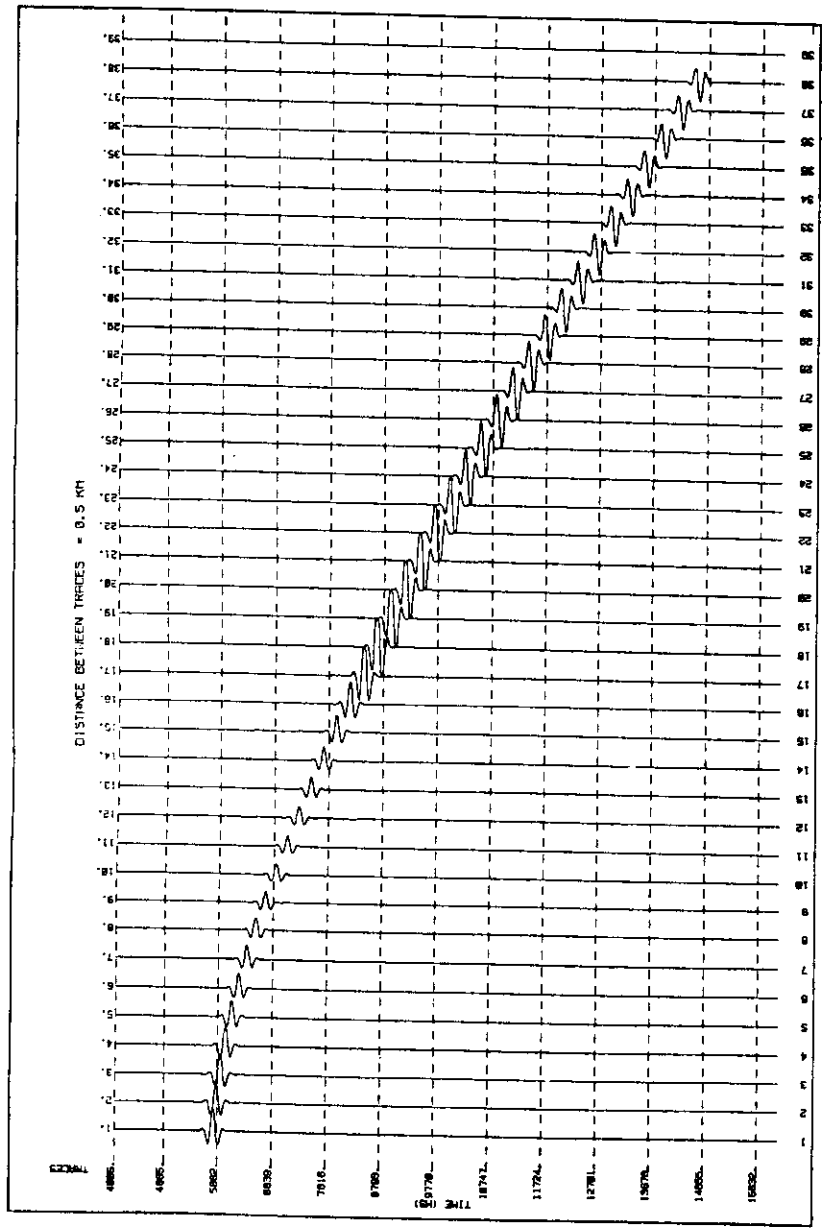
DISTANCE BETWEEN TRACES = 0.5 KM
TIME (SEC)

Fig. 4a

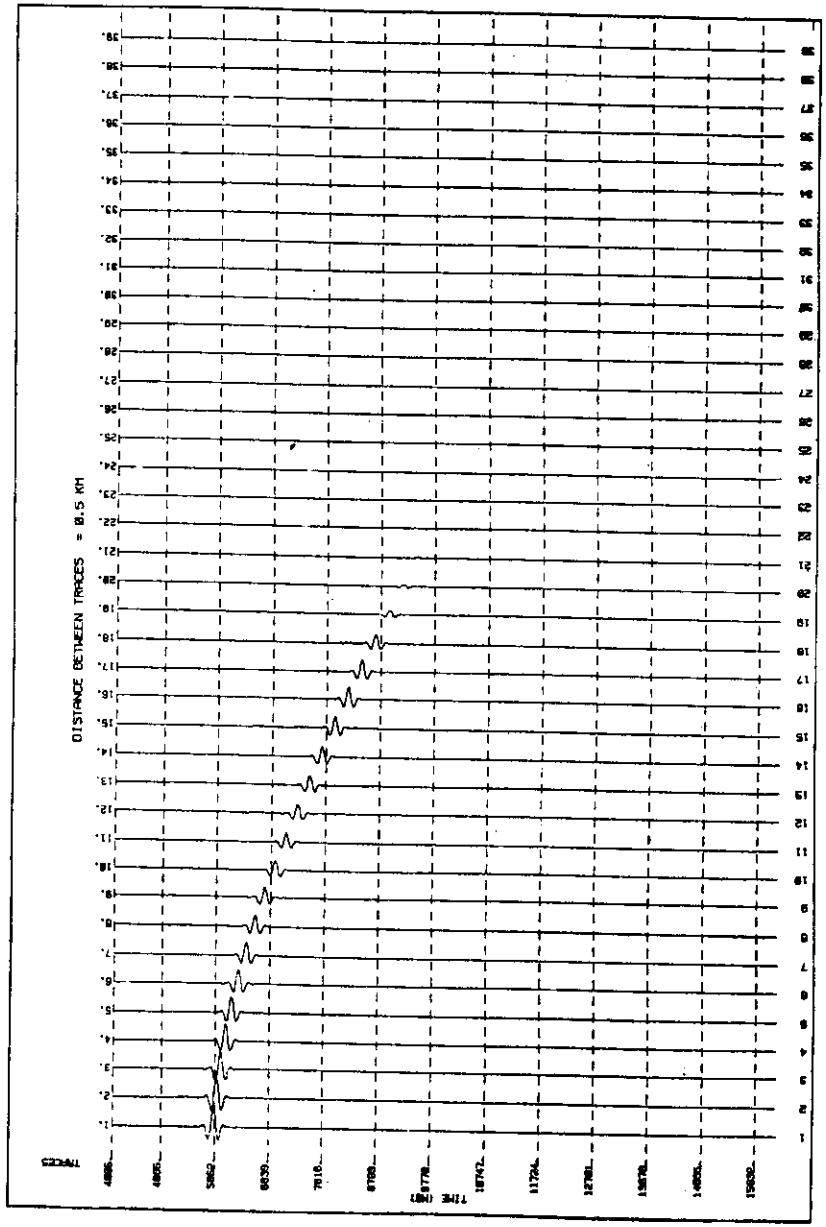
DISTANCE BETWEEN TRACES = 0.5 KM
TIME (SEC)

Fig. 4b

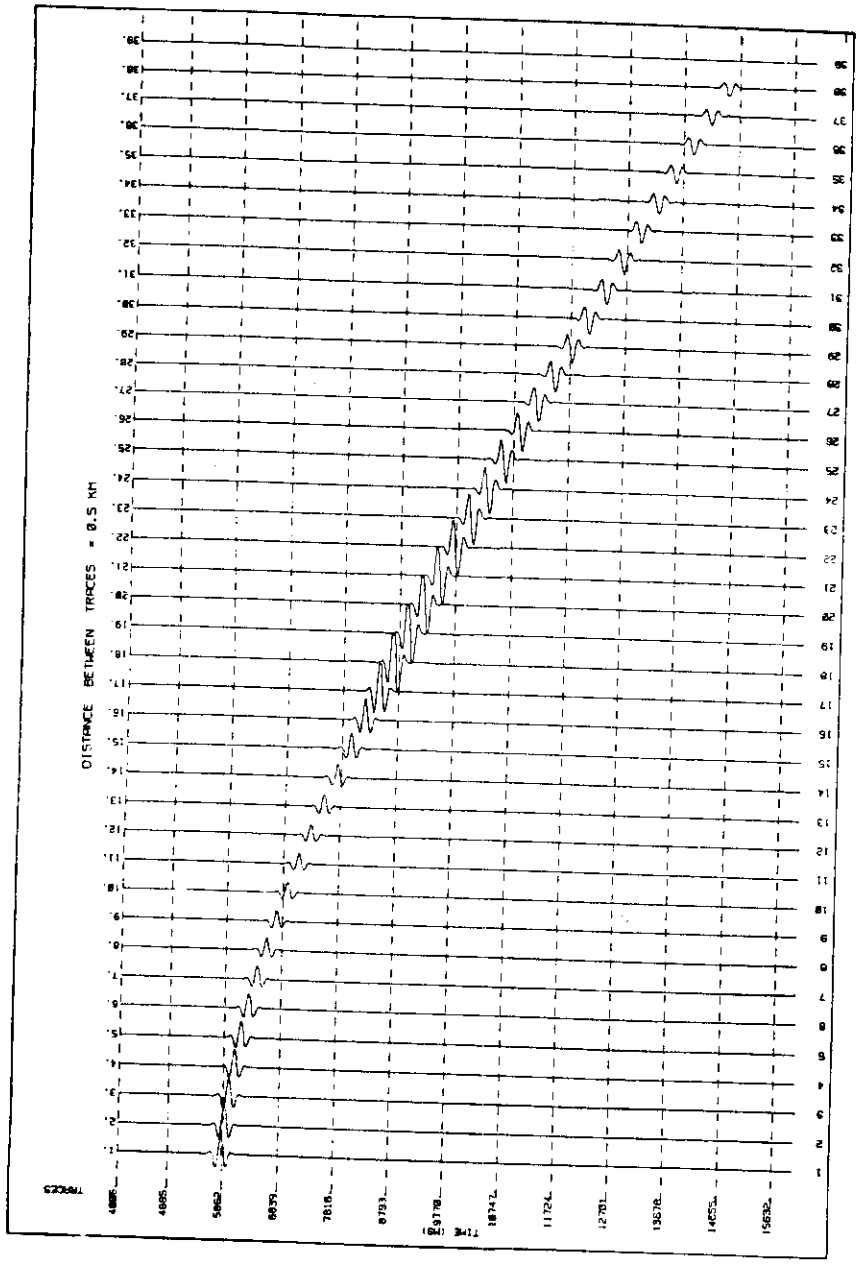

Fig. 4c

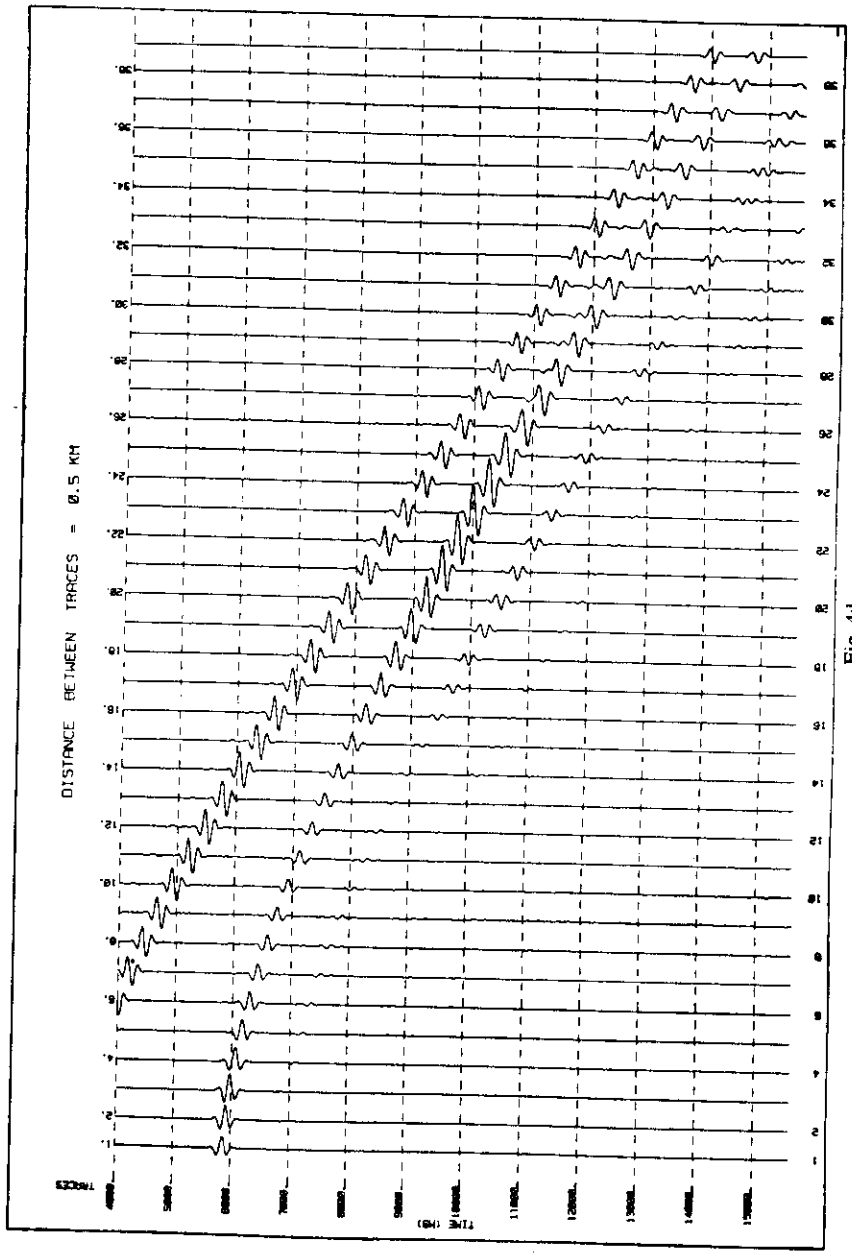

Fig. 4d

Fig. 4. Synthetic seismograms of P waves reflected from the bottom reflector for the models shown in Fig. 3. (a) Ray synthetic seismograms for the model without a thin high-velocity layer, see Fig. 3a. (b) Ray synthetic seismograms for the model with a thin high-velocity layer, see Fig. 3b. (c) Hybrid ray-reflectivity synthetic seismograms for the model with a thin high-velocity layer, see Fig. 3c. Note the great difference between (b) and (c). (d) The full reflectivity synthetic seismograms. The first distinct wave corresponds to the wave reflected from the thin high-velocity layer, the second to the wave reflected from the bottom reflector, and the last, weaker waves to the converted waves. A comparison of (c) and (d) shows that the hybrid ray-reflectivity method describes well the tunneling of seismic energy through the thin high-velocity layer at overcritical distances.

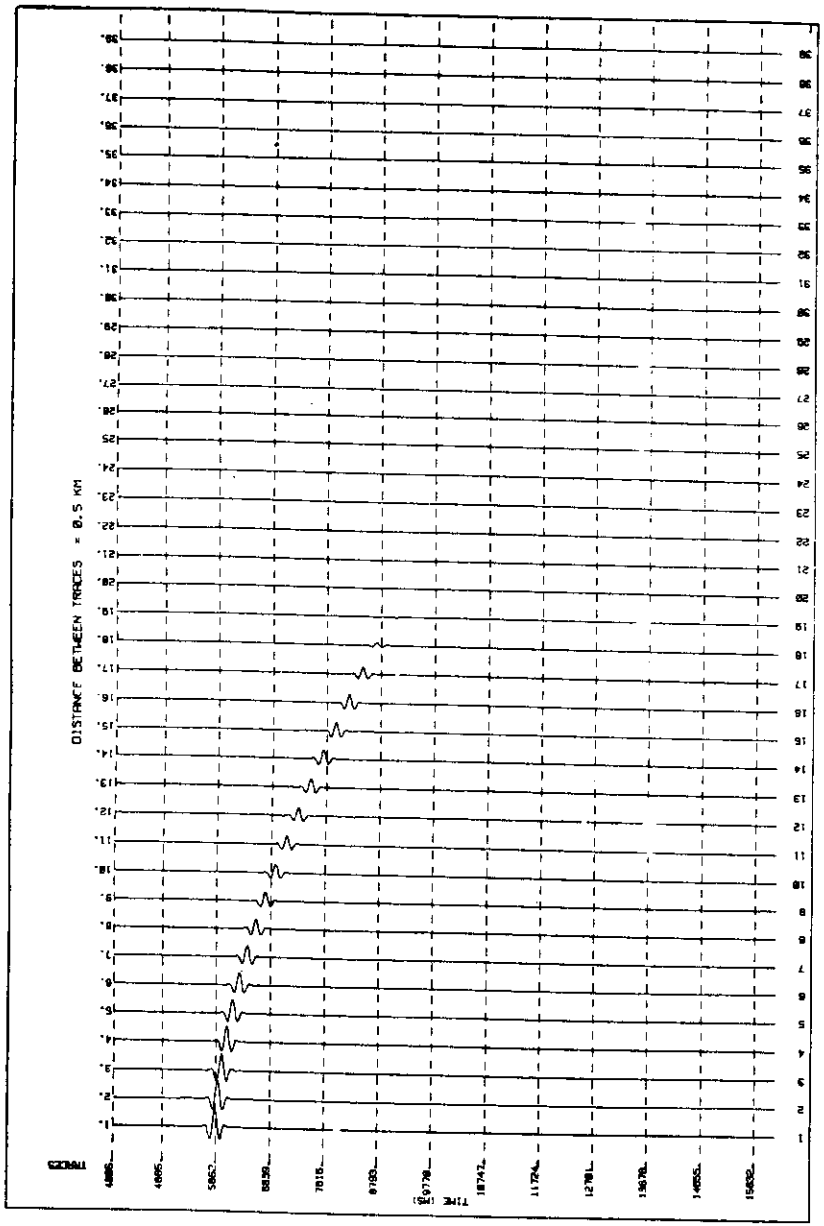

Fig. 5a

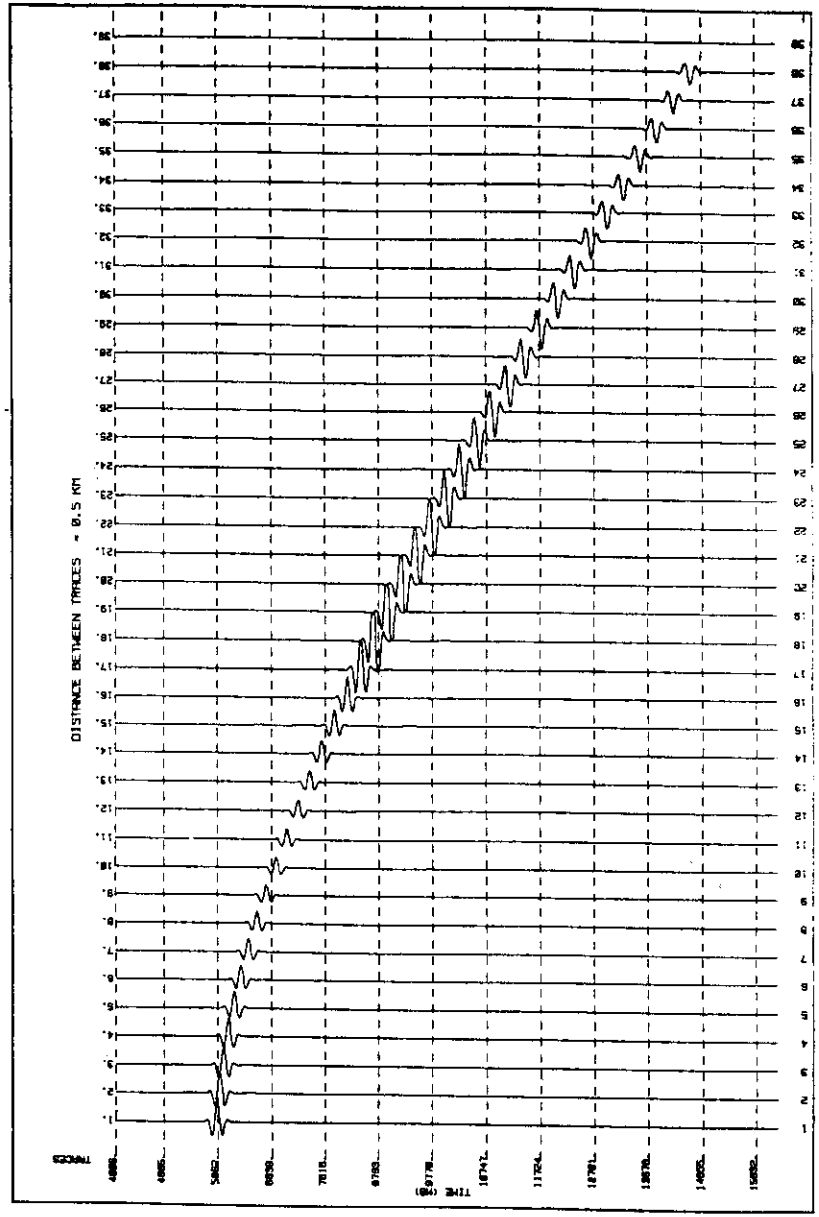

Fig. 5b

Fig. 5. Synthetic seismograms of the *P* waves reflected from the bottom reflector for the models shown in Fig. 3, out with a different inner strucure inside the thin high-velocity layer. The thin high-velocity layer consists of three laminas with alternating velocities. (a) Ray synthetic seismograms. (b) Hybrid ray-reflectivity seismograms. The reflections from the thin high-velocity layer are not considered.

velocity layer of larger thickness and with a broad-band seismic signal (not presented here).

Both the ray method and the hybrid ray-reflectivity method are only approximate. To appreciate the accuracy of synthetic seismograms shown in Figs. 4b and 4c, the full reflectivity synthetic seismograms shown in Fig. 4d can be used. Two distinct waves can be observed in the reflectivity seismograms: the first corresponds to the P waves reflected from the thin high-velocity layer, and is of no interest to us here. The second distinct wave corresponds to the wave reflected from the bottom interface, discussed in this paper. The two weak waves arriving later correspond to converted waves and are of no interest to us.

The comparison of Figs. 4b, c, and d shows that the standard ray synthetic seismograms of P waves reflected from the bottom interface completely fail in the whole overcritical region (traces 17 – 38).This has been, of course, expected as the standard ray method does not consider inhomogeneous waves. On the other hand, the hybrid ray-reflectivity seismograms show surprisingly accurate results, even at large epicentral distances (see traces 30 – 38). There are, of course, several expected differences between the full reflectivity and hybrid ray-reflectivity seismograms. At small epicentral distances, the reflectivity method yields smaller amplitudes than the hybrid ray-reflectivity method. This difference is caused by the well-known effects of the apparent velocity filtering in the reflectivity code. In the critical region (traces 18 – 25), we can observe the shift of the maxima of amplitudes of reflected waves in the full reflectivity computations from trace 18 to trace 23. This shift, which is frequency-dependent, is also well-known and has been described in detail in the seismological literature. It has nothing to do with the thin high-velocity layer in the overburden and exists even if the thin high-velocity layer is removed. For more details refer to in [9, 10].

In the conclusion of this section we can say that the standard ray method fully fails in the computation of overcritically reflected waves if a thin high-velocity layer is situated in the overburden. In this case, however, the hybrid ray-reflectivity method yields synthetic seismograms of good accuracy.

Thin laminated high-velocity layer

We keep all the conditions of computations the same as in the previous section, with one exception; we change the inner structure of the thin high-velocity layer. The thickness of the thin layer also remains the same, i.e. 0·05 km, but the thin layer is divided into three laminas with the same thickness of 0·0167 km. The medium parameters in the first and the third lamina are the same as they were before in the whole thin layer, but the medium parameters in the middle lamina correspond to the parameters in the overburden.

Figures 5a and 5b shown the synthetic seismograms of the P wave reflected from the bottom halfspace. Fig. 5a shows ray synthetic seismograms, and Fig. 5b the hybrid ray-reflectivity seismograms.

The results are very similar to those demonstrated in Figs. 4b and 4c. At small epicentral distances (traces 1 – 14), the synthetic seismograms again practically coincide with those presented in Figs. 4a, b, c. Thus, the inner structure of the thin high-velocity layer does not influence considerably the synthetic seismograms at small epicentral distances. In ray synthetic seismograms (Fig. 5a), the decay of amplitudes at greater epicentral distances is even faster than in Fig. 4b. The reflected

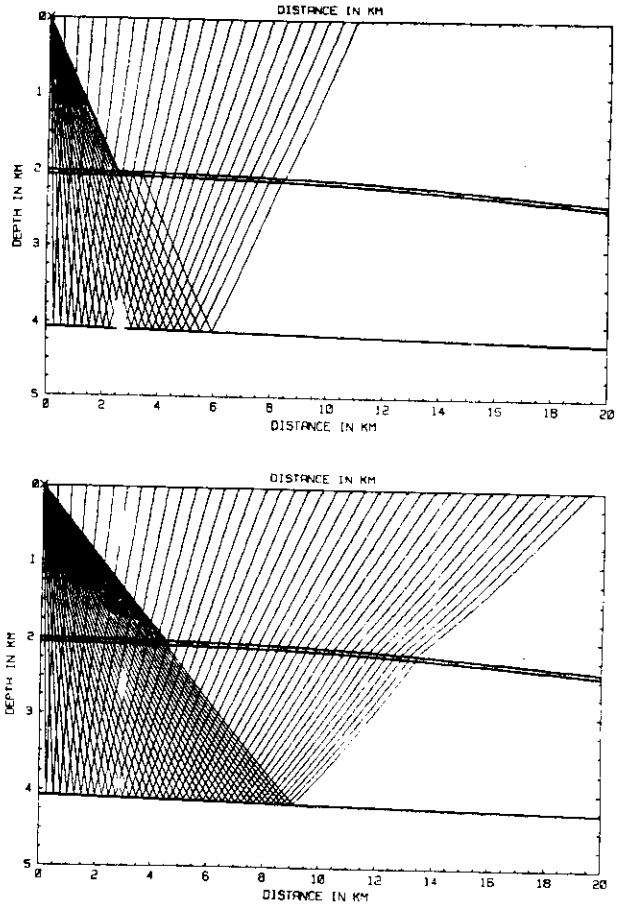

Fig. 6. Ray diagrams of a P wave reflected from the bottom reflector in a laterally varying 2-D structure. The thin high-velocity layer situated in the overburden is curved, the bottom reflector is dipping. The velocities inside the individual layers vary both laterally and vertically. (a) Standard ray computations. A shadow zone is formed beyond the epicentral distance of 11 km. (b) Hybrid ray-reflectivity computations. No shadow zone is formed. Note that the rays at larger epicentral distance are curved due to lateral variations of velocity.

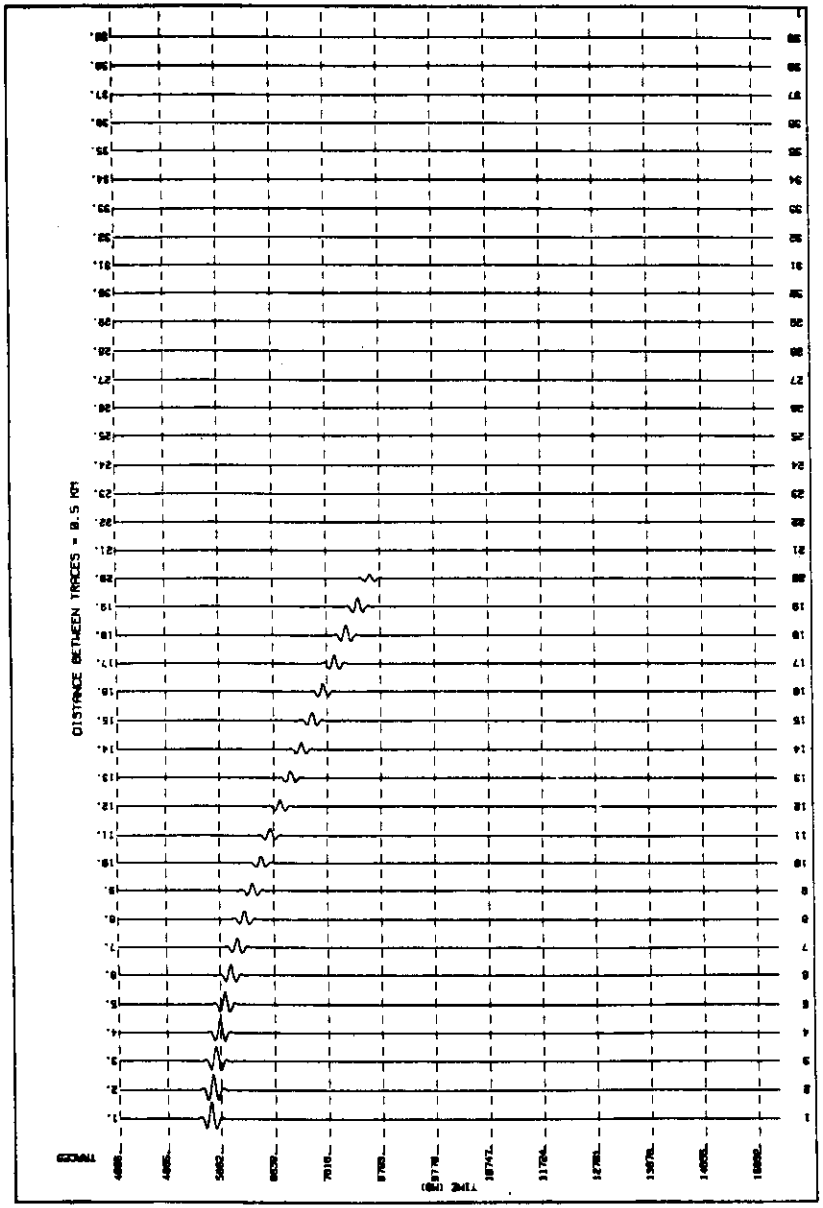

Fig. 7a

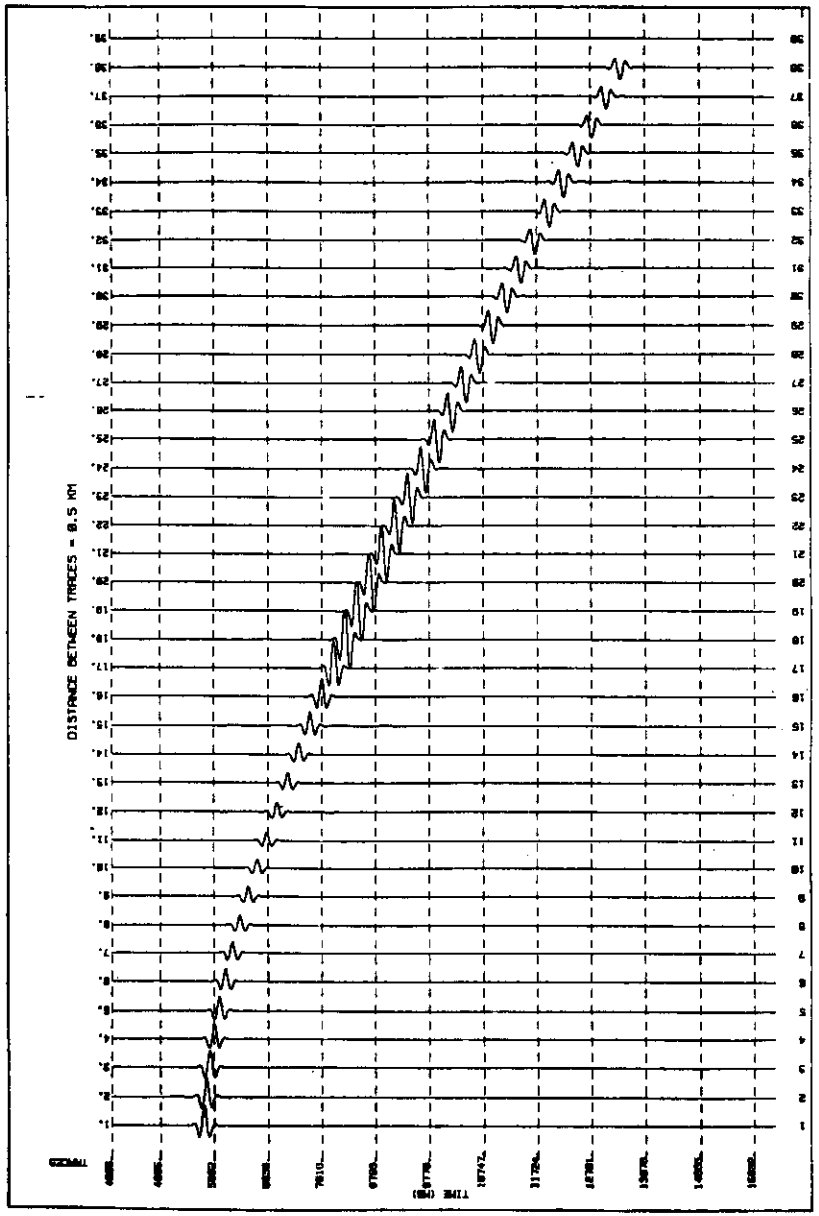

Fig. 7b

Fig. 7. Synthetic seismograms of P waves reflected from the bottom reflector, passing through the thin high-velocity layer, see models in Fig. 6. The reflections from the thin high-velocity layer are not considered. (a) Ray synthetic seismograms. (b) Hybrid ray-reflectivity synthetic seismograms.

waves practically vanish at traces 18 – 19. On the other hand, the hybrid ray-reflectivity synthetic seismograms for the high-velocity laminated layer display larger amplitudes at larger epicentral distances than the hybrid ray-reflectivity seismograms for the high-velocity homogeneous layer. Similarly as in Fig. 4c, the signals at larger epicentral distances have a more low-frequency character.

Curved thin high-velocity layer in a laterally varying structure

The model is again similar to the one above. The thin layer, however, is slightly curved and the reflector is slightly dipping. Moreover, the velocities in the overburden vary both laterally and vertically. Even the velocity inside the thin layer is not constant laterally, but varies from 2·0 km/s on the left-hand side to 2·1 km/s on the right-hand side of the model. We wish to demonstrate that the hybrid ray-reflectivity method can be applied without problems even to laterally varying structures. We, however, do not wish to change the previous model completely, so that only slight variations have been introduced.

Figures 6a and 6b show the ray diagrams for the model described above, corresponding to standard ray computations (6a) and to hybrid ray-reflectivity computation (6b). As we can see in Fig. 6a, the thin high-velocity layer again influences the ray diagram considerably. The rays do not even penetrate beyond trace number 21 (epicentral distance 11·0 km), where a shadow zone is formed. This effect is mainly due to the curvature of the thin layer. The ray diagram in Fig. 6b, corresponding to the hybrid ray-reflectivity method does not, of course, display any shadow zone. We thus expect the differences between the ray synthetic and hybrid ray-reflectivity seismograms to be even more pronounced than in Fig. 5.

The synthetic seismograms calculated by the two methods are shown in Figs. 7a and 7b. The ray seismograms behave similarly as the ray seismograms for the two previous models with a thin layer shown in Figs. 4b and 5a. Even though a ray theory shadow zone is formed in the model under consideration and no shadow zone was formed in previous cases, the actual behaviour of the ray synthetic seismogram is very similar. The behaviour of the synthetic seismograms computed by the hybrid ray-reflectivity method (Fig. 7b) is again drastically different from the ray synthetic seismograms.

4. CONCLUDING REMARKS AND DISCUSSION

The hybrid ray-reflectivity method extends the possibilities of the standard ray method considerably. It can be applied to 2-D and 3-D laterally varying layered structures which contain thin transition layers. The inner structure and physical properties within the thin transition layer may vary arbitrarily in the vertical direction. The method was used in [10] to study the properties of waves reflected from such

thin transition layers. The internal structure in the thin transition layer influences the amplitudes and frequency responses of reflected waves considerably. In this paper, the hybrid method is applied to the transmission of reflected waves through a thin high-velocity layer situated in the overburden of the reflector. It is shown that the method removes the difficulties of the standard ray method which is not able to describe properly the tunneling of seismic waves through the thin high-velocity layer along complex ray-paths at overcritical distances.

The accuracy of the hybrid ray-reflectivity computations related to thin high-velocity layer was tested by comparison with the reflectivity computations. It has been found that, in general, the hybrid ray-reflectivity method describes well the tunneling of seismic energy through a thin high-velocity layer. Differences were, of course, observed in the critical region, as the standard ray method was used in the hybrid ray-reflectivity computations presented in this paper. The hybrid Gaussian beam-reflectivity algorithm, which can be optionally used in BEAM87, would remove these differences.

The hybrid ray-reflectivity method can be used in many other applications important in seismology and in seismic prospecting. One such application is now under investigation and has yielded promising preliminary results. The thin layer in this application is situated directly at the top of the model. Another application is related to inhomogeneous waves. We feel it would be possible to incorporate even waves as pseudospherical, *P*, *S*, etc., into the routine ray computations in 2-D and 3-D laterally varying layered structures using the hybrid ray-reflectivity code.

Acknowledgements: This work was carried out during the sojourn of the firstnamed author at the Federal University of Bahia, Salvador. We wish to thank Drs. Peter Hubral and Ivan Pšenčík for valuable comments and discussions. We also thank Mr. Fernando C. M. de Andrade for his help with numerical computations using the full reflectivity method. The research was partly supported by the CNPq, FINEP, PETROBRÁS, and by the IBM Academic Initiative in Czechoslovakia.

Received 10. 10. 1991

References:

[1] C. Baag, C. A. Langston: A WKBJ spectral method for computation of *SV* synthetic seismograms in a cylindrically symmetric medium. Geophys. J. R. astr. Soc., 80 (1985), 387.
[2] V. M. Babich: Analytic continuation of the solutions of the wave equation into the complex region and caustics. In: Problems of the Dynamic Theory of Propagation of Seismic Waves 5, ed. Petrashen, G. I. Nauka, Leningrad Division, Leningrad 1961, 145 (in Russian).
[3] V. M. Babich: On transmission of a wave through a thin layer. Zapiski Nauchnych Seminarov LOMI, 173 (1988), 20 (in Russian).
[4] V. M. Babich, A. P. Kiselev: Ray description of the "nongeometrical" *S* wave. Izv. AN USSR, Fizika Zemli, No. 10, 1988, 67 (in Russian).
[5] V. M. Babich, A. P. Kiselev: Non-geometrical waves — are there any? An asymptotic description of some "non-geometrical" phenomena in seismic wave propagation. Geophys. J. Int., 99 (1989), 415.
[6] G. Bernasconi, G. Drufuca: Rays and reflectivity: An intermediate approach. 60th Annual SEG Meeting Extended Abstracts. San Francisco 1990, 1012.

[7] L. M. Brekhovskikh: Waves in Layered Media. Academic Press, New York, 1960.
[8] V. Červený: The reflection of spherical waves at a plane boundary. Geofys. sb., 4 (1957), 343.
[9] V. Červený: Accuracy of ray theoretical seismograms. J. Geophys., 46 (1979), 135.
[10] V. Červený: Synthetic body wave seismograms for laterally varying media containing thin transition layers. Geophys. J. Int., 99 (1989), 331.
[11] V. Červený, J. Kozák, I. Pšenčík: Refraction of elastic waves into a medium of lower velocity — Pseudospherical waves. Pure and Appl. Geophys., 92 (1971), 115.
[12] V. Červený, I. A. Molotkov, I. Pšenčík: Ray Method in Seismology. Universita Karlova, Praha, 1977.
[13] I. D. Cvankin, A. V. Kalinin: Non-ray effects in the generation of converted seismic waves. Fizika Zemli, No. 2, 1984, 34 (in Russian).
[14] I. D. Cvankin, A. V. Kalinin, M. A. Kalita: Mathematical modelling of the wave field in the cross-borehole shooting with the consideration of non-ray effects. Vestnik Mosk. Univ., Ser. 4, No. 5, 1985, 85 (in Russian).
[15] P. Cummins, L. Johnson: Synthetic seismograms for an inner core transition of finite thickness. Geophys. J., 94 (1988), 21.
[16] P. F. Daley, F. Hron: Ray-reflectivity method for *SH* waves in stacks of thick and thin layers. Geophys. J. R. astr. Soc., 69 (1982), 527.
[17] P. F. Daley, F. Hron: Nongeometrical arrivals due to highly concentrated sources adjacent to plane interfaces. Bull. Seismol. Soc. Amer., 73 (1983), 1655.
[18] P. D. Einziger, L. B. Felsen: Evanescent waves and complex rays. IEEE-TAP, AP-30 (4), (1982), 594.
[19] H. Emmerich: 2-D wave propagation by a hybrid method. Geophys. J., 99 (1989), 307.
[20] L. B. Felsen, N. Markuwitz: Radiation and Scattering of Waves. Prentice Hall, Englewood Cliffs, 1973.
[21] J. Fertig: Shear waves by an explosive point source: the Earth's surface as a generater of converted $P-S$ waves. Geophys. Prosp., 32 (1984), 1.
[22] K. Fuchs, G. Müller: Computation of synthetic seismograms with the reflectivity method and comparison with observations. Geophys. J. R. astr. Soc., 23 (1971), 417.
[23] K. Fuchs, K. Schulz: Tunneling of low-frequency waves through the subcrustal lithosphere. J. Geophys., 42 (1976), 175.
[24] F. Hron, B. B. Mikhailenko: Numerical modelling of nongeometrical effects by the Alekseyev-Mikhailenko method. Bull. Seismol. Soc. Amer., 71 (1981), 1011.
[25] H. Ikuno, L. B. Felsen: Complex ray interpretation of reflection from concave-convex surfaces. IEEE-TAP, AP-27 (2), (1988), 199.
[26] J. B. Keller: A geometrical theory of diffractions. In: Calculus of Variations and Its Application, ed. Graves, L. M. McGraw-Hill, New York, 1958, 27.
[27] Yu. A. Kravtsov: Complex rays and complex caustics. Radiofizika, 10 (1967), 1284.
[28] A. L. Litvin, I. D. Cvankin: Investigation of certain types of inhomogeneous seismic waves. Fizika Zemli, No. 4, 1981, 72 (in Russian).
[29] G. R. Mellman, D. V. Helmberger: High-frequency attenuation by a thin high-velocity layer. Bull. Seismol. Soc. Amer., 64 (1974), 1383.
[30] G. Müller: The reflectivity method: A tutorial. J. Geophys., 58 (1985), 153.
[31] H. Ott: Reflexion and Brechung von Kugelwelle. Effecte 2. Ordnung. Ann. d. Phys., 41 (1942), 443.
[32] L. I. Ratnikova: The Method of Seismic Wave Computation in Thinly Layered Media. Nauka, Moscow, 1973 (in Russian).
[33] J. Schleicher, P. Hubral, M. Tygel: Nonspecular reflection from a curved interface. Geophysics, 56 (1991), 1203.
[34] M. Tygel, P. Hubral: Transient Waves in Layered Media. Elsevier, Amsterdam, 1987.